

Notes for Ultracold Quantum Gases

(LMU, WS 2020/21)

Lecturer: Simon Fölling
Typing: Yilun Yang

Contents

1	Introduction	1
1.1	A brief history of cold	1
1.2	Quick review of atomic physics	2
1.3	Atoms in external fields	3
1.3.1	Light-atom interaction	5
2	Laser Cooling	8
2.1	Light forces	8
2.2	Doppler and sub-Doppler cooling	9
2.2.1	Doppler cooling	9
2.2.2	Sub-Doppler cooling: polarization gradient cooling	11
2.3	Conservative Trapping Potentials	13
2.3.1	Light trapping	13
2.3.2	Magneto-optical trapping (MOT)	14
2.4	Evaporative cooling	16
2.5	Absorption imaging	18
2.6	Journal Club 1: Molasses cooling (Chu et al., 1985)	20
2.7	Journal Club 2: Evaporative cooling (Davis et al., 1995b)	25
3	Ideal Bose Gas and Bose-Einstein Condensation	30
3.1	Ideal gas in phase space	30
3.2	Bose-Einstein condensation	32
3.2.1	Density distribution of cold bosons	33
3.2.2	Interference of two bose-einstein condensates	34
3.3	Journal Club 3: BEC in sodium gas (Davis et al., 1995a)	37
3.4	Journal Club 4: <i>s</i> and <i>d</i> wave scattering interference (Thomas et al., 2004)	44
4	BEC with interactions	49
4.1	Scatterings	49
4.1.1	Elastic scattering	49

CONTENTS

4.1.2	Pseudo potential	52
4.2	BEC with weak interaction	53
4.2.1	Second quantization formalism for BEC	53
4.2.2	Gross-Pitaevskii equation	54
4.2.3	Thomas-Fermi regime	55
4.2.4	Attractive interactions	56
4.3	Excitation of (weakly interacting) BECs	58
4.3.1	solitons in 1D	58
4.3.2	Solitons in 2D	59
4.4	Journal Club 5: Solitons (Becker et al., 2008)	63
5	Ultracold atoms in periodic potentials	70
5.1	Bloch theorem	70
5.1.1	Solution for optical standing wave	72
5.1.2	Phase velocity, group velocity	73
5.2	Momentum space measurements on atoms in lattices	74
5.2.1	Wannier functions	74
5.2.2	Time of flight-imaging	75
5.2.3	Band mapping	77
5.3	Bose Hubbard model	78
5.3.1	Non-interacting case	78
5.3.2	Interaction dominated case	79
5.3.3	Phase transition in Bose-Hubbard model	80

CONTENTS

Chapter 1

Introduction

Literatures of the lecture:

- *Bose-Einstein Condensation in Dilute Gases*, (Pethick and Smith, 2008);
- *Theory of Bose-Einstein condensation in trapped gases*, (Giorgini et al., 2008);
- *Making, probing and understanding Bose-Einstein condensates*, (Ketterle et al., 1999);
- *Many-body physics with ultracold gases*, (Bloch et al., 2008).

1.1 A brief history of cold

- In 1904-1905, Heike Kamerlingh-Onnes starts the first really serious cold temperature lab to make liquid helium ($\sim 4\text{ K}$) and succeed in 1908.
- By 1910, the lowest temperature achieved is $\sim 1\text{ K}$ by depressurizing helium.
- In 1911, superconductivity is discovered in cold mercury metal.
- In 1937, superfluidity is discovered in liquid ^4He and ^3He .
- In 1965, dilution refrigerator reaches $\sim 0.1\text{ K}$. (With this "refrigerator approach" today one can reach typically $\sim 0.01\text{--}0.01\text{ K}$, but down to 2 mK .)

- In 1975, T. Hänsch and A. Schawlow, as well as D. Wineland and H. Dehmelt propose laser cooling. The motivation is that slow atoms allow higher resolution when doing spectroscopic atomic physics experiments.
- In early 1980s, laser slowing and cooling of atoms can reach $\sim \text{mK}$.
- In 1985-1987, with magneto-optical trap (MOT) and optical molasses cooling, atoms were cooled down to $\sim 40 \mu\text{K}$.
- In 1995, Bose-Einstein condensate is achieved at 170 nK in a dilute gas of ^{87}Rb atoms by Eric Cornell and Carl Wieman (JILA) and a few months later with ^{23}Na by Wolfgang Ketterle (MIT).
- In 1999, Guinness book records 100 pK (Ketterle group).

Condensed matter	Cold atoms
$\sim 10^{23}$ electrons	$\sim 10^5$ atoms
charged particles: long-range Coulomb interaction, Lorentz force	neutral: contact interactions
homogeneous	inhomogeneous (trap)
density: 10^{23} cm^{-1}	density: 10^{14} cm^{-1}
$T_F = 10^3\text{-}10^5 \text{ K}$	$T_F = 10 \times 10^{-6} \text{ K}$
very fast dynamics: dynamics not easily observable fast thermalisation	much slower dynamics (ms-s) observable dynamics bottleneck in preparation
well-controlled temperature and chemical potential	isolated system with fixed entropy and atom number; limited temperature range

Table 1.1: Comparison of cold atoms and condensed matter physics

1.2 Quick review of atomic physics

Our goal is to create an ultracold quantum gas of atoms with $\lambda \gtrsim d$, where d is the interaction distance between atoms and λ is the De Broglie wave length

$$\lambda = \frac{h}{\sqrt{2\pi m k_B T}}. \quad (1.1)$$

From the formula single, light atoms should be considered. For Hydrogen, when $n = 1.8 \times 10^{14} \text{ cm}^{-3}$, the critical temperature would be $T_c = 50 \mu\text{K}$. It is however not a good choice as we will see later, but Hydrogen-like structure is good, as it has well defined "closed" transitions and the ground state transitions has good wavelengths and line widths. Later we will always use Alkali atoms. Their atomic states can be described by:

- n : principle quantum number;
- L : orbital angular momentum;
- S : electron spin;
- J : $L-S$ coupling;
- I : nucleus spin (hyperfine structure);
- F : $J-I$ coupling;
- m, m_j, m_F : angular momentum orientations.

We use the ^{87}Rb levels as an example, see Fig. 1.1. For the ground state ($l = 0$) and first excited states ($l = 1$), the quantum numbers $n = 5, s = 1/2, I = 3/2$. The transitions between 5S and 5P states are "optical"; between $5^2\text{S}_{\frac{1}{2}}$ states with different F is "microwave"; and between $5^2\text{P}_{\frac{3}{2}}$ are "radio wave".

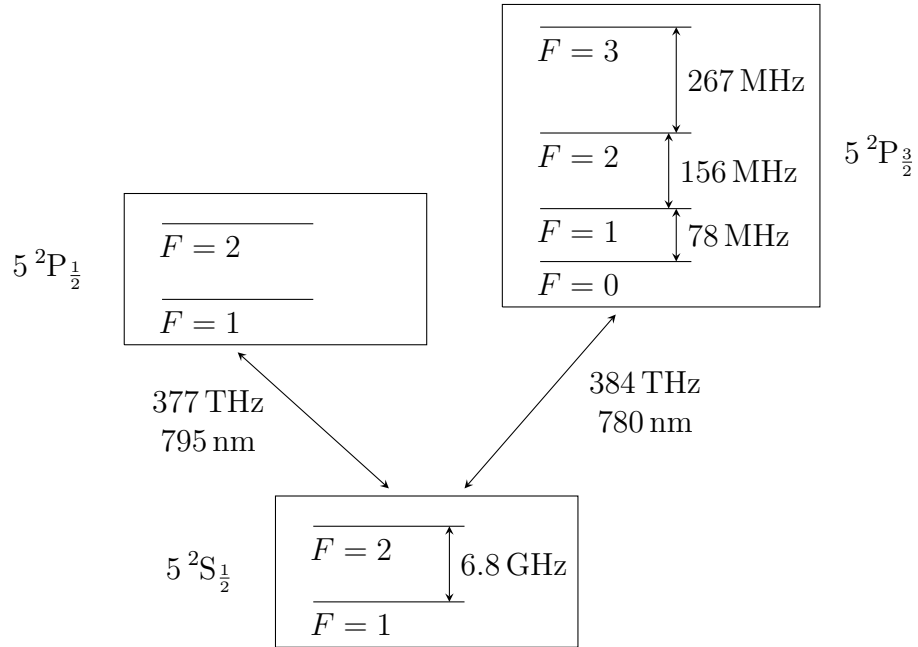
Selection rules

- $|\Delta L| = 1, |\Delta S| = 0$;
- $|\Delta J| \leq 1$, but $J = 0 \rightarrow J = 0$ is forbidden;
- $|\Delta F| \leq 1$, but $F = 0 \rightarrow F = 0$ is forbidden;
- $|\Delta m| \leq 1$.

By controlling the direction of the light, the change of m can be determined by absorbing a photon.

1.3 Atoms in external fields

When talking about atoms in external fields, we usually need to consider electrostatic fields, magnetic fields, of course electromagnetic fields and sometimes also gravity.


 Figure 1.1: Some lowest levels of ^{87}Rb

Electrostatic field As atoms are neutral particles, the influence by electrostatic fields is usually small. It is interesting only in special cases, like for ions, highly excited atoms (Rydberg atoms) and molecules, where the dipole moments are large.

Magnetic field In magnetic field, we need to consider the Zeeman effects, usually the weak field situation of interest. The magnetic field functions as a (weak) hyperfine coupling to Hamiltonian:

$$\Delta E = g_F m_F \mu_B B, \quad (1.2)$$

where g_F is the Landau factor and $\mu_B = e\hbar/2m_e$ is the Bohr magnet.

Reduced mass correction The nucleus mass is large, but not infinite to reduce the mass changes

$$\mu \sim \frac{m_e m_n}{m_e + m_n}, \quad (1.3)$$

so $\mu - m_e \sim m_e/1000$. All energies are shifted by this factor.

1.3.1 Light-atom interaction

The most interesting part is the light-atom interaction, which is really used broadly to control the atoms.

Rabi model The basic Hamiltonian is a two level system plus interaction with electric field through a dipole:

$$H = H_0 + V = H_0 - \mathbf{d}(t) \cdot \mathbf{E}(t). \quad (1.4)$$

We make several assumptions:

1. The light field is monochromatic and classical: $\mathbf{E}(t) = \mathbf{E}_0 \cos(\omega_L t)$.
2. The spatial structure of dipole is much smaller than λ_{light} , which can be ignored.
3. (*Rotating wave approximation*) $\omega_{12} = (E_1 - E_2)/\hbar \approx \omega_L$, where E_1 and E_2 are the two levels of atom.

In matrix form,

$$H = \begin{pmatrix} E_1 & -\Omega_0 \cos(\omega_L t) \\ -\Omega_0 \cos(\omega_L t) & E_2 \end{pmatrix}, \quad (1.5)$$

where

$$\Omega_0 := \frac{\langle 2 | \mathbf{d} \cdot \mathbf{E}_0 | 1 \rangle}{\hbar} \quad (1.6)$$

is the *Rabi frequency*. Further define the *detuning*

$$\delta := \omega_L - \omega_{12}. \quad (1.7)$$

In the interacting picture, define the rotating frame:

$$\begin{aligned} |\tilde{1}\rangle &= e^{i\delta t/2} |1\rangle, \\ |\tilde{2}\rangle &= e^{-i\delta t/2} |2\rangle. \end{aligned} \quad (1.8)$$

Use rotating wave approximation to ignore the fast-oscillating terms, and the effective interaction will be

$$\tilde{V} = \frac{\hbar}{2} \begin{pmatrix} -\delta & -\Omega_0 \\ -\Omega_0 & \delta \end{pmatrix}. \quad (1.9)$$

It's solution are the *dresses states*

$$|\pm\rangle = \frac{1}{\sqrt{2\Omega(\Omega \pm \delta)}} \begin{pmatrix} -\Omega_0 \\ \delta \pm \Omega \end{pmatrix} \quad (1.10)$$

with eigenvalues $E_{\pm} = \pm \hbar\Omega/2$, where

$$\Omega := \sqrt{\Omega_0^2 + \delta^2} \quad (1.11)$$

is the *effective Rabi frequency*.

The excited state ($|e\rangle$) population can also be calculated:

$$P_e(t) = \frac{\Omega_0^2}{\Omega^2} \sin^2\left(\frac{\Omega t}{2}\right) \quad (1.12)$$

given that the initial state is the ground state.

Optical Bloch equations and light scattering rate Write the Rabi problem in terms of density matrices, and moreover introduce spontaneous decay from excited state to ground state at rate γ :

$$\begin{aligned} \dot{\rho}_{11} &= \frac{i}{2}\Omega_0(\tilde{\rho}_{21} - \tilde{\rho}_{12}) - \gamma(\rho_{11}) \\ \dot{\rho}_{22} &= \frac{i}{2}\Omega_0(\tilde{\rho}_{12} - \tilde{\rho}_{21}) + \gamma(\rho_{11}) = -\dot{\rho}_{11} \\ \dot{\tilde{\rho}}_{12} &= \frac{i}{2}\Omega_0(\rho_{22} - \rho_{11}) - (\gamma/2 - i\delta)\tilde{\rho}_{12} \\ \dot{\tilde{\rho}}_{21} &= \frac{i}{2}\Omega_0(\rho_{11} - \rho_{22}) - (\gamma/2 + i\delta)\tilde{\rho}_{21} = \dot{\tilde{\rho}}_{eg}^*. \end{aligned} \quad (1.13)$$

These equations are called *Optical Bloch equations*. The decay rate can actually be related to the dipole moment:

$$\gamma = \frac{d^2\omega_{21}^3}{3\pi\epsilon_0\hbar c^3}. \quad (1.14)$$

The steady state solution gives

$$\rho_{ee}^{\infty} = \frac{s_0/2}{1 + s_0 + (2\delta/\gamma)^2} \quad (1.15)$$

with the *saturation parameter* $s_0 = 2\Omega_0^2/\gamma^2$. The name of the parameter comes from the fact that $s_0 = I/I_{\text{sat}}$ is the ratio of driving field intensity to the saturation intensity $I_{\text{sat}} = \frac{\pi hc}{3\lambda^3}\gamma$. Now the scattering rate is

$$\Gamma_{\text{sc}} = \gamma\rho_{ee} = \frac{\gamma}{2} \frac{s_0}{1 + s_0} \cdot \frac{1}{1 + 4\delta^2/(\gamma')^2}. \quad (1.16)$$

It is a Lorentzian with *saturation broadened line width* $\gamma' = \gamma\sqrt{1+s_0}$.

Remarks

- The decay rate γ of the excited state usually corresponds to life time of order $\tau \approx 20 \text{ nm}$ for optical transitions, but for microwave or lower transitions, it is much larger than the length of experiment (e.g., $\sim \text{years}$).
- Optical fields are almost always in the *far field*, which means there are many wavelengths of distance in propagation from the source to the atom. The wavelengths of radio and microwaves are however much larger than the size of the experiment, and are called *near field* of the emitter.

Chapter 2

Laser Cooling

2.1 Light forces

The light force comes from the momentum transfer of photons:

$$\mathbf{F} = \pm \Gamma_{\text{sc}} \mathbf{p}_{\text{ph}} = \pm \Gamma_{\text{sc}} \hbar \mathbf{k}, \quad (2.1)$$

where the plus and minus sign represent absorbing and emitting photons respectively. Note that the emission is undirected while absorption is directed, and hence we take the positive sign. Using the scattering rate derived in 1.3.1, this yields a force of

$$\mathbf{F} = \frac{\hbar \mathbf{k} \gamma}{2} \frac{s_0}{1 + s_0 + 4\delta^2/\gamma^2}. \quad (2.2)$$

The typical values of corresponding acceleration in the strong interaction limit ($s_0 \rightarrow \infty$) are:

- ^{87}Rb : $m = 87 \text{ u}$, $\gamma = 2\pi \times 6.8 \text{ MHz}$, $a \approx 110\,000 \text{ m s}^{-2}$.
- ^{88}Sr : $m = 88 \text{ u}$, $\gamma = 2\pi \times 35 \text{ MHz}$, $a \approx 990\,000 \text{ m s}^{-2}$.

This is however for atoms at rest. In the moving frame, we need to take into account the Doppler effect. For atoms moving facing the light with velocity \mathbf{v} , in the rest frame of atoms the frequency of light changes by $\mathbf{k} \cdot \mathbf{v}$:

$$\omega'_L = \omega_L - \mathbf{k} \cdot \mathbf{v}. \quad (2.3)$$

Thus the light force becomes velocity dependent:

$$\mathbf{F}(\mathbf{v}) = \frac{\hbar \mathbf{k} \gamma}{2} \frac{s_0}{1 + s_0 + 4(\delta - \mathbf{k} \cdot \mathbf{v})^2/\gamma^2}. \quad (2.4)$$

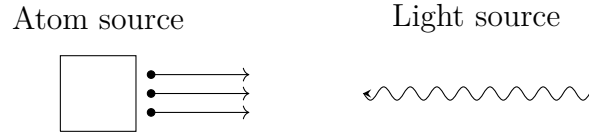


Figure 2.1: Typical setup of laser cooling

The typical setting for decelerating atoms is shown in Fig. 2.9. It works only for a small range of velocity; the change in velocity will lead to change in effective detuning. There are different ideas to cool down the atoms in the full velocity distribution:

- (*Chirp cooling*) Change the frequency from right to left.
- (*White light slowing*) use all frequencies simultaneously.
- (*Zeeman cooling*) Use Zeeman shift to compensate the Doppler effect.

2.2 Doppler and sub-Doppler cooling

2.2.1 Doppler cooling

The goal of Doppler cooling is to reduce the width of any velocity even without an overall direction (see left side of Fig. 2.2; $P(v_x)$ is the distribution of x -direction velocities of atoms).

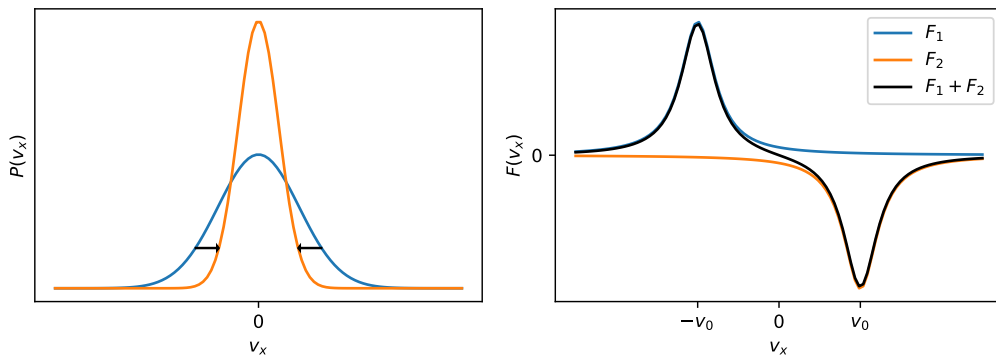


Figure 2.2: Doppler cooling

The idea is to use counter-propagating light beams. A positive acceleration force is need for negative velocities (F_1 in right side of Fig. 2.2) and vice versa

(F_2) . Therefore the detuning has to be *negative* to meet the requirements and $v_0 = -\delta/k$. In the center, the negative slope means a damping force

$$F(v) \approx -\beta v, \quad \beta = -8\hbar k^2 \frac{\delta s_0}{\gamma(1 + s_0 + 4\delta^2/\gamma^2)^2} \quad (2.5)$$

and the cooling rate (loss rate of kinetic energy) is $-\beta v^2$.

Doppler limit. What is the lowest temperature which can be achieved? We have considered absorption; now let's take emission also into account. The momentum transferred per absorption-emission process is $\sqrt{2}\hbar k$ with completely random direction. After N emissions, the probability distribution of the norm of momentum transferred will be Gaussian due to the central limit theorem, with width $\sqrt{2N}\hbar k$. This indicates the heating by per scattering is of order recoil energy

$$E_{\text{rec}} = \frac{(\sqrt{2}\hbar k)^2}{2m} \quad (2.6)$$

and the heating rate is $6\Gamma_{\text{sc}}E_{\text{rec}}$ (for 6 laser beams in total). To achieve equilibrium, we have

$$6\Gamma_{\text{sc}}E_{\text{rec}} - \beta\bar{v}^2 = 0, \quad (2.7)$$

which gives the equilibrium temperature

$$\frac{3}{2}k_B T = \frac{1}{2}m\bar{v}^2 = -\frac{3\hbar}{16} \left[(1 + s_0) \frac{\gamma^2}{\delta} + 4\delta \right]. \quad (2.8)$$

The minimum is reached when $\delta = -\gamma'/2$, which gives

$$k_B T = \frac{\hbar\gamma'}{2k_B}. \quad (2.9)$$

Finally, we are working in the low saturation limit $s_0 \rightarrow 0$, which defines the *Doppler temperature*:

$$T_D = \frac{\hbar\gamma}{2k_B}. \quad (2.10)$$

For instance, T_D is 240 μK for Na, 4.4 μK for Yb and 150 μK for Rb. It corresponds to a Doppler velocity of $v_D \sim 15 \text{ cm s}^{-1}$.

Using 3 pairs of laser beams in 3D is called *molasses* cooling, performed by (Chu et al., 1985) and (PHILLIPS et al., 1988). It however turns out that the temperature measured are much lower than the Doppler temperature: for Na, they got only 50 μK . There must be still sub-Doppler cooling effects.

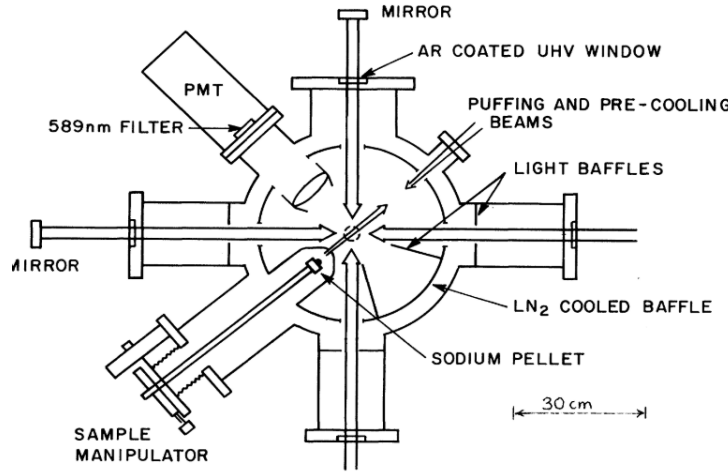


Figure 2.3: Molasses cooling scheme from (Chu et al., 1985). The vertical confining beam is indicated by the dashed circle.

2.2.2 Sub-Doppler cooling: polarization gradient cooling

One new idea of further cooling is to use the fact that a real atom has more than one ground state and excited state, so that the kinetic energy can be removed when climbing up the potentials and the atom then jump to lower energy levels. This cycles are called *Sysiphus cooling*. Typically, hyperfine structure has two ground states, which can be changed by optical excitation and subsequent decay.

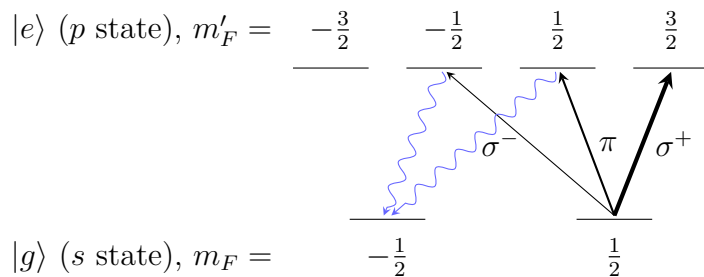


Figure 2.4: Typical hyperfine structure of atom

The strengths of dipole transitions are different. The Clebsch-Gordon coef-

ficients ${}_{m'_F} \langle e|d|g \rangle_{n_F}$ are

$$\begin{aligned} {}_{\frac{3}{2}} \langle e|d|g \rangle_{\frac{1}{2}} &= {}_{-\frac{3}{2}} \langle e|d|g \rangle_{-\frac{1}{2}} = 1 \\ {}_{\frac{1}{2}} \langle e|d|g \rangle_{\frac{1}{2}} &= {}_{-\frac{1}{2}} \langle e|d|g \rangle_{-\frac{1}{2}} = \sqrt{\frac{2}{3}} \\ {}_{-\frac{1}{2}} \langle e|d|g \rangle_{\frac{1}{2}} &= {}_{\frac{1}{2}} \langle e|d|g \rangle_{-\frac{1}{2}} = \sqrt{\frac{1}{3}}. \end{aligned} \quad (2.11)$$

In optical molasses, a pair of counterpropagating, linearly parallel polarized lasers will interfere to be standing waves:

$$E_{tot} = Ee^{-ikx} + Ee^{ikx} = 2E \cos(kx). \quad (2.12)$$

But if we choose orthogonal polarization, there will be a polarization pattern in the x -direction, and the light can be decomposed into σ^+ and σ^- components; each corresponds to an attractive potential if we choose red detuning ($\delta < 0$). Due to the Clebsch-Gordon coefficients, the atoms "see" different potentials.

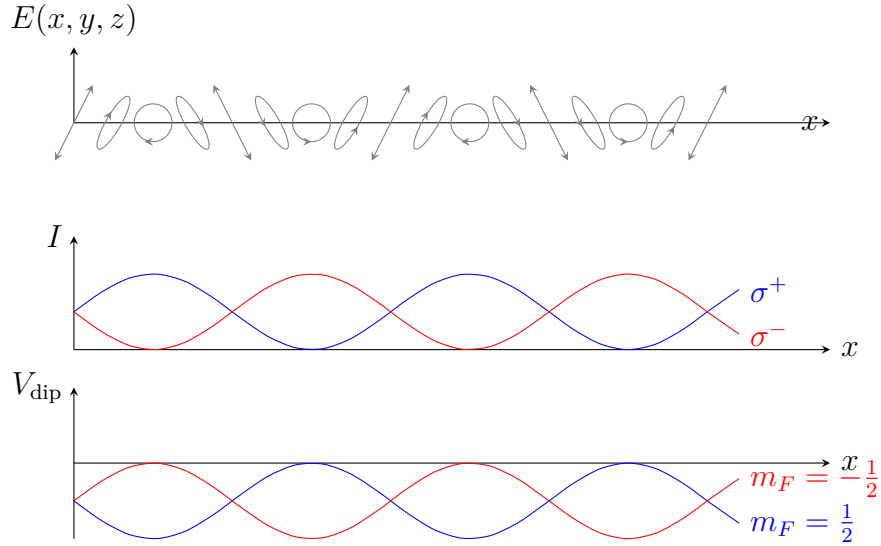


Figure 2.5: Counterpropagating lights with orthogonal polarization.

When σ^+ dominates, $m_F = \frac{1}{2}$ state is stable, while $m_F = -\frac{1}{2}$ state will be firstly excited to $m'_F = \frac{1}{2}$ state and then decayed to $m_F = \frac{1}{2}$ state, since the π decay is stronger than the σ^- decay. Therefore the atoms at the state with higher potential will jump to the other and lose energy. Then how low can the temperature go?

In the x direction, the time needed for an atom to climb to the top of the potential is $\Delta t = \lambda/2v_x$, and the energy loss ΔE is the difference between the two potentials. The cooling rate is

$$\frac{\Delta E}{\Delta t} = \frac{2\Delta E}{\lambda} v_x, \quad (2.13)$$

which will dominate the Doppler cooling ($\propto v^2$) in low v limit. Under these conditions, there is no natural equilibrium point of heating and cooling. The next fundamental limit is however the recoil limit: the emission of the last scattered photon is uncontrolled (when we remove the laser), and its momentum will determine the minimum temperature:

$$T_{\text{rec}} = E_{\text{rec}}/k_B = \frac{\hbar^2 k^2}{2mk_B}. \quad (2.14)$$

For Rb, $T_{\text{rec}} \sim 350 \text{ nK}$ and for Na, $T_{\text{rec}} \sim 2.5 \mu\text{K}$. This is *not* yet the ultimate limit for optical cooling; there are even sub-recoil optical cooling methods, though rarely used.

2.3 Conservative Trapping Potentials

We have so far only discussed about slowing down the atoms, but not trapping them in configuration space. This can be done by introducing conservative trapping potentials $V(\mathbf{r})$ which satisfies

- $F(\mathbf{r}) = -\nabla V(\mathbf{r})$;
- there is ideally no photon scattering;
- there is ideally no heating;
- there is also no cooling, except for adiabatic case.

2.3.1 Light trapping

Recall the dressed states $|\pm\rangle$ with energies $E_{\pm} = \frac{\hbar}{2}\Omega$. There will now be avoided crossing at $\delta = 0$ with splitting Ω_0 for any finite Ω_0 , see Fig. 2.6. The shift in energy eigenstates due to the light-atom interaction is called *light shift*. For $E_1 = \hbar\sqrt{\Omega_0^2 + \delta^2}/2$, it is in the limit $|\delta| \gg |\Omega_0|$

$$\Delta E = \frac{\hbar}{2}\Omega - \frac{\hbar}{2}\delta \approx \frac{\hbar\Omega_0^2}{4\delta} = \frac{\hbar}{8} \cdot \frac{\gamma^2}{\delta} \cdot \frac{I}{I_{\text{sat}}}. \quad (2.15)$$

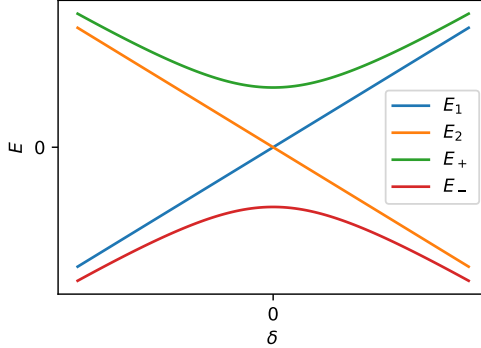


Figure 2.6: Avoided crossing

When the intensity is position dependent, the light field is equivalent to the *dipole potential*

$$V_{\text{dip}}(x) = \frac{\hbar\gamma^2}{8\delta I_{\text{sat}}} I(x). \quad (2.16)$$

It is a conservative potential, which can produce a force

$$F(x) = -\nabla V_{\text{dip}}(x) = -\frac{\hbar\gamma^2}{8\delta I_{\text{sat}}} \nabla I(x) \quad (2.17)$$

to *trap* the atom. In general we use with negative detuning a Gaussian laser beam:

$$I(x, y) = I_0 \exp\left(-2\frac{x^2}{w_x^2} - 2\frac{y^2}{w_y^2}\right). \quad (2.18)$$

It also provides a different view towards the relation between detuning and scattering rate. In the far-detuned limit, the scattering rate is

$$\Gamma_{\text{sc}} = \frac{\gamma/2}{1 + (2\delta/\gamma')^2} \cdot \frac{s_0}{1 + s_0} \approx \frac{\gamma^3 s_0}{8\delta^2} = \frac{1}{\hbar} V_{\text{dip}} \frac{\gamma}{\delta}. \quad (2.19)$$

Therefore when we choose large detuning δ , the scattering rate is proportional to $1/\delta$ so that $1/\Gamma_{\text{sc}}$ is longer than the measurement.

2.3.2 Magneto-optical trapping (MOT)

There can be further confinement and compression to the atoms done together. The idea is to add position-dependence to the scattering force so

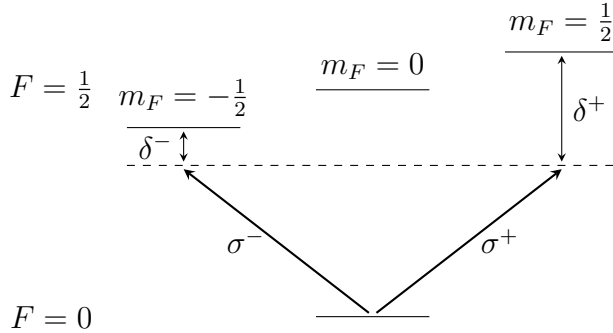


Figure 2.7: Levels under Zeeman effect

that the particles are pushed to the center. We use the Zeeman effect with magnetic field gradient ($B_x = b_x \cdot x$) to create the position dependence. The Zeeman potential is $V(x) = g_F m_F \mu_B B_x$. When $B_x > 0$ and the detuning is negative, $|\delta^-| < |\delta^+|$ so σ^- is more resonant.

Quadrupole field We use parallel coils whose currents go towards opposite directions. Close to the origin, the field components are linear in position:

$$B_i(x, y, z) = b_i \cdot i, \quad i = x, y, z. \quad (2.20)$$

Therefore the effective detuning would be $\delta^\pm = \delta \mp \mathbf{k} \cdot \mathbf{v} \pm \frac{1}{2} g_F \mu_B B / \hbar$, which lead to a new term in the scattering force of laser pair in Doppler cooling:

$$F(\mathbf{v}, \mathbf{r}) = -\beta \mathbf{v} - \kappa \mathbf{r}. \quad (2.21)$$

The minus sign in front of $\kappa \mathbf{r}$ is due to that \mathbf{k} has opposite sign to \mathbf{x} . This is a damped harmonic oscillator. The limitation of the damping comes from collisions between particles and radiation pressure from scattering.

A tricky point is that when B_x changes sign, the polarization of atom also changes sign and light switches to σ^+ . The non-adiabatic spin flips near the center of the trap will cause loss of atoms, namely majorana losses, constituting as a hole. This effect can be suppressed by adding a repulsive potential around the center to avoid the sign change (Davis et al., 1995a). The limitation of MOT to condensate the atoms comes from

- radiation pressure. For dense gases, emitted photons are re-scattered inside the cloud which effectively forms a repulsive force, so that the system expands;
- collisions can lead to light-induced losses.

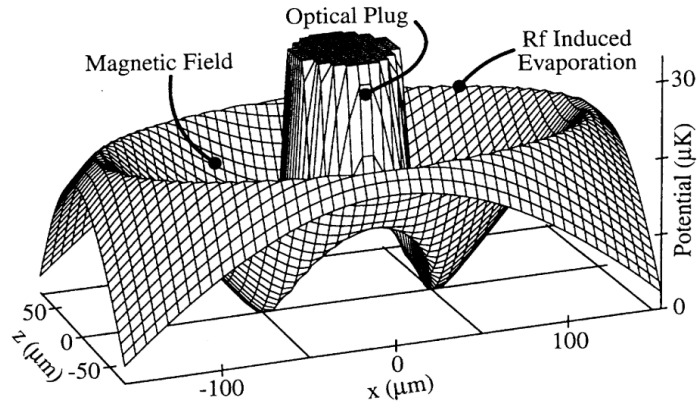


Figure 2.8: Quadrupole magneto-optical trapping with a plug in the center, taken from (Davis et al., 1995a).

Dipole traps vs. magnetic traps

- Pros: dipole traps are usually m_F -independent and has flexible geometry;
- Cons: dipole traps have smaller volume and depth, and the laser is more complicated than a B -field. Also there is residual photon scattering.

2.4 Evaporative cooling

For degeneracy of atoms at reachable densities, we need the temperature to be 100 nK or lower. This is usually not possible by optical cooling due to recoil and density limits; we can however do the cooling without photons, i.e., remove energy and entropy by removing some fraction of the atoms. The idea is to remove atoms with largest energy from the thermal distribution. The steps are:

1. trap the atoms and thermalize the atom gas;
2. apply "filter" process to remove high-energy fraction;
3. re-thermalize the gas to repopulate the high energy tail of distribution;
4. repeat 2-3.

Remove "hot" atoms In the low-density gas, atoms oscillate in the trap of depth V_0 . To trap the tail of Maxwell distribution, it is required that $V_0 \gg k_B T$. For evaporation, simply reduce V_0 so that $E_{\text{cut}} = V_0 \gtrsim k_B T$, and let the hot atoms whose energy larger than E_{cut} escape. For magnetic trap, it is to switch from low-field seeking states to untrapped states. We can use RF (radio frequency) fields that induce the transition at certain trap depth that only warm atoms can reach.

— **Remark** —

Continuous evaporation is also possible, which is usually done by reduce $E_{\text{cut}}(t)$ dynamically.

Efficiency We want to minimize the atom loss while maximizing the energy per removed particle. In this sense we should choose high E_{cut} . This is however constrained by the exponentially reduced rate of evaporation in E_{cut} ; the cooling speed has to be fast enough to be realistic in experiments and also to compensate residual heating. The limiting factors are

- thermalization rate, where *interaction* has to be investigated;
- the density needs to be high enough despite loss due to evaporation;
- contraction due to reduction in temperature can compensate or even *overcompensate* the reduction in density due to evaporative particle loss. If the center density increases during the evaporation, it is called *runaway / accelerating evaporation*.

Collisions The collision rate for one particle is

$$R_{\text{coll}} = \sigma \cdot v \cdot n, \quad (2.22)$$

where σ is the cross-section of collision, v is its velocity and n is the density of particles. Usually the thermalization of a gas requires *only a few* scattering events (1-3) per particle, which means

$$\tau_{\text{thermal}} \simeq 1/\sigma v n. \quad (2.23)$$

The collision process obeys the momentum and energy conservation laws. If the kinetic energy is also conserved, it is called *elastic* collision; otherwise it is *inelastic* collision. The latter case leads to heating and a change of internal state, which reduces the density of indistinguishable atoms. In the extreme case, the internal state changes from trappable to non-trappable, which causes loss of atoms! As a results, we want to choose states

- without spin-changing collisions (for magnetic traps);
- or of lowest energy configuration (these are however high-field seekers).

Even without spin and magnetic field, there are *molecule formations* for most atoms, specifically for all alkali atoms. The two-particle cases are forbidden by momentum and energy conservation laws, but with a third particle present, it can carry the binding energy as kinetic energy away. The three-body collision rate scales as n^2 ($\Gamma = K_3 n^2$), so for low densities, the 2-body collisions dominate (\Rightarrow metastable state). For a given density, smaller three-body collision parameter K_3 is better, like ^{87}Rb ($K_3 \approx 6 \times 10^{-30} \text{ cm}^6/\text{s}$) and ^{39}K ($K_3 \approx 1 \times 10^{-25} \text{ cm}^6/\text{s}$).

The ratio of "good" elastic collisions to "bad" inelastic collisions is important: we want

$$R_{\text{el}} \gg R_{\text{inel}}. \quad (2.24)$$

Therefore the density should be reduced until R_{inel} is minimized.

- The typical timescale for a particle to be hit by a background gas atom in typical vacuum chamber (of pressure $10^{-12} - 10^{-10}$ mbar).
- For typical densities of $10^{13} - 10^{14} \text{ cm}^{-3}$, the typical $R_{\text{inel}} \approx 10^{-1} \text{ s}^{-1} - 10^{-3} \text{ s}^{-1}$.

The evaporation process must be faster than this scale, and the typical evaporation time is $\approx 1 \text{ s} - 100 \text{ s}$. This density also define the *limitation* of degeneracy in evaporative cooling!

2.5 Absorption imaging

When we talk about atoms with low temperature T in a trap, how is T defined? How large is the cloud in the trap? What is the number of atoms? We generally use the time of flight (ToF) measurement. After preparation of gas in a trap, the trap is instantaneously switched off. Then we wait for some time ToF period t_{ToF} and measure the particle density. After ballistically releasing the atoms for a long time, the initial position becomes negligible and the distribution of velocities determines the density distribution. We can measure the velocity distribution through

$$n(\mathbf{x}) = n(\mathbf{v} \cdot t_{\text{ToF}}) \quad (2.25)$$

for $x_0 \ll v_{\text{typ}} t_{\text{ToF}}$. Here we assume *ballistic expansion*, that is, no interaction or collisions during the expansion. We expect to obtain the Bose-Einstein

distribution for indistinguishable bosons and Fermi-Dirac distribution for fermions. In the BEC case, the density is usually large enough such that interactions cannot be neglected for BEC fraction, both in trap and during expansion.

So the problem is reduced to particle density detection. Early methods are atom counting by fluorescence: let the illumination beam travel through the trapped atoms, where photons are absorbed and then released and fall; the fluorescence then detected. The intensity $I(t)$ is the only observable and only a small amount of light can be easily captured.

The standard method today is however *absorption imaging*.

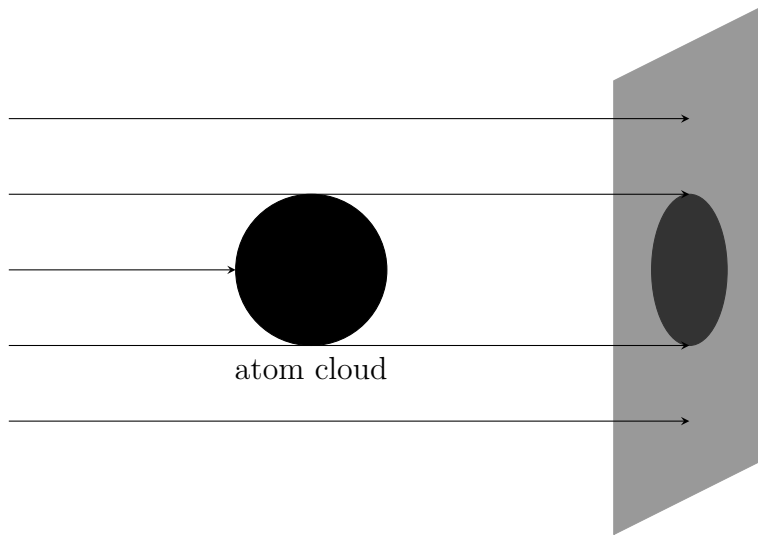


Figure 2.9: Absorption imaging

Light is absorbed as a function of the atom density and absorption cross-section. Along the propagation direction z , the absorption is

$$\frac{dI(x, y, z)}{dz} = -I(x, y, z)n(x, y, z)\sigma. \quad (2.26)$$

Integrate over z , and we get (*Lambert-Beer* absorption law)

$$I(x, y, z') = I(x, y, z_0) \exp\left(-\sigma \int_{z_0}^{z'} n(x, y, z) dz\right). \quad (2.27)$$

If all the constants are known, out observable is therefore the column density

$$n(x, y) = \int n(x, y, z) dz. \quad (2.28)$$

Now it is possible to measure the temperature through ToF.

2.6 Journal Club 1: Molasses cooling (Chu et al., 1985)

This paper is about pretty much the first experiments on optical molasses, just before the sub-Doppler cooling effect was discovered. It is nice and short, and uses the classical structure of a paper. See paper below.

- *What is the selling point of this paper?*

They confines sodium atoms in a small region for times on the order of 0.1 sec, and cool them to $\sim 240_{-60}^{+200}$ μK . Before it could be done up to 50 mK in three-dimensional for a short time.

- *What is the cooling scheme?*

They use first a counterpropagating laser to cool a pulsed sodium beam from $\sim 2 \times 10^4 \text{ cm s}^{-1}$ to $\sim 2 \times 10^3 \text{ cm s}^{-1}$ within 5 cm. Then the atoms can then be captured by the optical molasses and Doppler cooled.

- *What are actually detected?*

Fluorescence signals (from six pulses) are measured. They measure the number of atoms remaining in a certain area after switching off the lasers for some time periods (switch on the lasers again to measure). The diffusion constant D can be extracted after many experiments, which is dependent on the temperature T in the time of flight process.

Three-Dimensional Viscous Confinement and Cooling of Atoms by Resonance Radiation Pressure

Steven Chu, L. Hollberg, J. E. Bjorkholm, Alex Cable, and A. Ashkin

AT&T Bell Laboratories, Holmdel, New Jersey 07733

(Received 25 April 1985)

We report the viscous confinement and cooling of neutral sodium atoms in three dimensions via the radiation pressure of counterpropagating laser beams. These atoms have a density of about $\sim 10^6 \text{ cm}^{-3}$ and a temperature of $\sim 240 \mu\text{K}$ corresponding to a rms velocity of $\sim 60 \text{ cm/sec}$. This temperature is approximately the quantum limit for this atomic transition. The decay time for half the atoms to escape a $\sim 0.2\text{-cm}^3$ confinement volume is $\sim 0.1 \text{ sec}$.

PACS numbers: 32.80.Pj

The deflection of atoms by light resonant with an atomic transition was observed as early as 1933 by Frisch.¹ Much later Ashkin² pointed out that laser light can exert a substantial scattering force on an atom. He raised the possibility that this force could be used to trap atoms, and subsequently there have been numerous proposals to cool and ultimately trap neutral atoms.³ Various experiments have been proposed that would utilize trapped atoms; these generally require long observation times and/or low atomic velocities. We report the demonstration of a confinement scheme based on the damping of atomic velocities. This scheme is not a trap, but can confine atoms in a small region in space for times on the order of 0.1 sec, and cool them to $\sim 240 \mu\text{K}$, the quantum limit for our experimental conditions. For comparison, we note that two-dimensional radiative cooling has reduced the temperatures transverse to the motion of an atomic beam from 40 to 3.5 mK ,⁴ and atomic beams stopped by light have resulted in three-dimensional temperatures of 50–100 mK.⁵ Laser cooling of electromagnetically trapped ions has resulted in ion temperatures between 5 and 100 mK.⁶

The basic physics of the viscous damping scheme is briefly outlined. Consider an atom irradiated by a laser beam tuned near a resonance line. For each photon absorbed, an atom receives a net change of momentum $\Delta p = h/\lambda$, where λ is the wavelength. Since the subsequent reemission of the photon has no preferred direction, an average of many scattering events gives a net scattering force along the direction of the light.² Hänsch and Schawlow⁷ noted that if counterpropagating beams were tuned to the low-frequency side of the absorption line, there would always be a net force opposing the velocity of an atom. For example, an atom moving with velocity $+v_x$ will blue shift into resonance with a laser beam propagating towards $-\hat{x}$ and red shift out of resonance with the laser beam propagating towards $+\hat{x}$. Thus, the atom is more likely to absorb photons going towards $-\hat{x}$. With the use of six beams along $\pm\hat{x}$, $\pm\hat{y}$, and $\pm\hat{z}$ and an averaging over many absorptions, the net effect is a viscous damping

force $\mathbf{F} = -\alpha\mathbf{v}$ opposite the velocity of the atom. The cooling rate is $\mathbf{v}\cdot\mathbf{F} = -\alpha v^2$. The expression for the damping force which includes standing waves and saturation has been previously derived.⁸

In addition to the average force, statistical fluctuations must be considered.⁹ These fluctuations lead to heating. For a simple picture of the fluctuations, consider the momentum impulses on an atom due to the absorption and emission of photons. In the absence of damping, the atoms will execute a random walk in velocity, and although $\langle v \rangle = 0$, $\langle v^2 \rangle$ will increase linearly with the total number scattered photons. Increasing $\langle v^2 \rangle$ corresponds to heating, as first observed by Bjorkholm *et al.*¹⁰ If we equate the heating and cooling terms, the steady-state kinetic temperature is obtained. In the absence of stimulated processes, the minimum kinetic energy for a two-level atom is given by $kT = \frac{1}{4}h\gamma$, where γ is the width (FWHM) of the absorption line. If one includes stimulated processes, the minimum temperature is increased by a factor of 2.⁸ For sodium, $\gamma = 10 \text{ MHz}$ and $T_{\min} = 240 \mu\text{K}$.

An estimate of the confinement time can be obtained by the observation that the motion of atoms in a viscous fluid of photons ("optical molasses") is analogous to diffusion in classical Brownian motion. The diffusion constant D is given by the Einstein relation $D = kT/\alpha$, and for an infinite medium, $D = \langle x^2 \rangle/2t$, where $\langle x^2 \rangle$ is the mean square displacement after time t . However, an analysis based on an infinite medium overestimates the storage time. A more appropriate model is a viscous fluid surrounded by a spherical boundary (defined by the extent of the laser beams) such that the atoms that reach the boundary escape. If we assume an initial uniform concentration of atoms n_0 , the average concentration \bar{n} has been shown¹¹ to vary as

$$\bar{n} = n_0 \frac{6}{\pi^2} \sum_{v=1}^{\infty} \frac{1}{v^2} e^{-D\pi^2 v^2 t/R^2}. \quad (1)$$

The spherical-boundary modification of the random-walk analysis reduces the storage time for our experimental conditions by a factor of 3.1.

The experimental apparatus is schematically shown in Fig. 1. We use a pulsed atomic beam source in order to simplify diagnostics. The beam of sodium atoms is produced by irradiation of a pellet of sodium metal with a ~ 10 -nsec pulse from a frequency-doubled Nd-YAIG laser (~ 30 -mJ pulse focused to $\sim 5 \times 10^{-2} \text{ cm}^2$). A hot plasma is formed which produces sodium ions, suprathermal atoms with average energy of ~ 3.5 eV, and a small fraction of thermal atoms at ~ 1000 K. The source of atoms is apertured to produce a directed 0.6-cm-diam atomic beam at the confinement region shown in Fig. 1.

Since our "optical molasses" can only capture atoms moving with velocities $\lesssim 3 \times 10^3$ cm/sec, we slow some of the atoms in the atomic beam by using a counterpropagating laser beam. Following Ertmer *et al.*,⁵ we use an electro-optic modulator to generate a frequency-shifted sideband which can be swept in frequency to stay in resonance with the changing Doppler shift of the atomic resonance frequency as the atoms slow down. The laser intensity used to slow (precool) the atoms is ~ 120 mW/cm². Atoms with initial velocities of $\sim 2 \times 10^4$ cm/sec and less are slowed down in less than 5 cm to velocities $\sim 2 \times 10^3$ cm/sec. After slowing for 0.5 msec, the precooling beam is shut off by an acoustic-optic modulator, and the atoms then drift into the region defined by the six intersecting laser beams where they are cooled and viscously confined. The precooling laser beam and the confining beams are obtained from the combined beams of two cw actively stabilized, ring dye lasers. The lasers are operated at frequencies differing by ~ 1.7 GHz to prevent optical pumping of the sodium ground state.

The power of each confining beam is between 4 and 20 mW, and the beam radius is $w_0 = 0.36$ cm. Despite the fact that the vast majority of atoms are not slowed down, the pulsed beam is sufficiently intense that confinement densities on the order of 10^6 atoms/cm³ are obtained. At these densities, the cloud of confined atoms is clearly visible by eye.

An averaged fluorescence signal (sixteen pulses) as a function of time is shown in Fig. 2. Pulse-to-pulse amplitude fluctuations are $\sim 30\%$. The initial abrupt spike is due to fast atoms passing rapidly through the interaction region. The baseline is the scattered light level obtained by blockage of the precooling beam. If any of the confining dimensions is blocked, a fluorescence pulse $\lesssim 1$ msec long is seen as a result of the passage of the slowed atoms through the interaction region. In addition, the laser frequencies must be tuned to the low-frequency side of the absorption lines and be critically tuned with respect to each other. In Fig. 2, we plot the number of atoms remaining in the observation region as a function of Dt/R^2 , where D is the diffusion constant, t is the time, and R is an effective radius to the spherical boundary. We extract a value for D by scaling the horizontal axis of the experimental data to match to the theoretical decay given by Eq. (1). If we take $R = 0.4$ cm (where the intensity of the laser beam is ≈ 0.1 of the peak intensity), the decay curves give us an effective diffusion constant, D_{eff} . Using a computed value of $\alpha = \alpha_{\text{max}} = 5.8 \times 10^{-18}$ g/sec,⁸ we obtain an upper limit on the temperature of $T_{\text{max}} = D_{\text{eff}}\alpha_{\text{max}}/k = 1.9$ mK. The actual temperature is expected to be lower since we have ignored drift velocities due to beam intensity imbalance, intensity

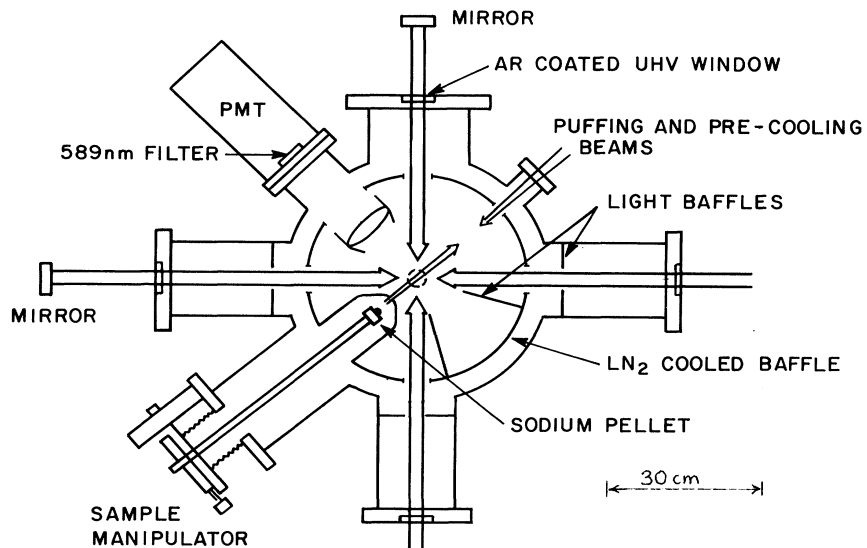


FIG. 1. Schematic of the vacuum chamber and intersecting laser beams and atomic beam. The vertical confining beam is indicated by the dashed circle. The "puffing" beam is from the pulsed YAIG laser.

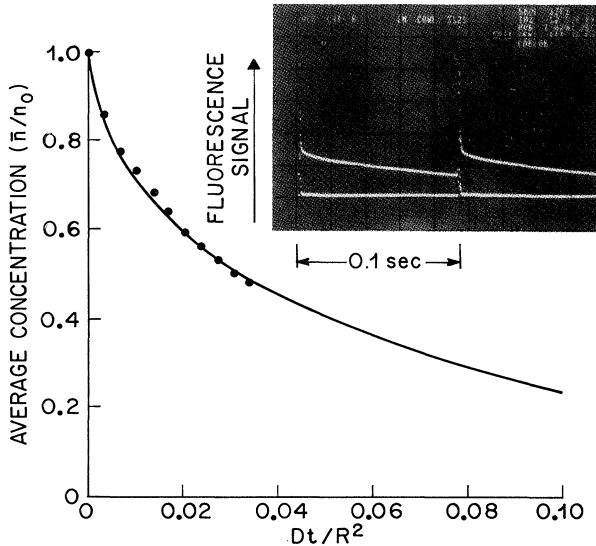


FIG. 2. Fluorescence signal as a function of time is shown in the inset. The baseline shows the scattered light level. The confinement region is loaded every 0.1 sec, governed by the repetition rate of the YAG laser. The fraction of atoms remaining in the observation region is plotted as a function of Dt/R^2 . The solid line is the theoretical calculation based on the modified random walk.

hot spots, and beam misalignment, all of which increase D_{eff} but do not substantially increase the temperature of the atoms. For example, if the counterpropagating beams are imbalanced by 2%, the drift velocity is $v_{\text{drift}} = 3 \text{ cm/sec}$, and the storage time will be $R/v_{\text{drift}} \sim 0.13 \text{ sec}$.

A direct measurement of the temperature of the cooled atoms is obtained by a time-of-flight technique. After a 15-msec cooling and confinement time, all six beams are turned off in $\sim 0.1 \text{ msec}$ and left off for a variable time. During that time, the atoms will leave the observation region ballistically with their instantaneous velocities. We show in the inset of Fig. 3 an example time-of-flight measurement for a 9.1-msec light-off time. Given an initial uniform spherical distribution of atoms with a Maxwell-Boltzmann distribution of velocities, we calculate the fraction of atoms remaining in the observation region as a function of the light-off time. To fit the data with calculated decay curve, we introduce a 1.4-msec time shift in the theoretical curve to account for the fact that the actual atomic distribution will be depleted near the edge of the sphere by Brownian diffusion to the escape boundary.¹¹ The measured fraction of atoms remaining and the theoretical curve are plotted in Fig. 3. Additional uncertainty in the temperature measurement arises from the fact that our Gaussian-type beam profiles must be convoluted with saturation effects and the acceptance volume of our phototube. Note that the tem-

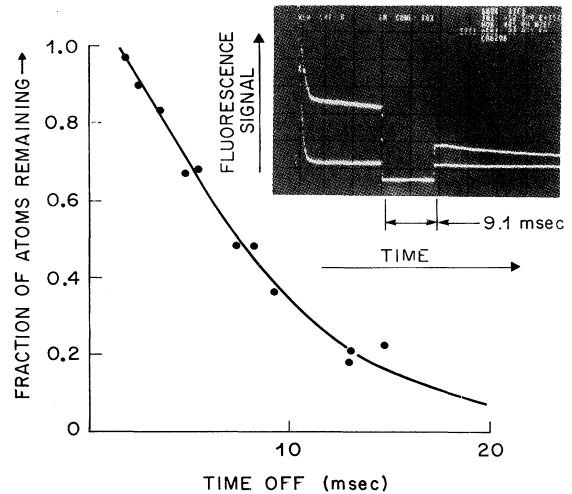


FIG. 3. Inset shows the effect of blocking the confining laser beams 15 msec after the YAG laser fires. The horizontal trace is the scattered light level. The fraction of atoms remaining is plotted as a function of the time-off period. The solid line is the theoretical curve.

perature depends on R_{eff}^2 , where R_{eff} is an effective observation radius. Using a fairly conservative value of $R_{\text{eff}} = 0.4 \text{ cm}$, we obtain $T = 240 \pm 200 \mu\text{K}$.

In summary, we have confined sodium atoms in a $\sim 0.2\text{-cm}^3$ volume for times on the order of 0.1 sec and cooled them to temperatures approaching the quantum limit. These kinetic temperatures are significantly lower than the electromagnetically trapped ions⁶ or stopped atoms⁵ previously reported. The low velocities and long confinement times that we have achieved can increase the observation and/or coherence time for atoms, opening up new possibilities in areas such as collisions, quantum statistics, and precision spectroscopy. In addition, the low temperatures make possible the efficient loading of atom traps. Such traps will help in reaching higher densities and possibly temperatures as low as 10^{-6} K .³ At these temperatures, the de Broglie wavelength of the atoms is on the order of $1 \mu\text{m}$. Even modest densities of these ultracold atoms (which can be either fermions or bosons) should reveal interesting physics.

We acknowledge helpful discussions with J. P. Gordon and assistance from L. Buhl in the preparation of the LiTaO₃ crystal used in the electro-optic modulator.

¹O. R. Frisch, Z. Phys. **86**, 42 (1933).

²A. Ashkin, Phys. Rev. Lett. **24**, 156 (1970), and **25**, 1321 (1970).

³See, for example, A. Ashkin, Science **210**, 1081 (1980), and Prog. Quantum Electron. **8**, 204 (1984); for recent proposals, see D. E. Pritchard, Phys. Rev. Lett. **51**, 1336

(1983); A. Ashkin, Opt. Lett. **9**, 454 (1984); J. Dalibard, S. Reynaud, and C. Cohen-Tannoudji, J. Phys. B **17**, 4577 (1984).

⁴V. I. Balykin, V. S. Letokhov, and A. I. Sidorov, Pis'ma Zh. Eksp. Teor. Fiz. **40**, 251 (1984) [JETP Lett. **40**, 1026 (1984)].

⁵J. Prodan, A. Migdall, W. D. Phillips, I. So, H. Metcalf, and J. Dalibard, Phys. Rev. Lett. **54**, 992 (1985); W. Ertmer, R. Blatt, J. L. Hall, and M. Zhu, Phys. Rev. Lett. **54**, 996 (1985).

⁶W. Neuhauser, M. Hohenstatt, P. E. Toschek, and H. Dehmelt, Phys. Rev. A **22**, 1137 (1980); D. J. Wineland and W. M. Itano, Phys. Lett. **82A**, 75 (1981); W. Nagourney, G. Janik, and H. Dehmelt, Proc. Natl. Acad. Sci. U.S.A. **80**, 643 (1983).

⁷T. W. Hänsch and A. L. Schawlow, Opt. Commun. **13**, 68 (1975).

⁸J. P. Gordon and A. Ashkin, Phys. Rev. A **21**, 1606 (1980); R. J. Cook, Phys. Rev. A **20**, 224 (1979), and Phys. Rev. Lett. **44**, 976 (1980).

⁹A. Yu. Pusep, Zh. Eksp. Teor. Fiz. **70**, 851 (1976) [Sov. Phys. JETP **43**, 441 (1976)]; V. S. Letokhov, V. G. Minogin, and B. D. Pavlik, Zh. Eksp. Teor. Fiz. **72**, 1328 (1977) [Sov. Phys. JETP **45**, 698 (1977)]; J. L. Picqué, Phys. Rev. A **19**, 1622 (1979); D. J. Wineland and W. M. Itano, Phys. Rev. A **25**, 35 (1982).

¹⁰J. E. Bjorkholm, R. R. Freeman, A. Ashkin, and D. B. Pearson, Opt. Lett. **5**, 111 (1980).

¹¹N. A. Fuchs, *The Mechanics of Aerosols* (Pergamon, Oxford, 1964), pp. 193–200.

2.7 Journal Club 2: Evaporative cooling (Davis et al., 1995b)

- *What is the selling point of this paper?*

They use rf-induced evaporative cooling to cool sodium atoms to $17 \mu\text{K}$, which is much closer to the degeneracy limit (required for BEC) compared with the limit of sub-Doppler cooling $200 \mu\text{K}$.

- *What is the cooling scheme?*

They first do a Zeeman slowing and Doppler cooling is then loaded. They afterwards use a quadrupole magnetic trap to do evaporative cooling. Absorption imaging is applied to measure the column density after ToF.

- *How do they determine the elastic cross sections in absorption imaging?*

They do one-dimensional heating to an atom cloud, and let it achieve equilibrium again. During this period, the aspect ratio of the width of the cloud in two dimensions is measured, so that the $1/e$ relaxation time τ can be calculated. Monte Carlo simulations gives that the elastic cross section satisfies $n_{\text{eff}}\sigma v = 2.7/\tau$, where $n_{\text{eff}} = \int dV n^2 / \int dn = n_0/8$.

- *What causes the shape of optical density in Fig.2 (a)?*

The magnetic field causes a shift in the level spacing, which changes the resonant frequency. That at somewhere away from the middle the light beams are more resonant causes an amplification of optical density.

Evaporative Cooling of Sodium Atoms

Kendall B. Davis, Marc-Oliver Mewes, Michael A. Joffe, Michael R. Andrews, and Wolfgang Ketterle

*Department of Physics and Research Laboratory of Electronics, Massachusetts Institute of Technology,
Cambridge, Massachusetts 02139*

(Received 28 December 1994)

We have observed evaporative cooling of magnetically trapped sodium atoms. A novel technique, rf induced evaporation, was used to reduce the temperature by a factor of 12 and increase the phase space density by more than 2 orders of magnitude. The elastic collision cross section of cold sodium atoms in the $F = 1, m_F = -1$ hyperfine state was determined to be $6 \times 10^{-12} \text{ cm}^2$, which implies a positive value of the scattering length.

PACS numbers: 32.80.Pj, 42.50.Vk

Cooling neutral atoms to submicrokelvin temperatures offers the exciting possibility of studying novel phenomena at long de Broglie wavelengths, most notably quantum degeneracy effects. Furthermore, such cold atoms are promising for a host of scientific applications such as precision measurements, high resolution atom lithography, and atom interferometry. Recently, several techniques have been demonstrated which allow the cooling of atoms to temperatures below the recoil limit. Optical techniques such as velocity selective coherent population trapping [1] and Raman cooling [2] have achieved subrecoil temperatures in one or two dimensions. They work best at low atomic densities. At high densities, temperature and density are eventually limited by the absorption of incident or scattered light [3,4] and by heating and trap loss due to excited state collisions [5]. The technique of forced evaporative cooling relies on collisional thermalization and has no recoil limit to overcome; therefore it seems ideally suited to reaching very low temperatures in dense atomic samples. Unfortunately, it requires high initial densities which could until recently only be prepared by cryogenic methods applicable solely to atomic hydrogen [6,7].

In this paper we elaborate on our initial demonstration of evaporative cooling for an atom different from hydrogen, Na [8], that was contemporaneous with the announcement of similar results in Rb [9]. Very recently, evaporative cooling of Na has also been observed in an optical trap [10]. By using a combination of different cooling and trapping techniques involving lasers and magnetic fields we were able to obtain the high initial density required for evaporative cooling. This closes the gap between optical cooling at relatively low density and collisional cooling which requires high density, and frees evaporative cooling from the restrictions of a cryogenic environment by using laser cooling as the precooling stage. Furthermore, it has been pointed out that alkali atoms have advantages for evaporative cooling due to the large elastic cross section [11].

Evaporative cooling requires the selective removal of the most energetic atoms from the trap. When the remaining atoms rethermalize there is a net cooling effect [12]. The selection of evaporating atoms is usually

done by lowering the height of the trapping potential [6]. Using this scheme in a spherical quadrupole trap would weaken the confinement, thus lowering the density and slowing down the evaporation process. This can be avoided in more complicated trapping geometries [6], but the spherical quadrupole trap provides the tightest confinement and therefore has advantages for evaporative cooling [13]. In this paper, we demonstrate a novel evaporation technique, rf induced evaporation, which was originally suggested in Ref. [14]. Atoms are removed from the trap by inducing an rf transition to an untrapped state without varying the trapping potential. Using this technique we observed strong evaporation of magnetically trapped sodium atoms lowering the temperature by a factor of 12 and increasing the phase space density by a factor of more than 100.

A high density of magnetically trapped atoms is obtained in a multistep procedure. Atoms were initially slowed in a Zeeman slower and loaded into a dark SPOT [3]. Typically, 10^9 to 10^{10} atoms were confined at densities of $5 \times 10^{11} \text{ cm}^{-3}$. Sub-Doppler temperatures of $100 \mu\text{K}$ were achieved by turning off the weak quadrupole magnetic field and applying a dark version of polarization gradient cooling. By employing very weak repumping sidebands, the density of atoms in the $F = 2$ state is kept low enough to avoid absorption of the cooling light. This method should avoid heating effects due to high optical density as observed in Cs [15]. The laser light was quickly (<1 ms) shut off and a magnetic quadrupole field of 100 G/cm switched on. Care was taken to provide a magnetic potential which is neither too steep (which would add too much potential energy, causing heating) nor too shallow (which would result in a loss of density as the cloud expands). The density in the magnetic trap is a factor of 10 lower than in the light trap because only about one-third of the atoms are in the trapped $F = 1, m_F = -1$ state, and because of some expansion of the cloud. Subsequently, the magnetic field gradient was increased to 1000 G/cm .

Adiabatic increase of a linear potential by a factor of η results in an increase in density by a factor of η and in temperature by a factor of $\eta^{2/3}$. The adiabaticity of the

compression was verified by expanding the cloud again and retrieving the initial temperature to within 10%. The adiabatic increase of the field gradient by a factor of 10 led to an enhancement of the elastic collision rate by a factor of 20 which was crucial for obtaining fast evaporation. The sample of atoms prepared in this way had typically 8×10^8 atoms at a peak density of 5×10^{11} and a temperature of 1 mK.

The number, the density, the temperature, and, also, the spatial distribution of the trapped atoms were determined by absorption imaging. Identical results obtained with two successive images of the same atoms verified that the probing was nonperturbative. Indeed, the number of absorbed photons was much less than one per atom. Atoms in our spherical quadrupole trap oscillate with an effective frequency on the order of kHz. This makes it rather difficult to *suddenly* switch off the magnetic trap and image the atoms at zero magnetic field. Therefore, the absorption images were taken *in situ* inside the magnetic trap and were compared to simulations that included the full hyperfine Hamiltonian and the varying magnetic field direction with respect to the probe polarization [16]. If the probe frequency is in resonance with a Zeeman shifted hyperfine transition in the spatial wings of the cloud, the absorption image appears wider. However, identical temperatures and densities were obtained from the fits to images taken with different probe frequencies.

The major goal of this multistep procedure of cooling and compressing atoms was to obtain a sample of magnetically trapped atoms with an elastic collision rate much higher than the loss rate due to background gas collisions. A residual pressure of about 5×10^{-11} mbar resulted in a trapping time of 30 s. In previous work [17] the time between collisions and the trapping time were both approximately 15 s. For our highest density samples, the average time between collisions was 20 ms (see below), resulting in 1500 collisions per trapping time, more than sufficient to study elastic collisions and observe evaporative cooling.

The driving process for evaporative cooling is elastic collisions. For submillikelvin sodium atoms only one or two partial waves (*s* and *d* wave) contribute to the scattering. Depending on the *s*-wave scattering phase shift, the zero-temperature cross section varies between zero and infinity. The phase shift depends critically on the binding energy of the last bound vibrational level and is very sensitive to fine details of the interaction potential.

We were able to deduce the elastic collision cross section by observing the thermalization of an atom cloud. For this a nonthermal distribution was prepared by temporarily displacing the trap center by about 1 mm along the symmetry axis (*z* axis). This was accomplished by suddenly imbalancing the current through the two solenoids of the spherical quadrupole trap. Within 100 ms, anharmonicities lead to dephasing of the initial oscillations, resulting in a cloud which was elongated along the *z* direction. Using absorption imaging, the

relaxation of the anisotropic energy distribution was observed by recording the shape of the cloud as a function of time [17]. In principle, equilibration might happen due to the ergodic evolution of orbits in the trap independent of collisions. However, Monte Carlo simulations showed that the spherical quadrupole trap is nonergodic for periods of at least 10 s. In addition, we lowered the density by a factor of 12 by optically pumping atoms to non-trapped states using off resonant laser light, and found the $1/e$ relaxation time τ to be inversely proportional to the product of peak density n_0 times velocity (Fig. 1). From that we estimate a lower bound for the ergodic mixing time of 30 s, completely negligible to the observed relaxation time of 1 s. Note that we determined relaxation times for the uncompressed cloud. Assuming constant elastic cross section, adiabatic compression to the maximum field gradient reduced the relaxation time to about 50 ms, comparable to the dephasing time.

According to calculations by Snoke and Wolfe it takes five elastic collisions for complete thermalization [18]. Monte Carlo calculations gave 2.7 for the ratio of elastic collision rate to the relaxation rate $1/\tau$ which describes the cross-sectional relaxation of a cloud with an anisotropic energy distribution [17].

We determine the elastic cross section σ from the equation $n_{\text{eff}} \sigma v = 2.7/\tau$, where $v = 4(k_B T / \pi m)^{1/2}$. The effective density is defined by $n_{\text{eff}} = \int n^2(\mathbf{r}) dV / \int n(\mathbf{r}) dV$, which is $n_0/8$ for an equilibrium distribution in a linear potential. The result is $\sigma = (6.0 \pm 3.0) \times 10^{-12} \text{ cm}^2$ for the elastic cross section. The estimated uncertainty mainly reflects three standard deviations of the fit with smaller contributions from the determinations of density and temperature.

The measurement was preformed at $200 \mu\text{K}$, well below the temperature at which one expects *d*-wave

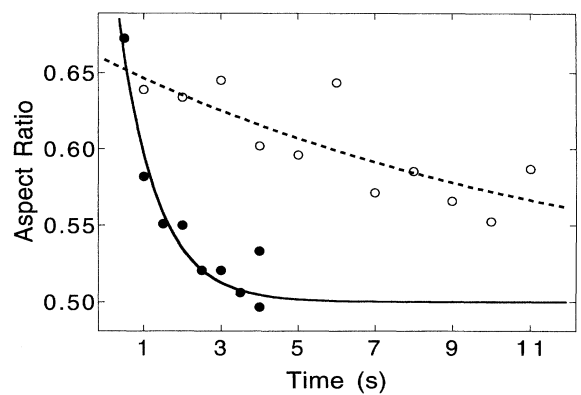


FIG. 1. Thermal relaxation of an atom cloud after one-dimensional heating. The figure shows the time variation of the aspect ratio of the cloud for two different initial densities (solid circles: $5 \times 10^{10} \text{ cm}^{-3}$; open circles: $4 \times 10^9 \text{ cm}^{-3}$). The lines represent simple exponential fits with time constants of 1.0 and 13 s, respectively.

contributions or a temperature dependence of the s -wave cross section [19,20]. We can therefore deduce the scattering length $a = \pm(92 \pm 25)a_0$ using the relation $\sigma = 8\pi a^2$.

Recently, accurate calculations of the scattering length of cold sodium atoms have been performed [21,22]. For sodium atoms in the $F = 1$, $m_F = 1$ state the result was $56a_0 < a < 154a_0$, and for an alternative choice of potentials $-36a_0 < a < 154a_0$ [21]. Thus negative values of the scattering length which would result in an unstable Bose condensate could not be ruled out. Our experimental result, together with the theoretical prediction, shows that sodium in the $F = 1$, $m_F = -1$ state has a large positive scattering length and is therefore an ideal choice for the pursuit of Bose-Einstein condensation in alkali atoms.

In rf induced evaporation, atoms are spin flipped to an untrapped state when they are in resonance with an applied rf field. Because this resonance frequency is a function of magnetic field B , atoms are selectively removed at a specific value of B . In the case of transitions between magnetic sublevels m_F one has $\omega_{\text{rf}} = |g|\mu_B B/\hbar$, where g is the g factor. Since the trapping potential is given by $m_F g \mu_B B(\mathbf{r})$, only atoms which have a total energy $E > \hbar\omega_{\text{rf}}|m_F|$ will evaporate, or, in other words, application of rf radiation of frequency ω_{rf} creates a trap lip with a height of $\hbar\omega_{\text{rf}}|m_F|$. An advantage is that the "lip" exists over a large surface rather than a small surface saddle point region of the trap [6].

For a more detailed description of the evaporation process one has to use the dressed-atom formalism to obtain the eigenvalues of an atoms in a combined magnetic and rf field. These solutions represent the adiabatic potential for the motion of the atoms. Slowly moving atoms follow the avoided crossing and stay on the lowest potential surface. The "spin-flip" process is a two-photon adiabatic transition from a trapped to an untrapped state. If, as in our experiments, the strength of the rf magnetic field is not strong enough to ensure adiabaticity, one has to use Landau-Zener probabilities for spin flips at the avoided crossings. The evaporation of atoms saturates when the Landau-Zener probability is comparable to the ratio of oscillation time to equilibration time.

Forced evaporative cooling requires a continuous decrease of the potential depth to maintain it at an optimum value proportional to the decreasing temperature [12]. This was accomplished by ramping down the rf frequency. If the rf frequency changes too quickly, the atomic distribution is only truncated without increase in phase-space density; if it changes too slowly, more atoms than necessary are lost due to background gas collisions during the evaporation. The optimum result is obtained when the rf sweep keeps pace with the collisional thermalization [13,23]. As discussed in Ref. [24] the phase-space density increase in evaporative cooling is due to the combined effect of truncation and collisions; neither process alone would increase phase-space density.

Forced evaporation can also be obtained by adiabatically compressing the atoms at fixed rf frequency. We used a combination of both methods. After the initial loading a constant rf frequency of 30 MHz was applied and the magnetic field gradient increased by a factor of 10 in 1 s. With the rf off, this increased the temperature by a factor of 5, whereas with evaporative cooling the temperature went up by only 20%. Subsequently, the rf frequency was reduced linearly to 7 MHz within 200 ms. The temperature and density of the cloud were probed at various stages of the evaporation process after decompression to the initial field gradient. This ensured identical conditions for probing atoms and avoided very high optical densities and small clouds.

The results are shown in Fig. 2. We observed temperature reduction by a factor of 12 and a simultaneous increase in density by a factor of 4.6, resulting in an increased phase space density by a factor of 190. This means that the elastic collision rate, which is proportional to $n\nu$, was increasing during evaporation. At the intermediate stage of evaporation in Fig. 2, the elastic collision rate had doubled and then went down slightly, probably due to the loss of atoms by Majorana flops (see below). This means we are already in the regime of self-accelerating evaporation.

Indeed, one expects runaway evaporation when the number of collisions during a trapping time exceeded 25 [13]. With an estimated collision rate of 50/s in the compressed cloud we exceed this value by a factor of about 60. The cloud after evaporation had a temperature of $80 \mu\text{K}$ and a density of $2 \times 10^{12} \text{ cm}^{-3}$, as inferred from $17 \mu\text{K}$ and $1.8 \times 10^{11} \text{ cm}^{-3}$ measured after adiabatic de-

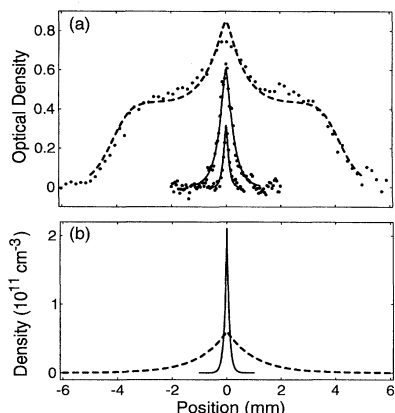


FIG. 2. Optical density (a) and density (b) before and after evaporative cooling. (a) The initial cloud was cooled by adiabatic compression at constant rf frequency (middle trace) and further cooled by decreasing the rf frequency. The lines are fits to the observed profiles. The "bumpy" structure of the initial profile is a result of Zeeman shifts of the transitions used for probing the atoms. (b) Density before and after evaporation as obtained from the fits to the optical density profiles (temperatures are 200 and $17 \mu\text{K}$, respectively).

compression. The uncertainties on temperature and density are estimated to be 10% and 20%, respectively. Our final phase-space density is 2×10^4 times smaller than that required for Bose-Einstein condensation.

The current limitation of our evaporative cooling is an observed increased trap loss for small atom clouds. For the coldest temperatures achieved, the trapping time decreases from 30 s to a few seconds. This is most probably due to Majorana flops, nonadiabatic transitions to an untrapped state which happen in the center of the trap near the zero of the magnetic field. It may be shown that this loss rate is proportional to the ratio of the area of the "nonadiabatic" region around the center to the cross-sectional area of the cloud. From a Landau-Zener model we estimate the lifetime to be $500d^2$ (in seconds), where d is the cloud diameter in mm. The observed decrease in trapping time for cloud sizes of $100 \mu\text{m}$ is in qualitative agreement with this model.

In conclusion, we have evaporatively cooled alkali atoms and increased the phase-space density by more than 2 orders of magnitude. We have achieved the initial conditions necessary for accelerated evaporation and identified nonadiabatic transitions in the center of the trap as the current limitation. Further progress should be possible after transferring the atoms into a trap with a different field geometry which does not have magnetic field in the center.

This work was supported by the Office of Naval Research and Air Force Office of Scientific Research through Grant No. N00014-90-J-1642, the Joint Service Electronics Program, and the Sloan Foundation. M.-O.M. and K.B.D. would like to acknowledge support from Studienstiftung des Deutschen Volkes and the MIT Physics Department Lester Wolfe fellowship, respectively. The authors are grateful to D.E. Pritchard for many useful discussions and to I.A. Entin for experimental assistance.

- [1] J. Lawall *et al.*, Phys. Rev. Lett. **73**, 1915 (1994).
- [2] N. Davidson, H.-J. Lee, M. Kasevich, and S. Chu, Phys. Rev. Lett. **72**, 3158 (1994).
- [3] W. Ketterle, K. B. Davis, M. A. Joffe, A. Martin, and D. E. Pritchard, Phys. Rev. Lett. **70**, 2253 (1993).

- [4] T. Walker, D. Sesko, and C. Wieman, Phys. Rev. Lett. **64**, 408 (1990).
- [5] T. Walker and p. Feng, in "Advances in Atomic, Molecular, and Optical Physics," edited by B. Bederson and H. Walther (to be published).
- [6] N. Masuhara *et al.*, Phys. Rev. Lett. **61**, 935 (1988).
- [7] I. D. Setija *et al.*, Phys. Rev. Lett. **70**, 2257 (1993).
- [8] K. B. Davis, M.O. Mewes, M.A. Joffe, and W. Ketterle, in Fourteenth International Conference on Atomic Physics, Boulder Colorado, 1994, Book of Abstracts (to be published) Abstract No. 1-M3.
- [9] W. Petrich, M.H. Anderson, J.R. Ensher, and E.A. Cornell, in *Fourteenth International Conference on Atomic Physics, Boulder Colorado, 1994* (Ref. [8]).
- [10] M. Kasevich (private communication).
- [11] E. Tiesinga, A.J. Moerdijk, B.J. Verhaar, and H.T.C. Stoof, Phys. Rev. A **46**, R1167 (1992).
- [12] H. F. Hess, Phys. Rev. B **34**, 3476 (1986).
- [13] K. B. Davis, M.-O. Mewes, and W. Ketterle, Appl. Phys. B **60**, 155 (1995).
- [14] D.E. Pritchard, K. Helmerson, and A.G. Martin, in *Proceedings of the 11th International Conference on Atomic Physics*, edited by S. Haroche, J.C. Gay, and G. Grynberg (World Scientific, Singapore, 1989), p. 179.
- [15] M. Drewsen *et al.*, Appl. Phys. B **59**, 283 (1994).
- [16] O.J. Luiten *et al.*, Phys. Rev. Lett. **70**, 544 (1993).
- [17] C.R. Monroe, E.A. Cornell, C.A. Sackett, C.J. Myatt, and C.E. Wieman, Phys. Rev. Lett. **70**, 414 (1993).
- [18] D.W. Snoke and J.P. Wolfe, Phys. Rev. B, **39** 39 (1989).
- [19] A.-J. Moerdijk and B.J. Verhaar (private communication).
- [20] This does not contradict the observation of d -wave scattering in recent photoassociation experiments at 0.6 mK [L.P. Ratliff *et al.*, J. Chem. Phys. **101**, 2638 (1994)]. Since the ratio of d - and s -wave partial cross sections scales as T^2 in inelastic scattering, the d -wave contribution to photodissociation at $200 \mu\text{K}$ should be less than 10%, and even smaller for elastic scattering which requires two passages through the centrifugal barrier.
- [21] A.J. Moerdijk and B.J. Verhaar, Phys. Rev. Lett. **73**, 518 (1994).
- [22] R. Côté and A. Dalgarno, Phys. Rev. A **50**, 4827 (1994).
- [23] J.M. Doyle *et al.*, Physica (Amsterdam) **194-196B**, 13 (1994).
- [24] W. Ketterle and D.E. Pritchard, Phys. Rev. A **46**, 4051 (1992).

Chapter 3

Ideal Bose Gas and Bose-Einstein Condensation

3.1 Ideal gas in phase space

Write the single-particle Hamiltonian

$$H_0(\mathbf{r}, \mathbf{p}) = \frac{\mathbf{p}^2}{2m} + U(\mathbf{r}). \quad (3.1)$$

The probability density of finding it at (\mathbf{r}, \mathbf{p}) is

$$P(\mathbf{r}, \mathbf{p}) = \frac{1}{(2\pi\hbar)^3} \frac{e^{-H_0(\mathbf{r}, \mathbf{p})/k_B T}}{Z}, \quad (3.2)$$

where the partition function

$$Z = \frac{1}{(2\pi\hbar)^3} \int d^3r d^3p e^{-H_0(\mathbf{r}, \mathbf{p})/k_B T}. \quad (3.3)$$

For N particles, the density in phase space is

$$n(\mathbf{r}, \mathbf{p}) = N \cdot P(\mathbf{r}, \mathbf{p}). \quad (3.4)$$

Assuming $U(\mathbf{0}) = 0$ as a trap minimum, the highest density will occur at energetically lowest place

$$n(\mathbf{0}, \mathbf{0}) = \frac{1}{(2\pi\hbar)^3} \cdot \underbrace{\frac{N}{Z}}_D. \quad (3.5)$$

$D = N/Z$ is the number of particles per unit cubic Planck constant volume (*degeneracy parameter*). For $D \gtrsim 1$, it will be unavoidable that particle

wavefunctions overlap in phase space and thus quantum effects cannot be neglected. $D \ll 1$ however corresponds to the classical limit.

We can now calculate then density distributions in real space and momentum space.

$$\begin{aligned} n(\mathbf{r}) &= \int n(\mathbf{r}, \mathbf{p}) d^3 p = n(\mathbf{0}, \mathbf{0}) e^{-U(\mathbf{r})/k_B T} \int_0^\infty 4\pi p^2 e^{-\frac{p^2}{2mk_B T}} dp \\ &= n(\mathbf{0}, \mathbf{0}) e^{-U(\mathbf{r})/k_B T} \left(\frac{2\pi\hbar}{\lambda_{dB}} \right)^3, \end{aligned} \quad (3.6)$$

where $\lambda_{dB} = \sqrt{2\pi\hbar^2/mk_B T}$ is the de Broglie wavelength. Insert $\mathbf{r} = 0$, and we get

$$D = n(\mathbf{0}) \lambda_{dB}^3. \quad (3.7)$$

Similarly, the momentum distribution is

$$n(\mathbf{p}) = n(\mathbf{0}, \mathbf{0}) e^{-\mathbf{p}^2/2mk_B T} \int e^{-\frac{U(\mathbf{r})}{k_B T}} d^3 r. \quad (3.8)$$

Examples of the degeneracy parameter

- d -dimensional box potentials within box L^d . As the energy levels are

$$E_{n_1, \dots, n_d} = \frac{\pi^2 \hbar^2}{2mL^2} \sum_{i=1}^d n_i^2, \quad (3.9)$$

the density of states is

$$\rho(\epsilon) \sim \frac{\partial}{\partial \epsilon} \frac{1}{2^d} A_d \left(\sqrt{\frac{2mL^2}{\pi^2 \hbar^2} \epsilon} \right), \quad (3.10)$$

where $A_d(r)$ is the volume of d -dimensional ball or radius r . Thus the phase space density $n(\mathbf{r}, \mathbf{p})$, which is uniform in configuration space, satisfies that

$$n(\mathbf{r}, \mathbf{p}) L^3 d\mathbf{p} = \rho \left(\frac{p^2}{2m} \right) d \left(\frac{p^2}{2m} \right). \quad (3.11)$$

Reorganizing Eq. (3.11) gives $n(\mathbf{r}, \mathbf{p}) = 1/(2\pi\hbar)^d$, and thus $D = 1$.

- Gas of nitrogen molecules at room temperature $T = 300$ K, density 1.2 kg/m^3 . The de Broglie wavelength can be calculated to be ap-

proximately 1.90×10^{-11} m, and hence the degeneracy parameter is $D = n(\mathbf{r})\lambda_{dB} \approx 1.75 \times 10^{-7} \ll 1$.

3.2 Bose-Einstein condensation

The number occupation of Bose gas is

$$N_j = \frac{1}{e^{\beta(\epsilon_j - \mu)} - 1} \quad (3.12)$$

for different energy levels ϵ_j and chemical potential μ . As $\mu \rightarrow \epsilon_0^-$, N_0 will diverge. We can compute the fraction by computing the number of particles in the rest of the system (assume $\epsilon_0 \rightarrow 0^+$):

$$N - N_0 = \sum_{j \geq 1} \frac{1}{e^{\beta(\epsilon_j - \mu)} - 1} \rightarrow \int_{0^+}^{\infty} \frac{\rho(\epsilon)}{e^{\beta(\epsilon - \mu)} - 1} d\epsilon. \quad (3.13)$$

Harmonic oscillator For a d -dimensional isotropic harmonic oscillator, the density of states is

$$\rho^{(d)}(\epsilon) = \frac{\epsilon^{d-1}}{(d-1)!(\hbar\omega)^d}, \quad (3.14)$$

where ω is the frequency for harmonic oscillator. Importantly, $\lim_{\epsilon \rightarrow 0} \rho(\epsilon) = 0$ for $d \geq 3$. We can therefore let the integral start at 0 when we set $\mu \rightarrow \epsilon_0 \rightarrow 0$. In 3D,

$$N - N_0 = \zeta(3) \left(\frac{k_B T}{\hbar\omega} \right)^3. \quad (3.15)$$

For a fixed T , $N_c = \zeta(3) \left(\frac{k_B T}{\hbar\omega} \right)^3$ is the critical atom number and for fixed N ,

$$T_c = \frac{\hbar\omega}{k_B} \left(\frac{N}{\zeta(3)} \right)^{\frac{1}{2}} \quad (3.16)$$

is the critical temperature. When $T < T_c$ or $N > N_c$, any atom added to the system will be in the condensed ground state!

The condensed fraction is (when $T < T_c$)

$$\frac{N_0}{N} = 1 - \frac{(N - N_0)}{N} = 1 - \zeta(3) \frac{1}{N} \left(\frac{k_B T}{\hbar\omega} \right)^3. \quad (3.17)$$

See Fig. 3.2. When cooling the system, the condensed fraction rises quickly towards 1.

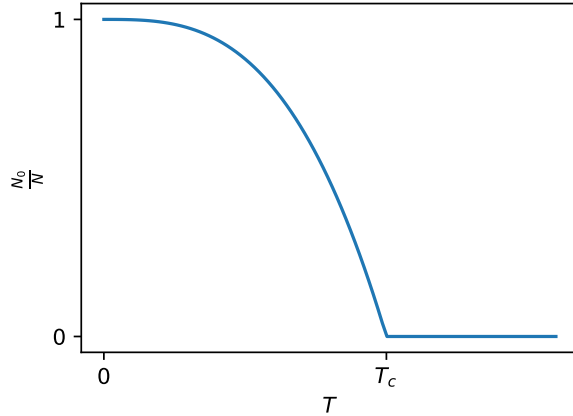


Figure 3.1: Bose-Einstein condensation

Uniform free system For box potential of finite volume L^3 ,

$$\rho(\epsilon) = \frac{L^3}{4\pi^2} \left(\frac{2m}{\hbar^2} \right)^{\frac{3}{2}} \sqrt{\epsilon}. \quad (3.18)$$

As this is proportional to the volume, we can use instead the the densities:

$$n_c = \frac{1}{L^3} \int_0^\infty \frac{\rho(\epsilon)}{e^{\beta\epsilon} - 1} d\epsilon = \frac{1}{4\pi^2} \left(\frac{2mk_B T}{\hbar^2} \right)^{\frac{3}{2}} \zeta\left(\frac{3}{2}\right) \Gamma\left(\frac{3}{2}\right) \approx 2.612 \lambda_{dB}^{-3}. \quad (3.19)$$

The critical density is 2.612 times larger than our criterion for the degenerate gas $n \geq \lambda_{dB}^{-3}$.

3.2.1 Density distribution of cold bosons

Configuration space distribution We can further calculate the density distribution in configuration space:

$$n(\mathbf{r}) = \int d\mathbf{p} \frac{1}{(2\pi\hbar)^3} \cdot \frac{1}{e^{\beta(\epsilon(\mathbf{r}, \mathbf{p}) - \mu)} - 1} = \frac{1}{\lambda_{dB}^3} g_{\frac{3}{2}}(e^{\beta(\mu - V(\mathbf{r}))}). \quad (3.20)$$

Here $g_\alpha(z) = \Gamma(\alpha) \sum_{n=1}^\infty z^n / n^\alpha$ is the Bose-Einstein function. In the high T or large V limit, it converges to the classical case. It is of course the non-condensed case.

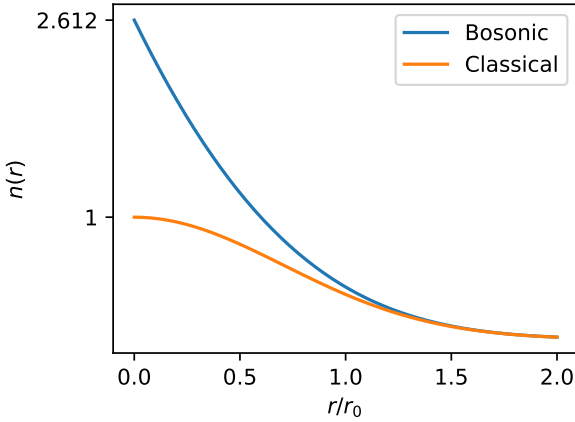


Figure 3.2: Configuration space distribution of cold bosons. $V(r) = |r/r_0|^2/\beta$.

Bose condensate For the atoms in the condensed part, the density distribution is more clear:

$$n_{\text{BEC}}(\mathbf{r}) = n_0 |\Psi(\mathbf{r})|^2. \quad (3.21)$$

Coincidentally, for harmonic oscillator the ground state wave function is also Gaussian, but determined entirely by the trap parameters, independent on the temperature. It will be typically a lot smaller than the thermal gas width for $T \ll T_c$, which you can easily understand by considering that ground state is the only occupied BEC state, whereas many states are occupied in the thermal gas.

Momentum space distribution Analogous calculations can be done to determine the distribution in momentum space. This is in particular more interesting for the uniform free gas, as the spatial density distribution is completely independent of the temperature.

3.2.2 Interference of two bose-einstein condensates

Symmetry breaking in BEC The symmetry broken in thermal-BEC transition is the $U(1)$ gauge symmetry in phase space. The phase can be seen by detecting

- the evaporated atoms in evaporative cooling of a BEC. Their phases of wavefunctions should depend on the phase of BEC and the transition

frequency. The atoms that decay at two different points of the trap will have different phases when propagated to the same point, which forms effectively the interference of two BECs.

- or directly interferences between BECs. We should first discuss the time of flight behavior of non-interacting BEC for better explanation.

Time of flight of ground state BEC Take the (isotropic) harmonic oscillator potential as an example. Before the time of flight (at $t = 0$), the condensate is at ground state of harmonic oscillator

$$\psi(\mathbf{r}, t = 0) = \left(\frac{m\omega}{\pi\hbar} \right)^{3/4} \exp \left(-\frac{m\omega\mathbf{r}^2}{2\hbar} \right), \quad (3.22)$$

where ω is defined by the trap. Its Fourier transform to the momentum space is

$$\begin{aligned} \tilde{\psi}(\mathbf{k}, t = 0) &= \frac{1}{(2\pi)^{3/2}} \int d\mathbf{r} \psi(\mathbf{r}, 0) e^{-i\mathbf{k}\cdot\mathbf{r}} \\ &= \left(\frac{\hbar}{\pi m\omega} \right)^{3/4} \exp \left(-\frac{\hbar\mathbf{r}^2}{2m\omega} \right). \end{aligned} \quad (3.23)$$

The time evolution in momentum space is clear:

$$\tilde{\psi}(\mathbf{k}, t) = \tilde{\psi}(\mathbf{k}, 0) \exp \left(-\frac{i\hbar\mathbf{k}^2}{2m} t \right), \quad (3.24)$$

which can be pulled back to configuration space by inverse Fourier transform:

$$\begin{aligned} \psi(\mathbf{r}, t) &= \frac{1}{(2\pi)^{3/2}} \int d\mathbf{k} \tilde{\psi}(\mathbf{k}, t) e^{i\mathbf{k}\cdot\mathbf{r}} \\ &= \frac{e^{i\delta_t}}{(\pi\sigma_t^2)^{3/4}} \exp \left(-\frac{\mathbf{r}^2(1 - i\omega t)}{2\sigma_t^2} \right). \end{aligned} \quad (3.25)$$

The width of BEC wavefunction is expanded to

$$\sigma_t^2 = \frac{\hbar}{m\omega} (1 + \omega^2 t^2) \quad (3.26)$$

and an additional phase is given by $\tan \delta_t = -3\omega t/2$.

Now consider two BECs (of same type of identical bosons) of initial distance d . Their total wavefunction of two is

$$\Psi(\mathbf{r}, t) = \sqrt{N_1} e^{i\phi_1} \psi(\mathbf{r} - \mathbf{d}/2, t) + \sqrt{N_2} e^{i\phi_2} \psi_2(\mathbf{r} + \mathbf{d}/2, t), \quad (3.27)$$

which leads to an interference term in the total particle density $n(\mathbf{r}, t) = |\Psi(\mathbf{r}, t)|^2 = N_1|\psi(\mathbf{r} - \mathbf{r}/2, t)|^2 + N_2|\psi(\mathbf{r} + \mathbf{r}/2, t)|^2 + n_{\text{int}}$:

$$\begin{aligned} n_{\text{int}} &= 2\sqrt{N_1 N_2} \Re[e^{i(\phi_1 - \phi_2)} \psi(\mathbf{r} - \mathbf{d}/2, t) \psi^*(\mathbf{r} + \mathbf{d}/2, t)] \\ &= 2\sqrt{N_1 N_2} \frac{1}{(\pi \sigma_t^2)^{3/2}} e^{-(\mathbf{r}^2 + \mathbf{d}^2/4)/\sigma_t^2} \cos\left(\frac{\omega t \mathbf{d}}{\sigma_t^2} \cdot \mathbf{r} + \phi_1 - \phi_2\right). \end{aligned} \quad (3.28)$$

The cosine part oscillates much faster than the exponential decay, given that $\omega t \gg 1$, which also means that the BEC has been expanded to much larger than the original situation, $\sigma_t \gg \sigma_0$. Therefore the interference patterns are distanced by

$$\Delta r = \frac{2\pi\sigma_t^2}{\omega t d}. \quad (3.29)$$

As $\sigma_t^2 \approx \frac{\hbar\omega}{m} t^2$,

$$\Delta r \approx \frac{2\pi\hbar t}{md}. \quad (3.30)$$

Such interference patterns have been observed in experiments (Andrews, 1997), see Fig. 3.3.

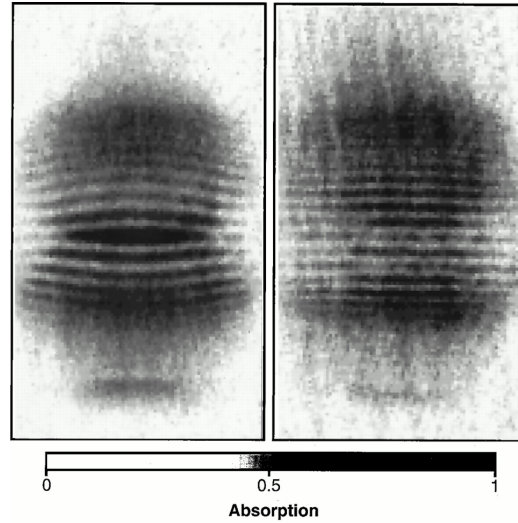


Figure 3.3: Interference of two BEC condensates from (Andrews, 1997).

3.3 Journal Club 3: BEC in sodium gas (Davis et al., 1995a)

- *What is the selling point of this paper?*

They solved the problem of majorana loss in their last paper (Davis et al., 1995b) in Journal Club 2 by "plugging in the hole" so that lower temperature ($2\mu\text{K}$) and higher particle density (exceeding 10^{14}cm^{-3}) are achieved. They also find a way to rapidly switch off the light for better imaging. BEC of sodium gas is observed.

- *How do they plug in the hole?*

They use a far-off-resonant beam with high intensity as a repulsive force to avoid atoms from moving to the centre. The large detuning is such that the heating to each atom is minimized, which a high intensity has to be applied to compensate the scattering rate.

- *How do they determine that the atoms are really in BEC phase?*

When the temperature is above BEC transition, kinetic energy dominates and thus after switching off the trap, the velocity distribution is isotropic and the shape of ToF image is round. In the BEC case, however, interaction contributes significantly and the kinetic energy can be neglected. The density distribution will be a mirror of the potential in the weak interacting case (see discussion in the next chapter).

Also in the transition regime, a single Gaussian is not enough to fit the ToF image. Instead, two of them, one for the condensate and one for the thermal atoms are needed.

PHYSICAL REVIEW LETTERS

VOLUME 75

27 NOVEMBER 1995

NUMBER 22

Bose-Einstein Condensation in a Gas of Sodium Atoms

K. B. Davis, M.-O. Mewes, M. R. Andrews, N. J. van Druten, D. S. Durfee, D. M. Kurn, and W. Ketterle

*Department of Physics and Research Laboratory of Electronics, Massachusetts Institute of Technology,
Cambridge, Massachusetts 02139*
(Received 17 October 1995)

We have observed Bose-Einstein condensation of sodium atoms. The atoms were trapped in a novel trap that employed both magnetic and optical forces. Evaporative cooling increased the phase-space density by 6 orders of magnitude within seven seconds. Condensates contained up to 5×10^5 atoms at densities exceeding 10^{14} cm^{-3} . The striking signature of Bose condensation was the sudden appearance of a bimodal velocity distribution below the critical temperature of $\sim 2 \mu\text{K}$. The distribution consisted of an isotropic thermal distribution and an elliptical core attributed to the expansion of a dense condensate.

PACS numbers: 03.75.Fi, 05.30.Jp, 32.80.Pj, 64.60.-i

Bose-Einstein condensation (BEC) is a ubiquitous phenomenon which plays significant roles in condensed matter, atomic, nuclear, and elementary particle physics, as well as in astrophysics [1]. Its most striking feature is a macroscopic population of the ground state of the system at finite temperature [2]. The study of BEC in weakly interacting systems holds the promise of revealing new macroscopic quantum phenomena that can be understood from first principles, and may also advance our understanding of superconductivity and superfluidity in more complex systems.

During the past decade, work towards BEC in weakly interacting systems has been carried forward with excitons in semiconductors and cold trapped atoms. BEC has been observed in excitonic systems, but a complete theoretical treatment is lacking [1,3]. The pioneering work towards BEC in atomic gases was performed with spin-polarized atomic hydrogen [4,5]. Following the development of evaporative cooling [6], the transition was approached within a factor of 3 in temperature [7]. Laser cooling provides an alternative approach towards very low temperatures, but has so far been limited to phase-space densities typically 10^5 times lower than required for BEC. The combination of laser cooling with evaporative cooling [8–10] was the prerequisite for obtaining BEC in alkali atoms. This year, within a few months, three independent and different approaches succeeded in creating BEC in

rubidium [11], lithium [12], and, as reported in this paper, in sodium. Our results are distinguished by a production rate of Bose-condensed atoms which is 3 orders of magnitude larger than in the two previous experiments. Furthermore, we report a novel atom trap that offers a superior combination of tight confinement and capture volume and the attainment of unprecedented densities of cold atomic gases.

Evaporative cooling requires an atom trap which is tightly confining and stable. So far, magnetic traps and optical dipole traps have been used. Optical dipole traps provide tight confinement, but have only a very small trapping volume (10^{-8} cm^3). The tightest confinement in a magnetic trap is achieved with a spherical quadrupole potential (linear confinement); however, atoms are lost from this trap due to nonadiabatic spin flips as the atoms pass near the center, where the field rapidly changes direction. This region constitutes a “hole” in the trap of micrometer dimension. The recently demonstrated “TOP” trap suppresses this trap loss, but at the cost of lower confinement [8].

We suppressed the trap loss by adding a repulsive potential around the zero of the magnetic field, literally “plugging” the hole. This was accomplished by tightly focusing an intense blue-detuned laser that generated a repulsive optical dipole force. The optical plug was created by an Ar^+ -laser beam (514 nm) of 3.5 W focused

to a beam waist of $30 \mu\text{m}$. This caused 7 MHz ($350 \mu\text{K}$) of light shift potential at the origin. Heating due to photon scattering was suppressed by using far-off-resonant light, and by the fact that the atoms are repelled from the region where the laser intensity is highest.

The experimental setup was similar to that described in our previous work [9]. Typically, within 2 s 10^9 atoms in the $F = 1, m_F = -1$ state were loaded into a magnetic trap with a field gradient of 130 G/cm ; the peak density was $\sim 10^{11} \text{ cm}^{-3}$, the temperature $\sim 200 \mu\text{K}$, and the phase-space density 10^6 times lower than required for BEC. The lifetime of the trapped atoms was $\sim 30 \text{ s}$, probably limited by background gas scattering at a pressure of $\sim 1 \times 10^{-11} \text{ mbar}$.

The magnetically trapped atoms were further cooled by rf-induced evaporation [8,9,13]. rf-induced spin flips were used to selectively remove the higher-energy atoms from the trap resulting in a decrease in temperature for the remaining atoms. The total (dressed-atom) potential is a combination of the magnetic quadrupole trapping potential, the repulsive potential of the plug, and the effective energy shifts due to the rf. At the point where atoms are in resonance with the rf, the trapped state undergoes an avoided crossing with the untrapped states (corresponding to a spin flip), and the trapping potential bends over. As a result, the height of the potential barrier varies linearly with the rf frequency. The total potential is depicted in Fig. 1. Over 7 s , the rf frequency was swept from 30 MHz to the final value around 1 MHz , while the field gradient was first increased to 550 G/cm (to enhance the initial elastic-collision rate) and then lowered to 180 G/cm (to avoid the losses due to inelastic processes at the final high densities).

Temperature and total number of atoms were determined using absorption imaging. The atom cloud was imaged either while it was trapped or following a sudden switch-off of the trap and a delay time of 6 ms . Such time-of-flight images displayed the velocity distribution of the trapped cloud. For probing, the atoms

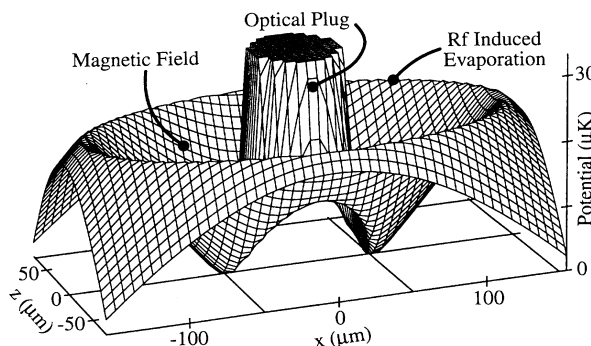


FIG. 1. Adiabatic potential due to the magnetic quadrupole field, the optical plug, and the rf. This cut of the three-dimensional potential is orthogonal to the propagation direction (y) of the blue-detuned laser. The symmetry axis of the quadrupole field is the z axis.

were first pumped to the $F = 2$ state by switching on a 10 mW/cm^2 laser beam in resonance with the $F = 1 \rightarrow F = 2$ transition. $10 \mu\text{s}$ later the atoms were concurrently exposed to a $100 \mu\text{s}$, 0.25 mW/cm^2 probe laser pulse in resonance with the $F = 2 \rightarrow F = 3$ transition, propagating along the trap's y direction. This probe laser beam was imaged onto a charge-coupled device sensor with a lens system having a resolution of $8 \mu\text{m}$. Up to 100 photons per atom were absorbed without blurring the image due to heating.

At temperatures above $15 \mu\text{K}$ the observed trapped clouds were elliptical with an aspect ratio of $2:1$ due to the symmetry of the quadrupole field. At the position of the optical plug they had a hole, which was used for fine alignment. A misalignment of the optical plug by $\sim 20 \mu\text{m}$ resulted in increased trap loss and prevented us from cooling below $50 \mu\text{K}$. This is evidence that the Majorana spin flips are localized in a very small region around the center of the trap. At temperatures below $15 \mu\text{K}$, the cloud separated into two pockets at the two minima in the potential of Fig. 1. The bottom of the potential can be approximated as a three-dimensional anisotropic harmonic oscillator potential with frequencies $\omega_y^2 = \mu B'/(2mx_0)$, $\omega_z^2 = 3\omega_y^2$, $\omega_x^2 = \omega_y^2[(4x_0^2/w_0^2) - 1]$, where μ is the atom's magnetic moment, m the mass, B' the axial field gradient, w_0 the Gaussian beam waist parameter ($1/e^2$ radius) of the optical plug, and x_0 the distance of the potential minimum from the trap center. x_0 was directly measured to be $50 \mu\text{m}$ by imaging the trapped cloud, w_0 ($30 \mu\text{m}$) was determined from x_0 , the laser power (3.5 W), and B' (180 G/cm). With these values the oscillation frequencies are 235 , 410 , and 745 Hz in the y , z , and x directions, respectively.

When the final rf frequency ν_{rf} was lowered below 0.7 MHz , a distinctive change in the symmetry of the velocity distribution was observed [Figs. 2(a) and 2(b)]. Above this frequency the distribution was perfectly spherical as expected for a thermal uncondensed cloud [14]. Below the critical frequency, the velocity distribution contained an elliptical core which increased in intensity when

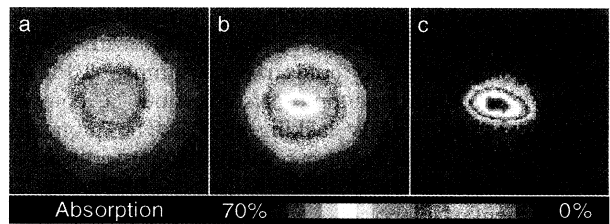


FIG. 2 (color). Two-dimensional probe absorption images, after 6 ms time of flight, showing evidence for BEC. (a) is the velocity distribution of a cloud cooled to just above the transition point, (b) just after the condensate appeared, and (c) after further evaporative cooling has left an almost pure condensate. (b) shows the difference between the isotropic thermal distribution and an elliptical core attributed to the expansion of a dense condensate. The width of the images is $870 \mu\text{m}$. Gravitational acceleration during the probe delay displaces the cloud by only 0.2 mm along the z axis.

the rf was further swept down, whereas the spherical cloud became less intense. We interpret the elliptical cloud as due to the Bose condensate, and the spherical cloud as due to the normal fraction.

In the region just below the transition frequency one expects a bimodal velocity distribution: a broad distribution due to the normal gas and a narrow distribution due to the condensate. The cross sections of the time-of-flight images (Fig. 3) indeed show such bimodal distributions in this region. Figure 4 shows how suddenly the time-of-flight image changes below $\nu_{rf} = 0.7$ MHz. The effective area of the observed cloud becomes very small [Fig. 4(a)], while the velocity distribution is no longer Gaussian [Fig. 4(b)] and requires different widths for the condensate and the normal fraction [Fig. 4(c)].

At the critical frequency, a temperature of (2.0 ± 0.5) μK was derived from the time-of-flight image. An independent, though less accurate estimate of the temperature T is obtained from the dynamics of evaporative cooling. Efficient evaporation leads to a temperature which is about 10 times smaller than the depth of the trapping potential [15]. Since the speed of evaporation depends exponentially on the ratio of potential depth to temperature, we expect this estimate of $T = 2 \mu\text{K}$ to be accurate to within a factor of 2.

The critical number of atoms N_c to achieve BEC is determined by the condition that the number of atoms per

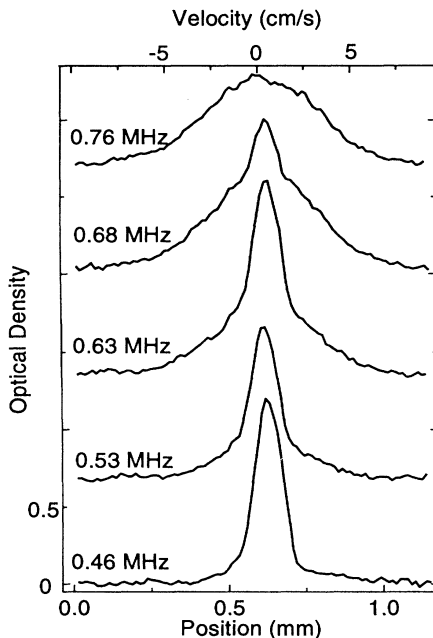


FIG. 3. Optical density as a function of position along the z axis for progressively lower values of the final rf frequency. These are vertical cuts through time-of-flight images like those in Fig. 2. For $\nu_{rf} < 0.7$ MHz, they show the bimodal velocity distributions characteristic of the coexistence of a condensed and uncondensed fraction. The top four plots have been offset vertically for clarity.

cubic thermal de Broglie wavelength exceeds 2.612 at the bottom of the potential [2]. For a harmonic oscillator potential this is equivalent to $N_c = 1.202(k_B T)^3 / \hbar^3 \omega_x \omega_y \omega_z$ [16]. For our trap and $2.0 \mu\text{K}$, $N_c = 2 \times (1.2 \times 10^6)$, where the factor of 2 accounts for the two separated clouds. The predicted value for N_c depends on the sixth power of the width of a time-of-flight image and is only accurate to within a factor of 3. We determined the number of atoms by integrating over the absorption image. At the transition point, the measured number of 7×10^5 agrees with the prediction for N_c . The critical peak density n_c at $2.0 \mu\text{K}$ is $1.5 \times 10^{14} \text{ cm}^{-3}$. Such a high density appears to be out of reach for laser cooling, and demonstrates that evaporative cooling is a powerful technique to obtain not only ultralow temperatures, but also extremely high densities.

An ideal Bose condensate shows a macroscopic population of the ground state of the trapping potential. This picture is modified for a weakly interacting Bose gas. The mean-field interaction energy is given by $n\tilde{U}$, where n is the density and \tilde{U} is proportional to the scattering length a : $\tilde{U} = 4\pi\hbar^2 a/m$ [2]. Using our recent experimental result $a = 4.9 \text{ nm}$ [9], $\tilde{U}/k_B = 1.3 \times 10^{-21} \text{ K cm}^3$. At the transition point, $n_c \tilde{U}/k_B T_c = 0.10$. Consequently, above the transition point, the kinetic energy dominates over the interaction energy, and the velocity

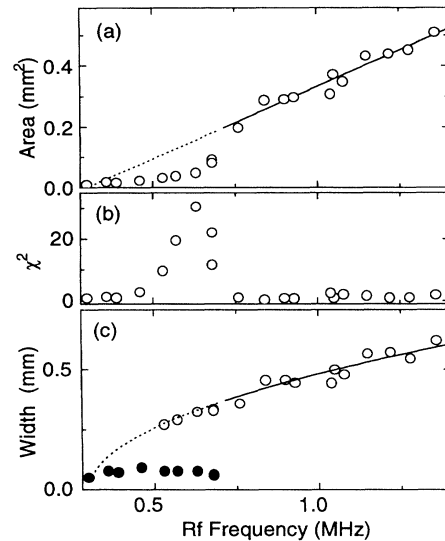


FIG. 4. Further evidence for a phase transition is provided by the sudden change of observed quantities as the final rf frequency ν_{rf} is varied. (a) Area of the cloud in the time-of-flight image versus ν_{rf} . The area was obtained as the ratio of the integrated optical density and the peak optical density. The area changes suddenly at $\nu_{rf} = 0.7$ MHz. Below the same frequency, the velocity distributions (Fig. 3) cannot be represented by a single Gaussian, as demonstrated by the χ^2 for a single Gaussian fit (b), and required different widths for the condensate (full circles) and noncondensate fraction (c). In (a) and (c) the lines reflect the behavior of a classical gas with a temperature proportional to the trap depth.

distribution after sudden switch-off of the trap is isotropic. For the condensate, however, the situation is reversed. As we will confirm below, the kinetic energy of the condensate is negligible compared to its interaction energy [17]. Furthermore, well below the transition point, the interaction with the noncondensate fraction can be neglected. In such a situation, the solution of the nonlinear Schrödinger equation reveals that the condensate density $n_0(\mathbf{r})$ is a mirror image of the trapping potential $V(\mathbf{r})$: $n_0(\mathbf{r}) = n_0(\mathbf{0}) - V(\mathbf{r})/\tilde{U}$, as long as this expression is positive, otherwise $n_0(\mathbf{r})$ vanishes (see, e.g., Refs. [5,18]). For a harmonic potential, one obtains the peak density $n_0(\mathbf{0})$ for N_0 atoms in the condensate $n_0(\mathbf{0}) = 0.118(N_0 m^3 \omega_x \omega_y \omega_z / \hbar^3 a^{3/2})^{2/5}$.

Typically, we could cool one-fourth of the atoms at the transition point into a pure condensate. For an observed $N_0 = 1.5 \times 10^5$, we expect the condensate to be 2 times more dense than the thermal cloud at the transition point, and about 6 times larger than the ground-state wave function. The kinetic energy within the condensate is $\sim \hbar^2/(2mR^2)$, where R is the size of the condensate [18], while the internal energy is $2n_0\tilde{U}/7$. Thus the kinetic energy of the condensed atoms is around 1 nK, much less than the zero-point energy of our trap (35 nK) and the calculated internal energy of 120 nK. This estimate is consistent with our initial assumption that the kinetic energy can be neglected compared to the interaction energy.

The internal energy is ~ 25 times smaller than the thermal energy $(3/2)k_B T_c$ at T_c . Consequently, the width of the time-of-flight image of the condensate is expected to be about 5 times smaller than at the transition point. This is close to the observed reduction in the width shown in Fig. 4(c). This agreement might be fortuitous because we have so far neglected the anisotropy of the expansion, but it indicates that we have observed the correct magnitude of changes which are predicted to occur at the BEC transition of a weakly interacting gas. In several cooling cycles, as many as 5×10^5 condensed atoms were observed; we estimate the number density in these condensates to be $4 \times 10^{14} \text{ cm}^{-3}$.

A striking feature of the condensate is the nonisotropic velocity distribution [11,19]. This is caused by the “explosion” of the condensate due to repulsive forces which are proportional to the density gradient. The initial acceleration is therefore inversely proportional to the width of the condensate resulting in an aspect ratio of the velocity distribution, which is inverted compared to the spatial distribution. When we misaligned the optical plug vertically, the shape of the cloud changed from two vertical crescents to a single elongated horizontal crescent. The aspect ratio of the time-of-flight image of the condensate correspondingly changed from horizontal to vertical elongation. In contrast, just above the transition point, the velocity distribution was found to be spherical and insensitive to the alignment of the plug. However, we cannot account quanti-

tatively for the observed distributions because we have two separated condensates which overlap in the time-of-flight images, and also because of some residual horizontal acceleration due to the switch-off of the trap, which is negligible for the thermal cloud, but not for the condensate [20].

The lifetime of the condensate was about 1 s. This lifetime is probably determined either by three-body recombination [21] or by the heating rate of 300 nK/s, which was observed for a thermal cloud just above T_c . This heating rate is much higher than the estimated 8 nK/s for the off-resonant scattering of green light and may be due to residual beam jitter of the optical plug.

In conclusion, we were able to Bose-condense 5×10^5 sodium atoms within a total loading and cooling cycle of 9 s. During evaporative cooling, the elastic collision rate increased from 30 Hz to 2 kHz resulting in a mean free path comparable to the dimensions of the sample. Such collisionally dense samples are the prerequisite for studying various transport processes in dense ultracold matter. Furthermore, we have reached densities in excess of 10^{14} cm^{-3} , which opens up new possibilities for studying decay processes like dipolar relaxation and three-body recombination, and for studying a weakly interacting Bose gas over a broad range of densities and therefore strengths of interaction.

We are grateful to E. Huang and C. Sestok for important experimental contributions, to M. Raizen for the loan of a beam pointing stabilizer, and to D. Kleppner for helpful discussions. We are particularly grateful to D. E. Pritchard, who not only contributed many seminal ideas to the field of cold atoms, but provided major inspiration and equipment to W. K. This work was supported by ONR, NSF, JSEP, and the Sloan Foundation. M.-O. M., K. B. D., and D. M. K. would like to acknowledge support from Studienstiftung des Deutschen Volkes, MIT Physics Department Lester Wolfe fellowship, and NSF Graduate Research Fellowship, respectively, and N. J. v. D. from “Nederlandse Organisatie voor Wetenschappelijk Onderzoek (NWO)” and NACEE (Fulbright fellowship).

-
- [1] A. Griffin, D. W. Snoke, and S. Stringari, *Bose-Einstein Condensation* (Cambridge University Press, Cambridge, 1995).
 - [2] K. Huang, *Statistical Mechanics* (Wiley, New York, 1987), 2nd ed.
 - [3] J. L. Lin and J. P. Wolfe, Phys. Rev. Lett. **71**, 1222 (1993).
 - [4] I. F. Silvera and M. Reynolds, J. Low Temp. Phys. **87**, 343 (1992); J. T. M. Walraven and T. W. Hijmans, Physica (Amsterdam) **197B**, 417 (1994).
 - [5] T. Greystak, in Ref. [1], p. 131.
 - [6] N. Masuhara *et al.*, Phys. Rev. Lett. **61**, 935 (1988).
 - [7] J. Doyle *et al.*, Phys. Rev. Lett. **67**, 603 (1991).
 - [8] W. Petrich, M. H. Anderson, J. R. Ensher, and E. A. Cornell, Phys. Rev. Lett. **74**, 3352 (1995).

- [9] K. B. Davis *et al.*, Phys. Rev. Lett. **74**, 5202 (1995).
- [10] C. S. Adams *et al.*, Phys. Rev. Lett. **74**, 3577 (1995).
- [11] M. H. Anderson *et al.*, Science **269**, 198 (1995).
- [12] C. C. Bradley, C. A. Sackett, J. J. Tollett, and R. G. Hulet, Phys. Rev. Lett. **75**, 1687 (1995).
- [13] D. E. Pritchard, K. Helmerson, and A. G. Martin, in *Atomic Physics II*, edited by S. Haroche, J. C. Gay, and G. Grynberg (World Scientific, Singapore, 1989), p. 179.
- [14] The measured $1/e$ decay time for the magnet current is 100 μ s, shorter than the ω^{-1} of the fastest oscillation in the trap (210 μ s). We therefore regard the switch-off as sudden. Any adiabatic cooling of the cloud during the switch-off would result in a nonspherical velocity distribution due to the anisotropy of the potential.
- [15] K. B. Davis, M.-O. Mewes, and W. Ketterle, Appl. Phys. B **60**, 155 (1995).
- [16] V. Bagnato, D. E. Pritchard, and D. Kleppner, Phys. Rev. A **35**, 4354 (1987). This formula is derived assuming $k_B T_c \gg \hbar \omega_{x,y,z}$, which is the case in our experiment.
- [17] Note that already for about 200 atoms in the ground state, the interaction energy in the center of the condensate equals the zero-point energy.
- [18] G. Baym and C. Pethick (to be published).
- [19] M. Holland and J. Cooper (to be published).
- [20] These effects do not affect the vertical velocity distributions shown in Fig. 3.
- [21] A. J. Moerdijk, H. M. J. M. Boesten, and B. J. Verhaar, Phys. Rev. A (to be published).

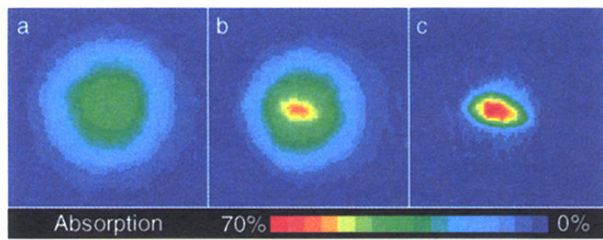


FIG. 2 (color). Two-dimensional probe absorption images, after 6 ms time of flight, showing evidence for BEC. (a) is the velocity distribution of a cloud cooled to just above the transition point, (b) just after the condensate appeared, and (c) after further evaporative cooling has left an almost pure condensate. (b) shows the difference between the isotropic thermal distribution and an elliptical core attributed to the expansion of a dense condensate. The width of the images is 870 μm . Gravitational acceleration during the probe delay displaces the cloud by only 0.2 mm along the z axis.

3.4 Journal Club 4: s and d wave scattering interference (Thomas et al., 2004)

- *What is the selling point of this paper?*

They take direct imaging of s and d wave interference in cold collisions of rubidium atoms.

- *How is this done?*

They prepare two clouds of atoms in a magnetic double-well potential with evaporative cooling such that the temperature is right above BEC transition. Then the trapping potential is continuously modified to a single-well configuration and atomic clouds are accelerated to collide at the center of the harmonic potential. The direction and speed of the collision can thus be well controlled.

- *What don't they use BECs?*

There will interferences between BECs so that the collision interference cannot be distinguished. Higher temperatures will however lead to more types of collision (of higher orbitals) and in all directions.

- *Why can't the particle density be large?*

It would be probable that a particle is scattered more than once. Moreover, when there are more dense, there could be scattering processes of more than two particles.

- *What leads to the shapes of the images?*

It is 2D projection of an elliptical 3D distribution, and an inverse Abel transform is required. The shapes of the halo of scattered atoms should correspond to the scattering amplitude $f(\theta)$ in Eq. (1), if we put them in polar plots.

Imaging of *s* and *d* Partial-Wave Interference in Quantum Scattering of Identical Bosonic Atoms

Nicholas R. Thomas,¹ Niels Kjærgaard,^{1,*} Paul S. Julienne,² and Andrew C. Wilson¹

¹Department of Physics, University of Otago, Dunedin, New Zealand

²National Institute of Standards and Technology, 100 Bureau Drive, Stop 8423, Gaithersburg, Maryland, 20899-8423 USA

(Received 19 May 2004; published 22 October 2004)

We report on the direct imaging of *s* and *d* partial-wave interference in cold collisions of atoms. Two ultracold clouds of ⁸⁷Rb atoms were accelerated by magnetic fields to collide at energies near a *d*-wave shape resonance. The resulting halos of scattered particles were imaged using laser absorption. By scanning across the resonance we observed a marked evolution of the scattering patterns due to the energy dependent phase shifts for the interfering *s* and *d* waves. Since only two partial-wave states are involved in the collision process the scattering yield and angular distributions have a simple interpretation in terms of a theoretical model.

DOI: 10.1103/PhysRevLett.93.173201

PACS numbers: 34.50.-s, 03.65.Nk, 32.80.Pj, 39.25.+k

Atomic collisions are a classic topic of quantum mechanics [1,2]. With the advent of laser cooling [3], confining and cooling various atomic species to submillikelvin temperatures became possible and gave rise to a wealth of experiments in which quantum effects in collisions at very low energies—cold collisions—were observed [4]. Knowledge about cold collisions paved the way for exciting new developments in experimental atomic physics. Collisions played a crucial role in the achievement of Bose-Einstein condensation [5] and Fermi degeneracy [6] in dilute atomic vapors by mediating thermalization during evaporative cooling and accounting for stability [7]. For atoms at temperatures associated with the quantum degenerate regime the essential interaction properties are determined by a single atomic parameter, the scattering length, because all elastic scattering has an isotropic (*s*-wave) nature at such low energies. The scattering length may exhibit a pronounced dependency on external magnetic fields giving rise to so-called Feshbach resonances [8] which have recently been exploited to create ultracold molecules [9] and molecular Bose-Einstein condensates (BECs) [10].

To date, most experiments on cold collisions of atoms have been carried out using magneto-optical traps (MOTs) or magnetic traps which suffer from the disadvantages that no collision axis is singled out or the collision energy cannot be varied over a wide range [4,11]. If no fixed collision axis is present, anisotropic scattering, as occurs for collision energies above the *s*-wave regime, will be obscured by spatial averaging. One solution to this problem was provided in the “juggling” MOT experiment [12], where a cloud of cesium atoms was laser cooled to 3 μK and ejected vertically from a trap to collide with a previously launched cloud at energies up to 160 μK. Scattered atoms were detected using a spectroscopic technique revealing interference between *s* and *p* partial waves. In experiments on BECs, a collision axis was also

selected using Bragg scattering to accelerate part of the atomic cloud, and pure *s*-wave scattering halos were directly imaged [13].

In this Letter, we report experiments on the collision of two bosonic atomic clouds, initially confined in a magnetic double-well potential and evaporatively cooled to a temperature just above the phase transition for Bose-Einstein condensation. Collisions at a selectable energy occur when the trapping potential is continuously modified to a single-well configuration. The atomic clouds accelerate from the sides of the harmonic potential and collide at the center of the well. The resulting scattering is equivalent to cold collisions of counterpropagating ultracold pulsed atomic beams. Angular resolved detection of scattered atoms is obtained using laser absorption imaging. Specifically, we consider atomic clouds of doubly spin-polarized ⁸⁷Rb which are cooled to a temperature of ∼225 nK and accelerated to collide with energies in the range from 87 to 553 μK as measured in units of Boltzmann’s constant k_B . In this energy interval a *d*-wave shape resonance is known to occur [14]. We observe scattering patterns evolving from *s*-wave-like to *d*-wave-like distributions via intermediate *s* + *d* interfering scattering states which expose the quantum mechanical origin of the process.

Quantum scattering of two particles under our conditions is conveniently described in the partial-wave formalism. The wave function for the relative motion is written $\psi = e^{ikz} + f(\theta)e^{ikr}/r$, where k is the magnitude of the relative wave vector of the colliding particles. The first term of this sum represents an incoming plane wave traveling along the z axis, while the second term represents a radially outgoing scattered wave with an amplitude which depends on the angle θ to the z axis, (see, e.g., [15]). Using a partial-wave expansion of ψ , the scattering amplitude for identical bosons is expressed as $f(\theta) = \sum_{l \text{ even}} (2l+1)(e^{2i\eta_l} - 1)P_l(\cos\theta)/ik$, where P_l is the

Legendre polynomial of order l and η_l are the partial-wave phase shifts. The l th term in the expansion represents particles having orbital angular momentum $l\hbar$ and the sum only runs over even l , since odd partial waves are forbidden by the requirement of a totally symmetric wave function for identical bosonic particles. In the present case, where only $l = \{0, 2\}$ terms (s and d waves) contribute [16], the scattering amplitude is

$$f(\theta) = [\underbrace{(e^{2i\eta_0} - 1)}_{s} + \underbrace{5(e^{2i\eta_2} - 1)(3\cos^2\theta - 1)/2}_{d}]/ik, \quad (1)$$

and the differential cross section $d\sigma/d\Omega = |f(\theta)|^2$ has an angular pattern which depends crucially on the quantum mechanical interference between the partial-wave states as dictated by the phase shifts. Assuming the collisions to occur in free space, scattered particles observed in the center of mass frame will be distributed over a ballistically expanding sphere (the so-called Newton sphere) according to the differential cross section. If the scattered particles are detected using absorption imaging, the distribution on this sphere will be projected onto a plane by the Abel transformation [17]. Figure 1 illustrates this in the case of pure d -wave scattering and imaging along a direction perpendicular to the collision axis.

In our experiment, ^{87}Rb atoms collected in a MOT were optically pumped into the $|F = 2, m_F = 2\rangle$ hyperfine substate and loaded into a Ioffe-Pritchard magnetic trap in the quadrupole-Ioffe configuration [18]. The trapping potential is cylindrically symmetric and harmonic, characterized by radial and axial oscillation frequencies of $\omega_r/2\pi = 275$ and $\omega_z/2\pi = 16$ Hz, respectively. After rf evaporative cooling to a temperature of $12 \mu\text{K}$, the trap was adiabatically transformed to a double-well configuration

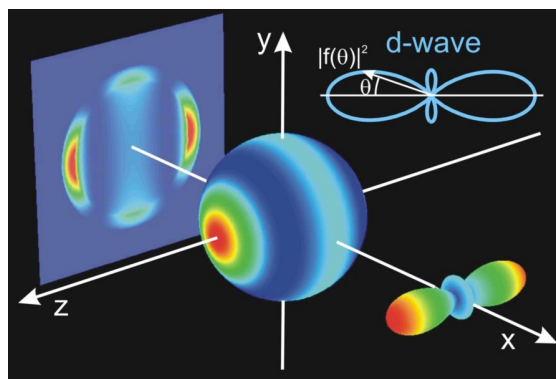


FIG. 1 (color online). Illustration of the process of using absorption imaging for the detection of scattered particles. We present the case of pure d -wave scattering occurring at the origin for particles coming in along the z axis. Scattered particles will be situated on an expanding sphere and distributed according to the d -wave angular emission pattern $|f(\theta)|^2$. Absorption imaging along the x axis projects this distribution onto the yz plane.

ration [19], splitting the atomic cloud in half along its long dimension (z) by raising a potential barrier. The z axis is horizontal so that the influence from gravity is unimportant. An additional rotating bias field of 0.5 mT is applied just before forming the double well to avoid Majorana spin-flip atom loss at the two trap minima, where the magnetic field would otherwise become zero. When fully separated the two clouds were 4.3 mm apart and the trap frequencies were $\omega_r/2\pi = 60 \text{ Hz}$ and $\omega_z/2\pi = 14 \text{ Hz}$ near the well minima. Further evaporative cooling lowered the temperature to 225 nK in each well (as compared to the BEC transition temperature of 100 nK), and the total number of remaining atoms was 4×10^5 . There is a slight difference between the properties of the two clouds due to a small residual tilt in the potential. Subsequently the separation of the clouds was adiabatically adjusted to select the potential energy gained when the trap is rapidly converted back to a single well. To increase the cloud densities the rotating bias field was reduced to 0.2 mT . The collision is initiated by rapidly ramping from a double- to a single-well configuration, accelerating the clouds towards the potential minimum positioned between them. The trapping configuration for the collision has frequencies $\omega_r/2\pi = 155 \text{ Hz}$ and $\omega_z/2\pi = 12 \text{ Hz}$ and remains unchanged until the end of the experiment. After the collision we waited for one-quarter of the radial trap period, so that atoms were at maximum radial extension, before acquiring an absorption image using a $40 \mu\text{s}$ pulse of resonant light and a charge coupled device camera. The 3D distribution of scattered atoms is projected onto a plane giving the column density distribution. We obtained the collision energy and the corresponding uncertainty from a fit to cloud positions measured before and after the collision. The collision energy, expressed in temperature units, is $T = \mu v^2/2k_B$, where μ is the reduced mass of the particles and v is the relative velocity of the two clouds.

Figure 2 shows absorption images of scattering acquired at collision energies in the range from 87 to $348 \mu\text{K}$. Scattering halos of particles with an elliptical envelope are clearly visible as are the outgoing clouds of unscattered atoms. The major and minor semiaxes of the former, and the distance between the latter, increase linearly with \sqrt{T} due to the fixed time of acquisition after collision. The total number of scattered particles N_{sc} was determined by integrating the column density over the image frame and using a suitable interpolation to bridge the areas hidden by the outgoing clouds of unscattered atoms.

The observed scattering yield is interpreted in terms of a coupled-channels theoretical model that includes the ground state singlet and triplet potentials and all spin-dependent interactions. The triplet potential has a van der Waals C_6 constant of 4707 a.u. ($1 \text{ a.u.} = 9.5734 \times 10^{-26} \text{ J nm}^6$) and a scattering length of 98.96 a.u. ($1 \text{ a.u.} = 0.052918 \text{ nm}$) [20]. Figure 3(a) presents the

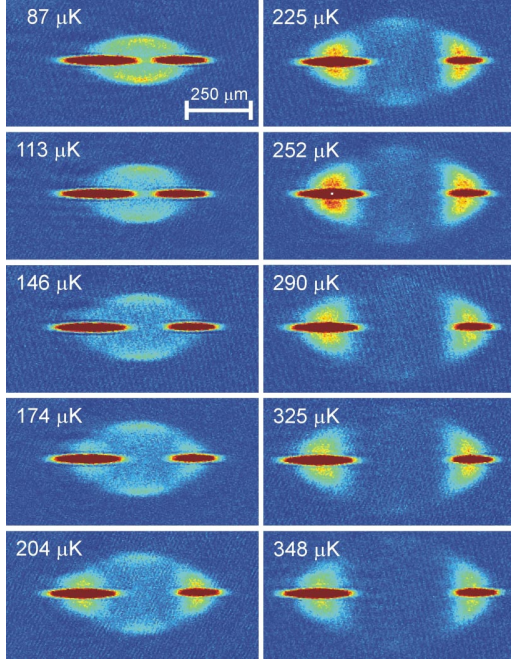


FIG. 2 (color online). Absorption images acquired at a quarter of a radial trap period after the collision of two doubly spin-polarized Rb clouds (visible as dark ellipses) for various collision energies. The halos of scattered particles have elliptical envelopes since they are evolving in an anisotropic harmonic trap which is weakest in the horizontal direction (z direction). At the selected time of acquisition the scattering halos have the maximum radial excursion in the trap.

partial-wave phase shifts for the $l = 0$ and 2 channels with total projection quantum number $m_F = 4$ when two $|F = 2, m_F = 2\rangle$ atoms collide in a total magnetic field of 0.22 mT, the bias field of this experiment (there is negligible difference at zero field). Using Eq. (1) these phase shifts give the s -wave, d -wave, and total cross sections shown in Fig. 3(b). In Fig. 3(c) we present the fraction of scattered atoms N_{sc}/N_{tot} versus the collision energy as measured in our experiments. Since N_{sc}/N_{tot} is on the order of 40% close to the resonance (i.e., large depletion), the number of scattered particles is not proportional to the total elastic cross section $\sigma(T)$. As a result, the observed d -wave resonance peak is not very pronounced even though the total cross section grows by a factor of ~ 4 with respect to the zero energy limit. However, when the effect of depletion is included [21] we obtain good agreement between the experimental and theoretical scattering fractions [Fig. 3(c)]. The model predicts the d -wave resonance to occur at $275 \mu\text{K}$, and the measurements are consistent with this to within $25 \mu\text{K}$.

As is obvious from Fig. 2, the scattered particles are emitted in spatial patterns which depend on the collision energy. It is possible to relate these patterns to the differential cross section when the effects on the particle distribution of the harmonic potential and the projection onto the imaging plane are accounted for. As a result of

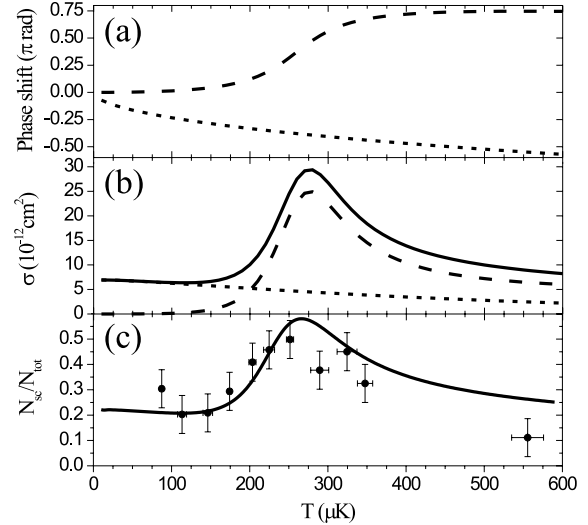


FIG. 3. Dependence on collision energy. (a) The s (dotted line) and d (dashed line) partial-wave phase shifts from the theoretical model. (b) The s -wave (dotted line), d -wave (dashed line), and total (solid line) cross sections calculated from the model partial-wave phase shifts. (c) The measured scattered fraction of atoms N_{sc}/N_{tot} (filled circles). The black curve shows the fraction as given by the model cross section when depletion of the colliding atom clouds is accounted for.

the scattered particles expanding in an anisotropic harmonic potential, the projected halos seen in Fig. 2 have elliptical envelopes rather than the circle expected for a free-space Newton sphere as shown in Fig. 1. However, due to the cylindrical symmetry about the collision axis (which is perpendicular to the optical axis of our imaging system), full 3D tomographical information on the scattering can be extracted from the 2D absorption images via the inverse Abel transform [17,22]. Applying Abel inversion to the absorption images gives us the angular particle distribution in the trap at the time of image acquisition, to which the distribution at the time of collision (the free-space distribution) is related in a straightforward manner [23].

In Fig. 4(a) we show polar plots of the probability density $n_{sc}(\theta, T) \propto d\sigma/d\Omega$ for a scattered particle to be emitted at the polar angle θ as determined from the absorption images in Fig. 2. The angular distributions for different temperatures have been normalized with respect to each other such that $\int n_{sc}(\theta, T)d\Omega = 1$ for all T and were determined from the Abel inverted images by counting the particles within angular bins at a unit sphere transformed to the quarter period ellipsoid via the relation in Ref. [23]. For comparison we present in Fig. 4(b) the temperature development of the normalized differential cross section as predicted by Eq. (1) using the partial-wave shifts from the previously described model. The scattering patterns of Figs. 4(a) and 4(b) show the same behavior and the minor discrepancies between the experimental and theoretical distributions may be attributed to

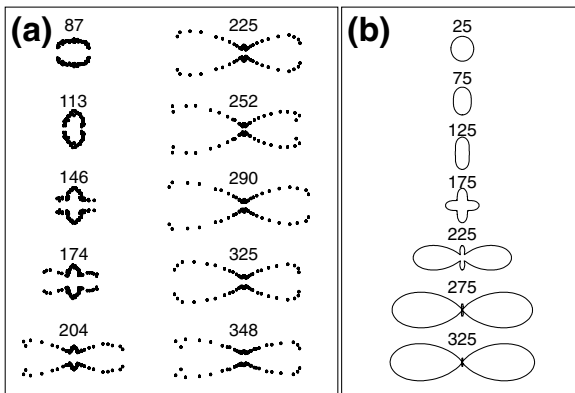


FIG. 4. Polar plots of the normalized angular scattering probability density for different collision energies in μK . (a) Experimental results from the absorption images of Fig. 2 after Abel inversion and a transformation from trap to free space. (b) Characteristic patterns as predicted by Eq. (1) using the partial-wave shifts from our theoretical model.

broadening effects from the finite sizes of the colliding clouds and a small departure from an ideal scattering geometry, both of which are not included in our analysis method [24]. For low temperatures the scattering is *s*-wave dominated and isotropic. However, at the onset of the *d*-wave scattering resonance the *s* and *d* partial-wave amplitudes interfere constructively in the radial direction and destructively in the axial direction. Above the *d*-wave resonance the scattering pattern is *d*-wave dominated, but nonvanishing *s*-wave scattering gives rise to destructive interference in the radial direction and constructive interference in the axial direction.

In conclusion, we have reported direct imaging of the scattered atoms in cold collisions of doubly spin-polarized ^{87}Rb . The emission patterns and the measured number of scattered atoms as a function of collision energy are described well by a theoretical model. The present experiment demonstrates, in particular, the quantum mechanical nature of the scattering of atoms. The underlying quantum mechanics reveals itself strikingly through the appearance of one of its most prominent features—interference—and as only two states are involved in the scattering, the interpretation becomes particularly simple. On a more subtle level the extended version of Pauli's exclusion principle gives rise to the absence of odd partial waves since the scattering particles are identical bosons. Finally, we note the possibility of extending our method to other important low-lying resonances, atoms in different spin states, and to heteronuclear collisions.

This work was supported by the Marsden Fund of New Zealand, Contract No. 02UOO080. N. K. acknowledges additional support from the Danish National Science Research Council. We thank V. Dribinski for providing us with a software implementation of the Abel inversion method of Ref. [22].

- *Electronic address: nk@physics.otago.ac.nz
- [1] H. Faxén and J. Holtsmark, *Z. Phys.* **45**, 307 (1927).
- [2] E. U. Condon and P. M. Morse, *Rev. Mod. Phys.* **3**, 43 (1931); P. M. Morse, *ibid.* **4**, 577 (1932).
- [3] S. Chu, *Rev. Mod. Phys.* **70**, 685 (1998); C. N. Cohen-Tannoudji, *ibid.* **70**, 707 (1998); W. D. Phillips, *ibid.* **70**, 721 (1998).
- [4] J. Weiner *et al.*, *Rev. Mod. Phys.* **71**, 1 (1999).
- [5] M. H. Anderson *et al.*, *Science* **269**, 198 (1995); K. B. Davis *et al.*, *Phys. Rev. Lett.* **75**, 3969 (1995).
- [6] B. DeMarco and D. S. Jin, *Science* **285**, 1703 (1999).
- [7] J. M. Gerton *et al.*, *Nature (London)* **408**, 692 (2000).
- [8] S. Inouye *et al.*, *Nature (London)* **392**, 151 (1998).
- [9] E. A. Donley *et al.*, *Nature (London)* **417**, 529 (2002); C. A. Regal *et al.*, *ibid.* **424**, 47 (2003).
- [10] S. Jochim *et al.*, *Science* **302**, 2101 (2003); M. Greiner, C. A. Regal, and D. S. Jin, *Nature (London)* **426**, 537 (2003); M.W. Zwierlein *et al.*, *Phys. Rev. Lett.* **92**, 120403 (2004).
- [11] H. R. Thorsheim, Y. Wang, and J. Weiner, *Phys. Rev. A* **41**, 2873 (1990).
- [12] R. Legere and K. Gibble, *Phys. Rev. Lett.* **81**, 5780 (1998).
- [13] A. P. Chikkatur *et al.*, *Phys. Rev. Lett.* **85**, 483 (2000).
- [14] H. M. J. M. Boosten *et al.*, *Phys. Rev. A* **55**, 636 (1997).
- [15] S. Geltman, *Topics in Atomic Collision Theory* (Academic Press, New York, 1969).
- [16] $l = \{1, 3, 5, \dots\}$ terms are strictly forbidden and $l = \{4, 6, 8, \dots\}$ terms have been calculated to be completely negligible for the energy interval of interest.
- [17] R. N. Bracewell, *The Fourier Transform and Its Applications* (McGraw-Hill, Singapore, 2000), 3rd ed.
- [18] T. Esslinger, I. Bloch, and T.W. Hänsch, *Phys. Rev. A* **58**, R2664 (1998).
- [19] N. R. Thomas, A. C. Wilson, and C. J. Foot, *Phys. Rev. A* **65**, 063406 (2002).
- [20] A. Marte *et al.*, *Phys. Rev. Lett.* **89**, 283202 (2002).
- [21] During collisions the densities n_i of the clouds labeled by $i = 1, 2$ are governed by the two coupled nonlinear partial differential equations $\partial_t n_i(x, y, z, t) = v_i \partial_z n_i \times (x, y, z, t) - |v| \sigma(T) n_1(x, y, z, t) n_2(x, y, z, t)$. Assuming the clouds to have initially Gaussian density distributions in all directions, this system was solved numerically to calculate the fraction of scattered particles and assess the scaling with the coupling parameter $\sigma(T)$. Because of the prolate cloud shapes we neglect multiple scattering events.
- [22] V. Dribinski *et al.*, *Rev. Sci. Instrum.* **73**, 2634 (2002).
- [23] A particle emitted in the polar angle θ_0 at time $t = 0$ from the center of the trap follows a trajectory so that $\tan\theta(t) = \tan\theta_0 \omega_z \sin(\omega_z t) / \omega_r \sin(\omega_z t)$.
- [24] As a consequence of the broadening, some scattered atoms reach their maximum radial excursion point before the time of image acquisition. This effectively transfers them to angular bins closer to the collision axis. The slight left-right pattern asymmetry observable for some collision energies is a combined result of the clouds having slightly different speeds in the laboratory frame, a small offset on the z axis between collision and trap centers, and the size difference between colliding clouds [N. Kjærgaard, A. S. Mellish, and A. C. Wilson, *New J. Phys.* (to be published)].

Chapter 4

BEC with interactions

4.1 Scatterings

4.1.1 Elastic scattering

Consider collision of two particles where the interaction is expressed as a conservative (thus elastic) potential. The potential consists of

- repulsive Fermi pressure, over Pauli principle of overlapping electron shells;
- van-der-Waals interaction induced by dipoles ($\sim r^{-6}$), whose typical range scales as tens of Å ($r_{\text{vdW}} \sim 30\text{\AA}$). The 3-body collisions are rare only for densities $n \ll (30\text{\AA})^{-3} \approx 1 \times 10^{19} \text{ cm}^{-3}$;
- dipolar interaction ($\sim r^{-3}$) for states with electron dipole, which is rare;
- magnetic interaction (weak).

The typical size here of the interior part is Bohr radius:

$$a_0 = \frac{4\pi\varepsilon_0\hbar}{m_e e^2} = 5.3 \times 10^{-11} \text{ m} \sim 0.53 \text{\AA}. \quad (4.1)$$

The quantum mechanical description of such elastic scattering is the ansatz:

$$\psi_{\mathbf{k}}(\mathbf{r}) = \underbrace{e^{ikz}}_{\text{in}} + \underbrace{\frac{e^{ikr}}{r} f(\theta, \phi, k)}_{\text{out}} \quad (4.2)$$

for large distances $|\mathbf{r}| \gg r_{\text{vdW}}$. The incoming wave is a plane wave and the outgoing one has a spherical wave front. Unless interested in the short-range physics, we only need to determine the scattering amplitude $f(\theta, \phi, k)$. When $f = 0$, there is no scattering at all. It is determined by the differential scattering cross section

$$||f(\theta, \phi, k)||^2 = \frac{d\sigma}{d\Omega} \quad (4.3)$$

that describes the probability of scattering into direction (θ, ϕ) .

To solve the problem, we can expand the amplitude in angular momentum eigenfunctions:

$$f(\theta, \phi, k) = \sum_{l', m'} c_{l', m'}(k) Y_{l', m'}(\theta, \phi). \quad (4.4)$$

The incoming wave is similarly

$$\psi_{\text{in}}(\theta, \phi, r) = \sum_{l, m} c_{l, m}(k) Y_{l, m}(\theta, \phi) \cdot \text{radial part.} \quad (4.5)$$

The scattering is described by the S tensor

$$S_{l, m, l', m'}(k) = \langle l, m | V | l', m' \rangle, \quad (4.6)$$

which is nonzero only when $l = l'$ and $m = m'$ if the potential is isotropic. Note that here l and m are orbital angular momentums of atoms around the center of mass of the two particle system. The kinetic energy associated with the angular momentum is

$$E_{\text{orb}} = \frac{\hbar^2 l(l+1)}{2\mu r^2}, \quad (4.7)$$

where μ is the reduces mass, and the total effective potential is

$$V_{\text{eff}}(r) = V(r) + E_{\text{orb}}. \quad (4.8)$$

Notice that for large r , there is a "centrifugal barrier". For low energies $k \rightarrow 0$ such that $E_{\text{kin}} \ll E_{\text{barrier}}$, the atoms only see outermost part of the effective potential, which is identical to non-interacting. Therefore scattering in $l > 0$ is suppressed and there is only s -wave collisions for low k and only $S_{0,0,0,0}$ is relevant! The total wave function for large r is thus (for two spherical wave)

$$\psi_k(r) \propto A_{\text{in}} \frac{e^{ikr}}{kr} + A_{\text{out}} \frac{e^{-ikr}}{kr}. \quad (4.9)$$

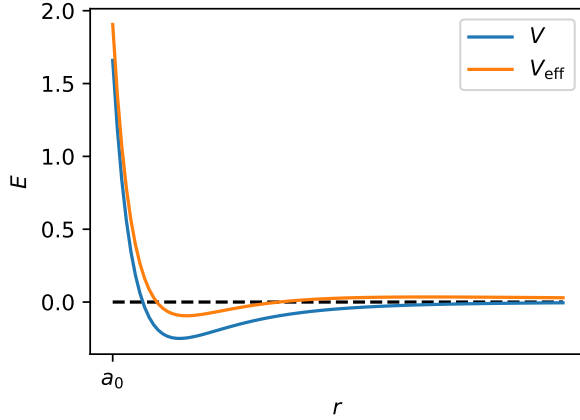


Figure 4.1: Effective molecule potential.

For conservation of mass, $|A_{\text{in}}| = |A_{\text{out}}|$, so only a phase remains:

$$\psi_k(r) \propto \frac{\sin(kr + \delta_s(k))}{kr}. \quad (4.10)$$

$\delta_s(k)$ is called *interaction phase shift*, which is 0 when $V(r) = 0$. For finite interaction, it must be $\mathcal{O}(k)$, otherwise $\psi_k(r)$ diverges when $k \rightarrow 0$. We can linearize it around $k = 0$:

$$\delta_s(k) = -a_s k + \mathcal{O}(k^2) \quad (4.11)$$

where

$$a_s := -\lim_{k \rightarrow 0} \frac{\tan \delta_s(k)}{k} \quad (4.12)$$

is the *s-wave scattering length*. The tan comes from more detailed derivations. As a result, the wave function is shifted for small k :

$$\psi_k(r) \propto \frac{\sin(k(r - a_s))}{kr} \quad (4.13)$$

and there is zero crossing at $r = a_s$.

The scattering amplitude can now be expressed as

$$f_s(k) = -\frac{1}{1/a_s + ik + \frac{r_{\text{eff}}}{2} k^2 + \dots}, \quad (4.14)$$

where r_{eff} is the *effective range* for the second order terms in the series. We can go to a different regime where the typical momenta is much larger than $1/a_s$, and the scattering becomes an a_s -independent universal process. It is therefore called *unitary regime*, that typically happens in fermionic gases with high Fermi momentum k_F and large a_s .

Examples

- Hard sphere potential. $V(r) = \infty$ when $r \leq r_0$ and 0 when $r > r_0$. The solution gives $a_s = r_0$.
- Repulsive box. $V(r) = V_0$ for $r \leq r_0$ instead. It gives a shift $0 < a_s < r_0$.
- Molecular potential. The shift can be both left or right, depending on precise shape of potential, which is difficult to compute for heavy particles. It is usually only measured.

Note that the total cross section in the s -wave approximation is $4\pi|a_s|^2$ only for distinguishable particles. For indistinguishable bosons, there will be an additional factor of 2 for two different scattering types (we cannot tell which particles is scattered). For indistinguishable fermions, there is no s -wave scattering and the cross section is 0.

4.1.2 Pseudo potential

In the section we decide which potential to be used in the Schrödinger equation. The assumptions are

- low k and therefore s -wave approximation;
- large $\lambda \gg r_{\text{vdW}}$;
- isotropic potential (\Rightarrow isotropic s -wave wave function \Rightarrow no s -wave scattering for identical fermions).

As discussed in the last section, this leads to a low- k scattering phase $\delta_s(k) \approx -ka_s$. A point like local potential that results in the same phase is required to avoid that r_{vdW} might be actually smaller than a_s , which can be found as

$$V(\mathbf{r}) = \frac{4\pi\hbar a_s}{\mu} \delta^3(\mathbf{r}). \quad (4.15)$$

This is valid only when $a_s \ll 1/k_\psi$, where k_ψ is the dominant k contribution to the wave function ψ . For $a_s \sim k_\psi$, a regularized δ -potential can be used as better approximation.

4.2 BEC with weak interaction

4.2.1 Second quantization formalism for BEC

The field operator in real space can be written as

$$\hat{\Psi}(\mathbf{r}) = \sum_k \phi_k(\mathbf{r}) \hat{a}_k. \quad (4.16)$$

Analogously the creation field operator is

$$\hat{\Psi}^\dagger(\mathbf{r}) = \sum_k \phi_k^*(\mathbf{r}) \hat{a}_k^\dagger \quad (4.17)$$

that acts on the vacuum state $|0\rangle$ to create a particle localized at \mathbf{r} :

$$\begin{aligned} \hat{\Psi}^\dagger(\mathbf{r}) |0\rangle &= \sum_k \phi_k^*(\mathbf{r}) \hat{a}_k^\dagger |0\rangle \\ &= \sum_k \langle \phi_k | \mathbf{r} \rangle |\phi_k\rangle = |\mathbf{r}\rangle. \end{aligned} \quad (4.18)$$

The commuting relations are

$$\begin{aligned} [\hat{\Psi}(\mathbf{r}), \hat{\Psi}^\dagger(\mathbf{r}')] &= \sum_{k,k'} \phi_k(\mathbf{r}) \phi_{k'}^*(\mathbf{r}') [\hat{a}_k, \hat{a}_{k'}^\dagger] \\ &= \sum_k \phi_k(\mathbf{r}) \phi_k^*(\mathbf{r}') \\ &= \sum_k \langle \mathbf{r} | \phi_k \rangle \langle \phi_k | \mathbf{r}' \rangle = \delta(\mathbf{r} - \mathbf{r}'), \\ [\hat{\Psi}(\mathbf{r}), \hat{\Psi}(\mathbf{r}')] &= 0. \end{aligned} \quad (4.19)$$

The density field operator can be similarly written as

$$\begin{aligned} \hat{n}(\mathbf{r}) &= \hat{\Psi}^\dagger(\mathbf{r}) \hat{\Psi}(\mathbf{r}) \\ &= \sum_k |\phi_k(\mathbf{r})|^2 \hat{a}_k^\dagger \hat{a}_k + \sum_{k \neq l} \phi_k^*(\mathbf{r}) \phi_l(\mathbf{r}) \hat{a}_k^\dagger \hat{a}_l. \end{aligned} \quad (4.20)$$

The first term is called the *density term*, while the second is the *coherence term*, which is nonzero if there is coherence in the state. Integrating over the density distribution, we can obtain the total atom number

$$\hat{N} = \int d\mathbf{r} \hat{n}(\mathbf{r}) = \sum_k \hat{a}_k^\dagger \hat{a}_k = \sum_k \hat{n}_k. \quad (4.21)$$

The interacting many body Hamiltonian

$$\hat{H} = \underbrace{\sum_i \left(-\frac{\hbar^2}{2m} \nabla_i^2 + U(\mathbf{r}_i) \right)}_{\hat{H}_0} + \underbrace{\frac{1}{2} \sum_{i \neq j} V_{\text{int}}(\mathbf{r}_i - \mathbf{r}_j)}_{\hat{H}_{\text{int}}} \quad (4.22)$$

can be rewritten in the second quantization form, if we replace the real potential $V(\mathbf{r})$ with the pseudo-potential $g\delta(\mathbf{r})$ (*repulsive!*):

$$\hat{H} \rightarrow \int d\mathbf{r} \hat{\Psi}^\dagger(\mathbf{r}) \left(-\frac{\hbar^2}{2m} \nabla^2 + U(\mathbf{r}) + \frac{1}{2} g \hat{\Psi}^\dagger(\mathbf{r}) \hat{\Psi}(\mathbf{r}) \right) \hat{\Psi}(\mathbf{r}). \quad (4.23)$$

Here

$$g = \frac{4\pi\hbar^2 a_s}{m}. \quad (4.24)$$

4.2.2 Gross-Pitaevskii equation

The Schrödinger equation

$$i\hbar \frac{\partial}{\partial t} \hat{\Psi}(\mathbf{r}, t) = [\hat{\Psi}(\mathbf{r}, t), \hat{H}] \quad (4.25)$$

gives, as one can expect,

$$i\hbar \frac{\partial}{\partial t} \hat{\Psi}(\mathbf{r}, t) = \left(-\frac{\hbar^2}{2m} \nabla^2 + U(\mathbf{r}) + g \hat{\Psi}^\dagger(\mathbf{r}) \hat{\Psi}(\mathbf{r}) \right) \hat{\Psi}(\mathbf{r}, t). \quad (4.26)$$

For weak interacting case, consider decomposing $\hat{\Psi} = \Psi + \delta\hat{\Psi}$, where a simple scalar field Ψ describes the density ($\langle \hat{n}(\mathbf{r}) \rangle = |\Psi(\mathbf{r})|^2$) and a fluctuation term $\delta\hat{\Psi}$ serves as perturbation such that $\langle \delta\hat{\Psi} \rangle = 0$ and

$$\langle \delta\hat{\Psi}^\dagger \delta\hat{\Psi} \rangle \ll |\Psi|^2. \quad (4.27)$$

The Schrödinger equation transforms now to the *Gross-Pitaevskii equation* (GPE)

$$i\hbar \frac{\partial}{\partial t} \Psi(\mathbf{r}, t) = \left(-\frac{\hbar^2}{2m} \nabla^2 + U(\mathbf{r}) + g \Psi^*(\mathbf{r}) \Psi(\mathbf{r}) \right) \Psi(\mathbf{r}, t). \quad (4.28)$$

It turns into a differential equation for a complex valued field, like the single particle *nonlinear Schrödinger equation* (NLSE). With effective energy μ , the time-independent form is

$$\left(-\frac{\hbar^2}{2m} \nabla^2 + U(\mathbf{r}) + g \Psi^*(\mathbf{r}) \Psi(\mathbf{r}) \right) \Psi(\mathbf{r}) = \mu \Psi(\mathbf{r}). \quad (4.29)$$

Validity. The energy consists of three parts: E_{kin} , E_{pot} and E_{int} . For the harmonic oscillator case, we have

$$\frac{E_{\text{int}}}{E_{\text{kin}} + E_{\text{pot}}} \sim \frac{N^2 |a_s| / a_{\text{HO}}^3}{N / a_{\text{HO}}^2} = \frac{N |a_s|}{a_{\text{HO}}}, \quad (4.30)$$

where N is the particle number and $a_{\text{HO}} \propto 1/\sqrt{\omega_{\text{HO}}}$ is the characteristic length of the potential. There are four regimes:

- $\frac{N |a_s|}{a_{\text{HO}}} \ll 1$: perturbative interactions. Wave functions stay unchanged, and interaction energies added as first order perturbations.
- $\frac{N |a_s|}{a_{\text{HO}}} \sim 1$: nonlinear regime. GPE is needed to find solutions of the Hamiltonian.
- $\frac{N |a_s|}{a_{\text{HO}}} \gg 1$: interaction dominated (Thomas Fermi regime).
- $\frac{|a_s|}{a_{\text{HO}}} \ll 1$: strongly correlated regime. Fluctuations can no longer be neglected.

4.2.3 Thomas-Fermi regime

Consider BEC in a harmonic trap. Repulsive interactions between the atoms will lead to the expansion of the cloud, which means the potential also increases. Therefore for the limit of large interaction, we expect $E_{\text{kin}} \ll E_{\text{pot}}, E_{\text{int}}$ and thus we have the *Thomas Fermi approximation* that simplifies the GPE to

$$\mu = U(\mathbf{r}) + g |\Psi(\mathbf{r})|^2. \quad (4.31)$$

This is not a differential equation, so the density is reduced to

$$n(\mathbf{r}) = |\Psi(\mathbf{r})|^2 = \frac{\mu - U(\mathbf{r})}{g} \quad (4.32)$$

for $U(\mathbf{r}) < \mu$ and 0 otherwise. The boundary where the density drops to 0 is called the Thomas Fermi radius R_{TF} . In the harmonic oscillator, it is obviously by construction always larger than the length of harmonic oscillator in the TF regime:

$$R_{\text{TF}} = a_{\text{HO}} \left(\frac{15 N a_s}{a_{\text{HO}}} \right)^{1/5}. \quad (4.33)$$

The chemical potential μ can be determined by integrating the particle number over the whole space:

$$\mu = \frac{\hbar\omega_0}{2} \left(\frac{15Na_s}{a_{\text{HO}}} \right)^{2/5}. \quad (4.34)$$

At the edges of the cloud, where the density drops towards zero, there will however always be a region where the density – and therefore the interaction energy density – is so low that the assumption of a large interaction contribution does not hold, and the full GPE would have to be applied. For very large particle numbers, however, this will only matter in a small region of the overall system. The length scale of this region can be found by comparing the kinetic and interaction energy densities:

$$\epsilon_{\text{kin}} = \frac{\hbar^2}{2m} \cdot \frac{1}{\xi^2} n = gn^2 = \epsilon_{\text{int}}, \quad (4.35)$$

which gives

$$\xi = \frac{1}{\sqrt{8\pi a_s n}}. \quad (4.36)$$

This is called the *healing length*, the length scale of interaction.

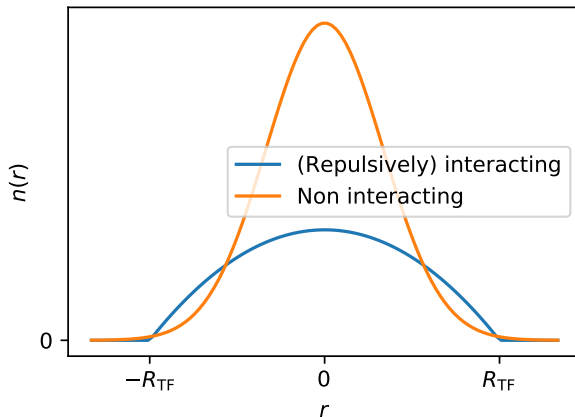


Figure 4.2: Density distribution of BEC in harmonic trap.

4.2.4 Attractive interactions

We are so far talking about repulsive interactions. Both the real and pseudo interaction potentials can be actually attractive. In that case, the weak

and intermediate interaction discussion does not necessarily change, but for stronger interactions the behavior is different. The shape of cloud will *contract* and hence the contribution of the kinetic energy term will increase rather than decrease; the potential contribution will conversely decrease. The system could become more and more condensed and finally collapses (*Bose Nova*), becoming a non-BEC gas after being heated up significantly. There is however another probability to find a new equilibrium size which is smaller than the non-interacting one. A common approach is to compute the Hamiltonian for a trial wave function of variable size. For harmonic oscillators, a Gaussian gives us

$$\Psi(\mathbf{r}) = \left(\frac{N}{w^3 a_{\text{HO}}^3 \pi^{3/2}} \right)^{1/2} e^{-\frac{r^2}{2w^2 a_{\text{HO}}^2}}, \quad (4.37)$$

where w characterizes the interaction strength and particle number. The total energy of such a trial function ends in

$$E = \frac{1}{2} N \hbar \omega_{\text{HO}} \left[-\underbrace{\sqrt{\frac{\pi}{2}} \cdot \frac{N|a_s|}{a_{\text{HO}}} \frac{1}{w^3}}_{E_{\text{int}}} + \underbrace{\frac{3}{2} \left(\underbrace{\frac{1}{w^2}}_{E_{\text{kin}}} + \underbrace{w^2}_{E_{\text{trap}}} \right)}_{E_{\text{tot}}} \right]. \quad (4.38)$$

A local minimum (and thus equilibrium size) can be obtained only if the first derivative of the LHS of Eq. (4.38) has a zero, which gives

$$w^5 - w + z = 0, \quad z := \sqrt{\frac{\pi}{2}} \cdot \frac{N|a_s|}{a_{\text{HO}}}. \quad (4.39)$$

We can make use the inequality for $a, b > 0, n \in \mathbb{Z}^+$:

$$\begin{aligned} a^n + b &= (n+1) \cdot \frac{a^n + \frac{b}{n} \cdot n}{n+1} \geq (n+1) \sqrt[n+1]{a^n \cdot \left(\frac{b}{n}\right)^n} \\ &\Rightarrow ab \leq \left(\frac{a^n + b}{n+1}\right)^{\frac{n+1}{n}} \cdot n \end{aligned} \quad (4.40)$$

by organizing the equation a bit and take $n = 4$:

$$z = w(1 - w^4) \leq \left(\frac{w^4 + 1 - w^4}{5} \right)^{\frac{5}{4}} \cdot 4 = 4 \cdot 5^{-5/4} \approx 0.535. \quad (4.41)$$

The equal sign is taken when $w^4 = (1 - w^4)/4$, which corresponds to the critical variational parameter

$$w_c = 5^{-1/4} \approx 0.669 \quad (4.42)$$

and critical particle number

$$N_c = 4 \cdot 5^{-5/4} \cdot \sqrt{\frac{2}{\pi}} \cdot \frac{a_{\text{HO}}}{|a_s|} \approx 0.427 \frac{a_{\text{HO}}}{|a_s|}. \quad (4.43)$$

4.3 Excitation of (weakly interacting) BECs

4.3.1 solitons in 1D

So far we are dealing with approximated GPE under different assumptions to deal with the nonlinear term. There are however exact analytical solutions of GPE, with forms of solitary waves, or *solitons*. Solitons serve as low-lying excitations of interacting BEC. They are more generally stationary solutions of nonlinear wave equations; dispersion needs to be compensated by the nonlinear term.

Dark solitons. For repulsive interactions, the soliton wave function is a wall that moves at speed u :

$$\psi(x, t) = \sqrt{n} \left[i \frac{u}{s} + \sqrt{\left(1 - \frac{u^2}{s^2}\right)} \tanh \left(\frac{x - ut}{\sqrt{2}\xi_u} \right) \right] e^{-i\mu t/\hbar}, \quad (4.44)$$

where $s = \sqrt{ng/m}$ is the sound velocity of the uniform condensate and ξ_u is the "relativistic" healing length:

$$\xi_u = \frac{\xi}{\sqrt{1 - u^2/s^2}}. \quad (4.45)$$

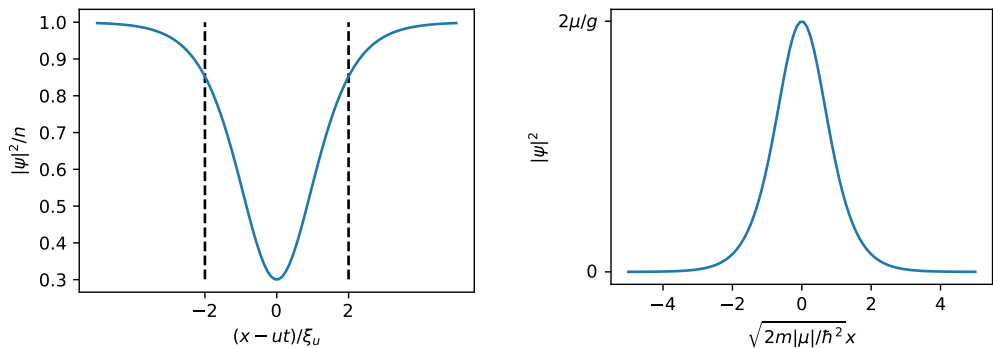


Figure 4.3: Density of (left) dark soliton for $u^2 = 0.3s^2$; (right) bright soliton.

As shown in left plot of Fig. 4.3, it causes a hole of length scale ξ , the healing length, which is effectively the threshold distance for disturbance to be detected. Such solitons are therefore called *dark solitons*. Notice that the phase of the wave function jumps discontinuously right at the wall, and hence it is also referred to as a *kink*.

Bright solitons. For attractive interaction, the one-dimensional soliton solution has a maximum in particle density instead of a minimum. For such *bright solitons* to exist, the chemical potential μ has to be negative and

$$\psi(x, t) = \left(\frac{2\mu}{g}\right)^{1/2} \frac{1}{\cosh(\sqrt{2m|\mu|/\hbar^2}x)} e^{-i\mu t/\hbar}. \quad (4.46)$$

Different from the dark solitons, the density vanishes at large distances from the center. If we fill the dark soliton with a bright soliton, the so-called dark-bright solitons can be obtained, which are much more stable.

4.3.2 Solitons in 2D

2D solitons are just linear combinations of x, y 1D solitons. Consider the harmonic oscillator, whose solutions are separable in different directions. Note that

$$|0_x\rangle \propto \exp\left(-\frac{x^2}{2a_{\text{HO}}^2}\right), \quad |1_x\rangle \propto x \exp\left(-\frac{x^2}{2a_{\text{HO}}^2}\right). \quad (4.47)$$

The most trivial superposition of the first excited states in two directions is

$$|\psi_{\text{trivial}}\rangle = \frac{1}{\sqrt{2}} (|1_x 0_y\rangle + |0_x 1_y\rangle), \quad (4.48)$$

but we are more interested in the vortex state

$$|\psi_{\text{vortex}}\rangle = \frac{1}{\sqrt{2}} (|1_x 0_y\rangle + i|0_x 1_y\rangle). \quad (4.49)$$

The latter is a circular flow around the centre. For more general (multi-)vortex fields, we can define the circulation

$$K = \oint \mathbf{v} \cdot d\mathbf{r} = \frac{e2\pi\hbar}{m} \quad (4.50)$$

Here $e \in \mathbb{Z}$ is the total charge of flow and the effective velocity is $\mathbf{v}(\mathbf{r}) = \nabla\phi(\mathbf{r})/m$, where $\phi(\mathbf{r})$ is the phase of the wavefunction: $e^{i\phi(\mathbf{r})/\hbar} = \psi(\mathbf{r})/|\psi(\mathbf{r})|$. Therefore when the charges are centred,

$$v = \frac{K}{2\pi r} = \frac{\hbar e}{mr}. \quad (4.51)$$

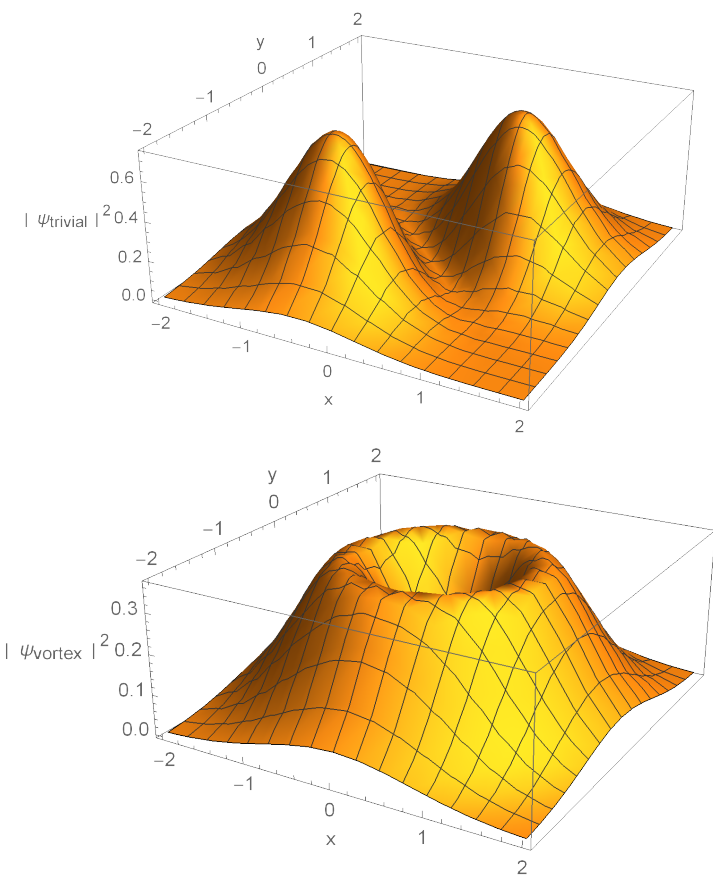


Figure 4.4: Density distributions of $|\psi_{\text{trivial}}\rangle$ and $|\psi_{\text{vortex}}\rangle$ in 2D.

The kinetic energy of a vortex with charge e is if we assume constant density n (all in 2D):

$$\begin{aligned} E_{\text{kin}} &= \frac{m}{2} \int_{\xi}^R d\mathbf{r} v(\mathbf{r})^2 n(\mathbf{r}) \\ &= \frac{\pi \hbar^2 n e^2}{m} \ln \frac{R}{\xi}, \end{aligned} \quad (4.52)$$

where R is the size of the system and ξ is the size of the core. Similarly, for two vortices with charges e_1 and e_2 at distance d , the interactions between them are

$$E_{\text{int}} = \frac{\pi \hbar^2 n e_1 e_2}{m} \ln \frac{R}{d}, \quad (4.53)$$

which is repulsive for the same sign of charges (co-rotating) and attractive for different signs of charges (counter-rotating).

Experimental realization To get such 2D soliton experimentally, we can start with classical gas in the rotating frame and then condense it. The Hamiltonian of a harmonic oscillator in the rotating frame is

$$\hat{H} = \frac{\hat{p}^2}{2m} + \frac{1}{2} m \omega_{\text{HO}}^2 \mathbf{r}^2 + \Omega \hat{L}_z. \quad (4.54)$$

Ω is the rotation frequency that shifts the Hamiltonian.

In the non-rotating frame, the ground state energy is

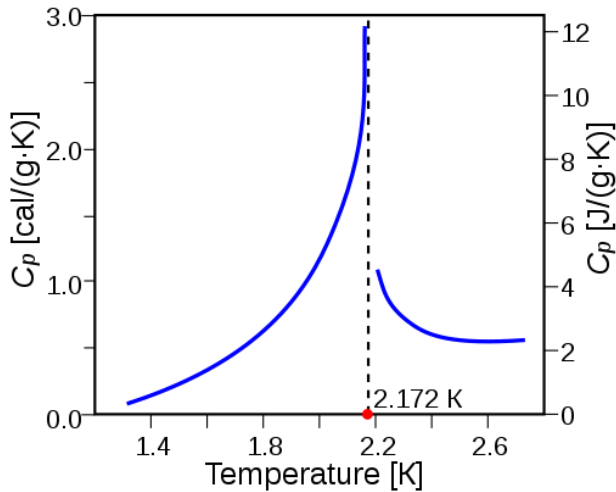
$$E_0 = \frac{3}{2} \hbar \omega_{\text{HO}}. \quad (4.55)$$

The first two degenerated excited states with $\langle \hat{L} \rangle = \hbar$ and $\langle \hat{L}_z \rangle = \pm \hbar$ are exactly the vortex states we want ($\langle \hat{L}_z \rangle = \hbar$ corresponds to $|\psi_{\text{vortex}}\rangle$, and the other is for different chirality). Their energy is

$$E_{1,2} = E_{\text{vortex}} = \frac{5}{2} \hbar \omega_{\text{HO}}. \quad (4.56)$$

In the rotating frame, E_0 stay unchanged while $E_{1,2}$ become non-degenerated: $\tilde{E}_{1,2} = E_1 \pm \hbar \Omega$. Therefore when $\Omega > \omega_{\text{HO}}$, the vortex state is lowered to be the ground state. When the rotating frequency is too large $\Omega \gtrsim \Omega_m$, however, all the particles will be dumped out and nothing is left.

In the middle regime ($\omega_{\text{HO}} < \Omega < \Omega_m$) there could be multiple vortices in a honeycomb lattice! We can have a semi-classical view of why there is a uniform lattice distribution. For fixed rotating frequency, $v = \Omega r$ and the circulation at radius r is $2\pi r \Omega r = 2\Omega \pi r^2$. Thus the charge density $e/A = 4\pi m \Omega / \hbar$, which is a constant everywhere.

Figure 4.5: Heat capacity in Lambda transition of ${}^4\text{He}$.

Superfluidity and superconductivity

The properties of the low-energy excitations strongly influence the macroscopic properties of the BEC as a whole, superfluidity and superconductivity being quite spectacular examples.

The effect of superconductivity was discovered in 1911 by Heike Kamerlingh Onnes, as he worked on reaching colder temperatures using novel cooling processes based on classical thermodynamic heat pumping effects with helium gas. He discovered that, when cooling solid mercury to temperatures below a critical temperature of $T_c = 4.2 \text{ K}$, the electrical resistivity would suddenly drop to a negligibly small value.

In contrast, the superfluidity of liquid ${}^4\text{He}$ was discovered later, in 1928 in the liquid flow between two reservoirs: If two reservoirs at pressures p_1 and p_2 are connected by a small “leak channel”, the flow velocity will classically be proportional to the pressure difference $\Delta p = p_1 - p_2$, so that the viscosity which is proportional to $v/\Delta p$ is finite, where v is the flow velocity. When liquid ${}^4\text{He}$ is cooled below 2.17 K , it was however discovered that in the limit of low pressure, $\lim_{\Delta p \rightarrow 0} v(\Delta p)/\Delta p$ diverges and hence no finite value of viscosity is found. This corresponds to a phase transition between two phases of liquid helium, called He-I and He-II. In addition, it is found that the heat capacity C_p of the liquid diverges at the same critical temperature, called T_λ . Functional dependence of the heat capacity on the temperature in the form of the λ character gave this transition the name “Lambda-transition”.

4.4 Journal Club 5: Solitons (Becker et al., 2008)

- *What is the selling point of this paper?*

They observed the oscillations of dark and dark-bright solitons in the time scale of 250 ms and 2 s respectively. The reflection of a dark soliton bouncing off a filled soliton could also be observed.

- *How do they create the solitons?*

They use a spatial light modulator to imprint a phase step by exposing part of the condensate to a far-detuned laser beam. Then the density dip can be filled with atoms in another state to form a dark-bright soliton.

- *Why do the solitons oscillate?*

The phase gradient leads to the superfluid velocity, which is the negative of soliton velocity as it has negative mass. Near the edges the depth of the soliton decreases and the local phase gradient vanishes, so the soliton will stop instead of pushing out. More detailed analysis shows that the position z of the soliton is governed by $m\ddot{z} = -\frac{1}{2}\frac{\partial V}{\partial z}$.

- *How is the interactions between solitons observed?*

An additional dark soliton is always generated when prepare the dark-bright soliton. In Fig. 3 (d), when the dark soliton approaches the position of the dark-bright soliton, it is reflected backwards.

Oscillations and interactions of dark and dark–bright solitons in Bose–Einstein condensates

CHRISTOPH BECKER¹, SIMON STELLMER¹, PARVIS SOLTAN-PANAHI¹, SÖREN DÖRSCHER¹,
MATHIS BAUMERT¹, EVA-MARIA RICHTER¹, JOCHEN KRONJÄGER¹, KAI BONGS²
AND KLAUS SENGSTOCK^{1*}

¹Institut für Laser-Physik, Universität Hamburg, Luruper Chaussee 149, 22761 Hamburg, Germany

²MUARC, School of Physics and Astronomy, University of Birmingham, Edgbaston, Birmingham B15 2TT, UK

*e-mail: sengstock@physnet.uni-hamburg.de

Published online: 4 May 2008; doi:10.1038/nphys962

Solitons are among the most distinguishing fundamental excitations in a wide range of nonlinear systems such as water in narrow channels, high-speed optical communication, molecular biology and astrophysics. Stabilized by a balance between spreading and focusing, solitons are wave packets that share some exceptional generic features such as form stability and particle-like properties. Ultracold quantum gases represent very pure and well-controlled nonlinear systems, therefore offering unique possibilities to study soliton dynamics. Here, we report on the observation of long-lived dark and dark–bright solitons with lifetimes of up to several seconds as well as their dynamics in highly stable optically trapped ⁸⁷Rb Bose–Einstein condensates. In particular, our detailed studies of dark and dark–bright soliton oscillations reveal the particle-like nature of these collective excitations for the first time. In addition, we discuss the collision between these two types of solitary excitation in Bose–Einstein condensates.

Nowadays, solitons are a very active field of research in many areas of science. They are characterized as localized solitary wave packets that maintain their shape and amplitude owing to a self-stabilization against dispersion through a nonlinear interaction. Although an early theoretical explanation of this non-dispersive wave phenomenon was given by Korteweg and de Vries in the late nineteenth century, it was not until after 1965 that numerical simulations of Zabusky and Kruskal theoretically proved that these solitary waves preserve their identity in collisions^{1,2}. This revelation led to the term ‘soliton’ for this type of collective excitation.

Bose–Einstein condensates (BECs) of weakly interacting atoms build up a macroscopic wavefunction described by a nonlinear Schrödinger equation and therefore enable studies of solitons. In this respect, the existence and some fundamental properties of solitons have been deduced from a few experiments with BECs. Bright solitons, characterized as non-spreading matter-wave packets, have been observed in BECs with attractive interaction^{3–5} where they represent the ground state of the system. In a repulsively interacting condensate confined in a periodic potential, bright gap solitons have been realized^{6,7} by modelling a suitable anomalous dispersion.

BECs with repulsive interactions allow for dark-soliton solutions, characterized by a notch in the density distribution. In contrast to bright solitons, dark solitons are truly excited states with energies greater than the underlying BEC ground state. Dark solitons have been generated in a few pioneering experiments^{8–10}, boosting an immense theoretical interest in these nonlinear structures in BECs. Dynamical^{10–17} and thermodynamical^{18–20}

instabilities as well as collisional properties^{21,22} have been analysed theoretically in great detail. Moreover, the existence of bright solitons stabilized by the presence of dark solitons in another quantum state in repulsive BECs has been proposed¹⁶ and confirmed in a proof-of-principle experiment¹⁰. The occurrence of undamped oscillations of solitons in axially harmonic traps comparable to those of a single particle has been predicted by mean field theory^{16,19}, see also ref. 23, and supported by numerical simulations¹⁸ for dark solitons and appears as one of the paradigms of soliton physics in BECs as it clearly demonstrates the particle-like character of the soliton. Limited by very short lifetimes in previous experiments however, oscillations of dark solitons have not been observed yet.

Here, we show that very long-lived dark solitons can be generated in BECs, facilitating detailed studies of soliton oscillations as well as the creation of dark–bright solitons by filling the dark soliton with atoms in another hyperfine state. In addition, the reflection of a dark soliton off a filled soliton has been observed and is presented. In the following, we give a brief introduction to the description of solitons in BECs and characteristic properties of soliton dynamics.

DARK SOLITONS IN BECS

Close to absolute zero temperature, where thermal fluctuations can be neglected to first order, the condensate is well described within the framework of the nonlinear Gross–Pitaevskii equation²⁴ (GPE), which is known to support soliton solutions as it is closely related

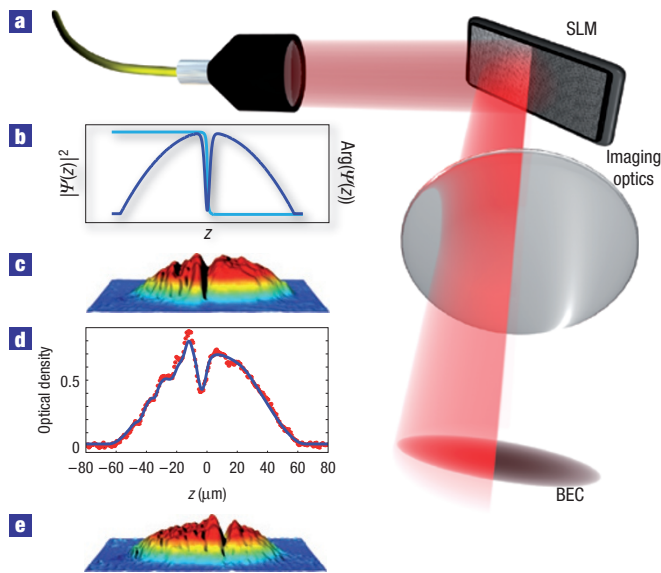


Figure 1 Principle of dark-soliton generation. **a**, Optical set-up. A spatial light modulator (SLM) is used to imprint a phase step by exposing part of the condensate to a far-detuned laser beam. **b**, Theoretical curve of a dark soliton's density $|\psi|^2$ (dark blue line) and phase ϕ (light blue line), as described by equation (1). **c**, A typical absorption image of the condensate, taken directly after preparation of the soliton and a subsequent free expansion of 11 ms. Optical density is colour- and height-coded for better visibility. **d**, Integrated column density (red circles) of the data in **c** together with a fit to the data (dark blue line). **e**, Image of a soliton after an evolution time of 2.8 s.

to the cubic nonlinear equation vastly used in nonlinear optics to describe solitary wave propagation in optical fibres²⁵

$$i\hbar\dot{\psi}(z, t) = -\frac{\hbar^2}{2m}\psi''(z, t) + [V_{\text{ext}}(z) + g|\psi(z, t)|^2]\psi(z, t).$$

Here, ψ denotes the condensate wavefunction; $g = 2\hbar\omega_{\perp}a$ is a measure of the nonlinear atomic interaction in quasi-one-dimensional (1D) geometries with strong transverse confinement. g is determined by the s -wave scattering length a and the transverse trapping frequency ω_{\perp} . V_{ext} describes a confining external potential. A dark-soliton solution to the GPE of a homogeneous BEC describing a density notch at position q propagating along z with a velocity \dot{q} can be written as^{26,27}

$$\psi_D(z, t) = \sqrt{n_0} \left\{ i\frac{\dot{q}}{\bar{c}_s} + \sqrt{1 - \frac{\dot{q}^2}{\bar{c}_s^2}} \tanh[\kappa(z - q(t))] \right\} e^{-ign_0t/\hbar}, \quad (1)$$

where the speed of sound in a quasi-1D condensate is given by $\bar{c}_s = \sqrt{n_0 g / 2m}$ and n_0 is the peak density of the condensate. The inverse size of the soliton κ is determined by the healing length $\xi = \hbar/m\bar{c}_s$ and the soliton speed \dot{q} through $\kappa = \xi^{-1} \times \sqrt{1 - (\dot{q}/\bar{c}_s)^2}$. Note that in a quasi-1D condensate, the averaging of the density over the radial degrees of freedom effectively changes the speed of sound to $\bar{c}_s = c_s/\sqrt{2}$ and the healing length to $\xi = \sqrt{2}\xi$ as compared with their 3D values c_s and ξ respectively. The phase and density distributions of a dark soliton are shown schematically in Fig. 1b. The phase only shows significant changes in the vicinity of the nodal plane of the soliton and is constant otherwise. Crossing the nodal plane of the soliton, the wavefunction accumulates a specific phase slip between 0 and π depending on the depth and

speed of the soliton related by $n_s/n_0 = 1 - (\dot{q}/\bar{c}_s)^2 = \sin^2(\phi/2)$, where n_s denotes the missing density at the position of the soliton. A phase jump of $\Delta\phi = \pi$ corresponds to a fully modulated soliton with zero velocity representing the only time-independent soliton solution of the GPE. As the phase difference diminishes the soliton velocity increases while it gets shallower and wider, ultimately vanishing at the speed of sound. The preceding considerations have led to the idea and experimental realization of creating dark solitons in BECs by optically imprinting a phase gradient of approximately π over a spatial region not larger than the healing length^{8,9,28}.

Whereas solitons in quasi 1D BECs are dynamically stable^{12,19}, experiments^{9,10} and intensive theoretical studies suggest that in less constrained geometries, where the condition $\gamma = n_0 g / \hbar\omega_{\perp} \ll 1$ is not perfectly met, the growth of dynamically unstable modes will lead to a transfer of kinetic energy of the soliton to radial excitation modes of the condensate, mediated by the atomic interaction and resulting in a bending of the soliton plane⁹, which may ultimately decay into a vortex ring as reported in ref. 10. As the energy of a dark soliton is always greater than the energy of the ground-state condensate, it is thermodynamically unstable in any case and shows fast decay even at reasonably low temperatures^{18,20,29} as observed in experiment^{8,9}. The dissipation accelerates the soliton according to its negative kinetic energy until it vanishes and smoothly transforms to the BEC ground state as it approaches the speed of sound¹⁹. This interesting aspect can be interpreted as an accelerating instability¹⁶ and implies that a negative mass can be assigned to a dark soliton. Lifetimes of the order of 10 ms have been reported, preventing the observation of more complex soliton physics such as oscillations or collisions.

We have developed a reliable, robust method to produce elongated ^{87}Rb BECs at extremely low temperatures in an optical trapping potential overcoming former technical limitations. We produce a BEC composed of 5×10^4 ^{87}Rb atoms in the $5^2S_{1/2}$, $F = 1$, $m_F = -1$ state in an optical dipole trap with trapping frequencies $\omega_z = 2\pi \times 5.9$ Hz, $\omega_{\perp}^{\text{ver}} = 2\pi \times 85$ Hz and $\omega_{\perp}^{\text{hor}} = 2\pi \times 133$ Hz with no discernible thermal fraction. Trap frequencies have been cross-checked by the measurement of various collective oscillations. Typical atomic peak densities are 5.8×10^{13} cm $^{-3}$, implying a speed of sound of $\bar{c}_s = 1.0$ mm s $^{-1}$. The chemical potential is of the order of 20 nK.

Ultradense laboratory conditions ensure exceptional reproducibility, enabling us to record time series of soliton dynamics with unprecedented precision. The low trap depth guarantees a slight but constant evaporative cooling, so that no heating can be detected for timescales as large as the lifetime of the condensate, which is greater than 10 s. Solitons are produced by optically imprinting a phase gradient as shown in Fig. 1a: a part of the condensate is exposed to the dipole potential U_{dip} of a laser beam detuned by some tens of gigahertz from atomic resonance. We image an optical mask pattern onto the BEC with diffraction-limited optical resolution of better than 2 μm . This results in a phase evolution of the masked relative to the unmasked part of the condensate of $\Delta\phi = U_{\text{dip}}t/(i\hbar)$. The pattern is generated by a spatial light modulator (SLM) with an effective pixel size of 0.8 μm allowing for almost arbitrary optical potentials³⁰. To imprint a phase slip of order π , we choose a pulse time $t_{\pi} = 40$ μs , much smaller than the correlation time $\tau_{\text{corr}} = \xi/\bar{c}_s = 700$ μs for our experimental parameters to avoid a simultaneous disturbance of the atomic density. This phase gradient leads to a local superfluid velocity of the condensate according to $v_{\text{SF}} = \hbar/m \partial_z \phi$, which can also be interpreted as a local potential gradient transferring momentum to the BEC, thus assisting the formation of a density minimum⁸. As a dark soliton can be regarded as a hole rather than a particle, it moves in the direction opposite to the superfluid flow

of the condensate. The appropriate equation of motion for small soliton velocities \dot{q} in a BEC that can be described by the Thomas–Fermi approximation is given by^{16,19}

$$m \ddot{q}(t) = -\frac{1}{2} \frac{\partial V(z)}{\partial z}. \quad (2)$$

The ratio of the negative soliton mass to the likewise negative Thomas–Fermi density potential of the BEC, $M_s/V_{\text{TF}}(z)$, is precisely twice the ratio of atomic mass to external potential $m/V(z)$. Therefore, the soliton behaves like a classical particle with mass $2m$. This implies a soliton oscillation frequency of $\omega = \omega_z/\sqrt{2}$ for harmonic trapping. The same result is obtained in the Thomas–Fermi regime in a harmonic trap using a local density approximation where the speed of sound \bar{c} is replaced by its local value $\bar{c}(z)$. Derived in this way, it has been shown that the equation of motion holds for almost arbitrary soliton velocities²³.

Figure 2a shows the time evolution of a dark soliton created by the aforementioned phase imprinting method. Absorption images were taken after a time-of-flight of 11.5 ms to enable the condensate and soliton to expand because the soliton size $l_s \approx \xi \approx 0.8 \mu\text{m}$ in the trap is beyond optical resolution. The soliton clearly propagates axially along the condensate with an initial velocity of $\dot{q} = 0.56 \text{ mm s}^{-1} = 0.56 \bar{c}_s$, indicating a relative soliton depth of $n_s = 0.68 n_0$. We were able to detect nearly pure dark solitons after times as long as 2.8 s in single experimental realizations (Fig. 1e), surpassing lifetimes of dark solitons in any former experimental realization by more than a factor of 200. Fluctuations in the soliton position due to small preparation errors however prevent the observation of soliton oscillations for evolution times $\tau_{\text{evol}} \gg 250$ ms. The extraordinary long lifetimes facilitate the first observation of an oscillation of a dark soliton in a trapped BEC. An oscillation frequency of $\Omega = 2\pi \times (3.8 \pm 0.1)$ Hz has been recorded and could be followed for more than one period. Owing to the shallowness of our dipole trap, the atoms experience a full gaussian potential, which is less steep than harmonic leading to a larger amplitude-dependent oscillation period for the soliton. We have calculated the soliton oscillation frequency using equation (2) for a gaussian potential created by a laser beam with a waist of $125 \mu\text{m}$ with the observed soliton amplitude of $Z_s = 33 \mu\text{m}$ and find an oscillation frequency of $\Omega = 2\pi \times 4.0$ Hz. This is in good agreement with our experimental data. We also checked the validity of this model by calculating the frequency for shallower and therefore faster solitons and find very good agreement with experimental data. Furthermore, the observed amplitude enables a consistency check of the soliton depth. At the turning point of the soliton motion Z_s , the constant soliton depth equals the Thomas–Fermi density $n_{\text{TF}}(Z_s)$ of the condensate and interrupts the superfluid flow of atoms. At this point, the soliton starts to move in the opposite direction. Given the measured initial speed of the soliton and the observed density distribution of the condensate, Z_s can be calculated to be $36 \mu\text{m}$ and is in very good agreement with the measured value.

Another feature extracted from Fig. 2a is a density wave that travels in the opposite direction at a velocity equal to the speed of sound. The occurrence of such a density wave has been investigated theoretically and experimentally⁸ and has been attributed to the method of soliton generation through phase imprinting while leaving the instantaneous density distribution unchanged. The density waves die out after approximately 50 ms, leaving a flat BEC with only one soliton excitation.

Calculating the dimensionality parameter $\gamma = n_0 g / \hbar \omega_{\perp} = 3.7$ and comparing this value with the critical ratio γ_c given by Muryshev *et al.*²⁰, we find our soliton to be right on the edge of the region of dynamical stability. This is confirmed regarding the observed soliton lifetimes.

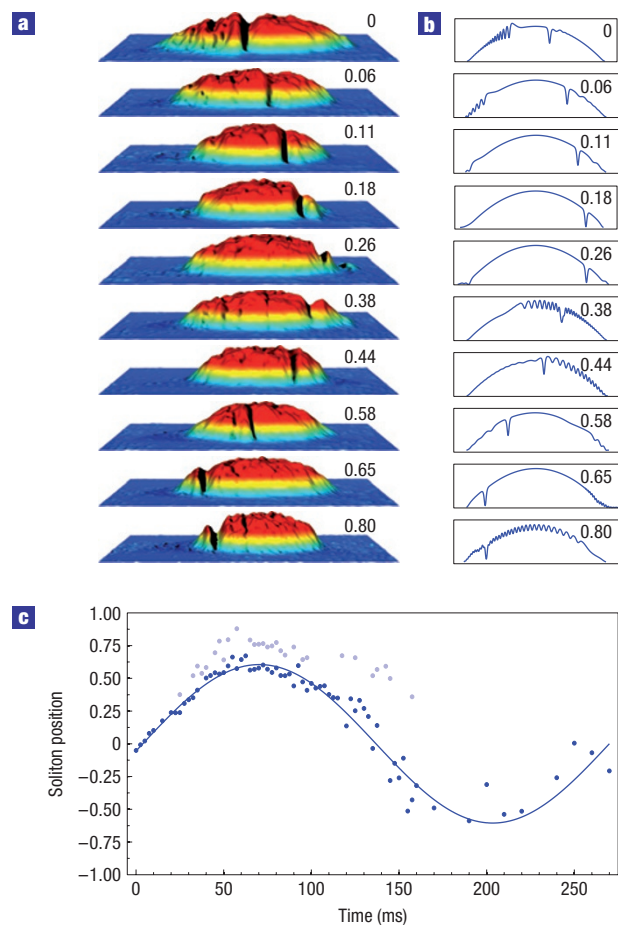


Figure 2 Dark-soliton oscillations in a trapped BEC. **a**, A set of absorption images showing the soliton position at various times after phase imprinting. The soliton propagates to the right and is reflected off the edge of the condensate after $t \approx 80$ ms. The corresponding evolution time for each image is given in units of the oscillation period T . **b**, Results of a numerical calculation solving the 1D Gross–Pitaevskii equation corresponding to our parameters in units of T . Experimentally observed features such as density modulations caused by a density wave on the left side of the condensate as well as the development of a tiny second soliton are reproduced. **c**, Axial positions of the soliton (dark blue dots) with respect to the centre of mass and normalized to the width of the condensate. The oscillation frequency is $\Omega = 2\pi \times (3.8 \pm 0.1)$ Hz. The position of a second tiny soliton (light blue dots) as well as a sinusoidal fit (blue line) to the position of the soliton are shown. Each data point was obtained from a different experimental run. The scatter is due to small fluctuations in the preparation process. Errors in extracting the soliton's position from the individual images are typically less than 0.02 and are therefore not plotted.

We have carried out numerical simulations of the 1D GPE showing that the phase imprinting method cannot create single perfect dark solitons but always creates density waves that carry away part of the imprinted phase gradient. Moreover, the occurrence of a second small soliton can be extracted from the simulations as shown in Fig. 2b.

The crucial feature to the observed long lifetimes of dark solitons seems to be the very low temperature of our samples. The critical temperature for Bose–Einstein condensation for our experimental parameters is (67 ± 5) nK. Estimating that a thermal fraction of at least 10% could have been detected in absorption imaging—which was not the case—an upper limit for

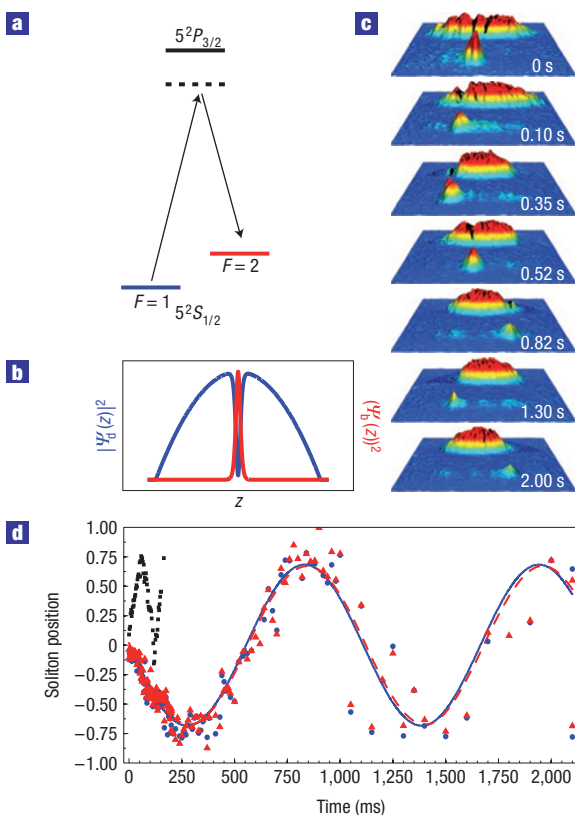


Figure 3 Creation and oscillation of a dark–bright soliton. **a,b**, A local population transfer in the centre of the trapped BEC is achieved by a coherent two-photon Raman process between the two hyperfine states $F = 1$ and 2 (**a**) leading to the generation of a dark–bright soliton (**b**). **c**, A set of double-exposure absorption images showing the density distributions of the two components that undergo slow oscillations in the axial direction. **d**, Time series of the axial positions of the dark (blue circles) and bright (red triangles) components of the soliton in addition to corresponding sinusoidal fits to the position. Note that the timescale is different by almost an order of magnitude as compared with that in Fig. 2c. An extra dark soliton (black squares) is also observed. For details of the first 175 ms, see Fig. 4.

the temperature of $T \leq 0.5 T_c = 30$ nK can be given, which is of the order of the chemical potential μ . We assume a significantly lower temperature, because temperatures of $T \approx 0.2 T_c$ would already considerably limit the soliton's lifetime¹⁸, which has not been observed in our experiment.

DARK-BRIGHT SOLITONS IN TWO-COMPONENT CONDENSATES

Despite the interesting physics that can be investigated using dark solitons, so-called dark–bright solitons appearing in multicomponent BECs show even more fascinating physical properties, such as enhanced dynamical stability and the possibility of bright-component particle exchange in soliton collisions. A dark–bright soliton is basically a dark soliton filled with atoms of a different species or in another internal state of an atomic matter wave^{31,32} (see the Methods section). A dark–bright soliton can be generated in a ⁸⁷Rb BEC by imprinting a dark soliton in state $|F = 1, m_F = 0\rangle$ and filling the density dip with atoms in state $|F = 2, m_F = 0\rangle$, leading to the density distribution shown in Fig. 3b. Whereas dark solitons are unstable to transverse excitations with wavelengths greater than their extension $l_s \approx \xi$, large dark–bright

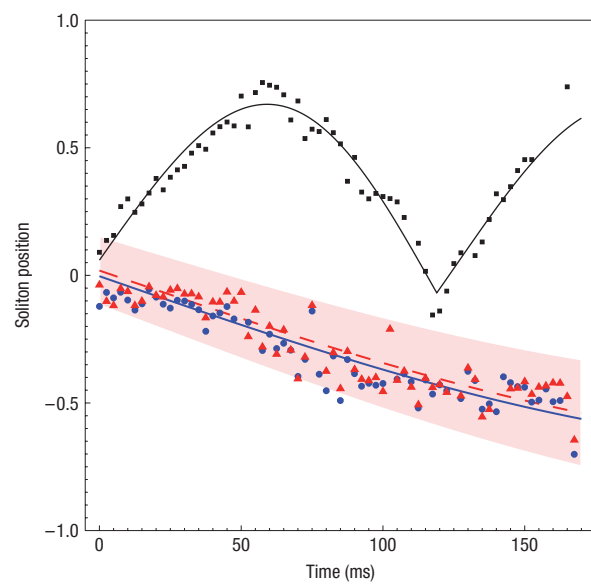


Figure 4 Collision of a dark and a dark–bright soliton. A detailed plot of the first 175 ms of Fig. 3 revealing the reflection of an extra dark soliton off the dark–bright soliton. The axial position of the extra dark soliton (filled squares) is plotted together with a fit to the data (lines). The mean e^{-2} width of the bright soliton is indicated (red shaded area). The reflection of the extra dark soliton is very close to that expected from a hard-wall reflection. The fit corresponds to a sine-function mirrored at the reflection time $t_r = 117$ ms.

solitons are expected to overcome this restriction because their size can be much larger than ξ when the number of atoms in the other hyperfine state becomes very large. Dark–bright solitons should therefore be robust in trap geometries that are not truly 1D. We have used a method to simultaneously imprint the phase gradient and transfer atoms to the other hyperfine state through a coherent Raman pulse technique using a laser system phase-locked on the two-photon hyperfine resonance $|F = 1, m_F = 0\rangle \rightarrow |F = 2, m_F = 0\rangle$ (Fig. 3a). Applying a 2π pulse of duration $40\ \mu s$ on one side of the condensate leaves the population effectively unchanged, but introduces a phase difference of π compared with the unperturbed part of the condensate. In a small region around the edge of the mask $l \approx \xi$, a transfer of the population to the $|F = 2, m_F = 0\rangle$ state occurs (Fig. 3b). By using a step-like intensity pattern rather than a simple edge, it is possible to vary the number of atoms transferred to the other hyperfine state by changing the width of the intermediate step. The mask pattern used in the experiment described here resulted in a bright-component population $N_B = 0.08 N_{\text{tot}}$, where N_{tot} is the total number of atoms. A time series of the propagation of such a dark–bright soliton is shown in Fig. 3c. After a short time-of-flight of 9 ms, the atoms are first exposed to a light pulse resonant only with $|F = 2\rangle$. After another 2 ms, the $|F = 1\rangle$ atoms are subsequently imaged. The dynamics of the dark–bright soliton could be followed for more than 2 s as seen in Fig. 3d. We observe an oscillation with a frequency of $\Omega_{\text{db}} = 2\pi \times (0.90 \pm 0.02)$ Hz = $0.24 \times \Omega$, much smaller than the frequency of the corresponding dark soliton. An expression for the oscillation frequency can be given using the equation of motion for very strongly populated dark–bright solitons³² and leads to

$$\Omega_{\text{db}} = \Omega \frac{\alpha_{z_{\text{max}}}}{\sqrt{2}} \left(\frac{4}{15} \frac{N_B R_z}{N_{\text{tot}} \xi} \right)^{-1},$$

where R_z denotes the radius of the BEC along the axial direction and $\alpha_{z\max}$ is an amplitude-dependent numerical factor that takes into account that the total potential experienced by the bright component depends on the inhomogeneous density of the dark component. For the observed values of N_b , R_z and N_{tot} , we calculate an oscillation frequency of $\Omega_{\text{db}} = 2\pi \times 1.27 \text{ Hz}$. This is in qualitative agreement with the observed value taking into account the assumption of a purely 1D model.

Another spectacular feature that can be extracted from this measurement is the interaction of a dark soliton with the much slower dark–bright soliton. Owing to the method of initial-state preparation, an extra dark soliton is always generated in addition to the dark–bright soliton. As shown in Fig. 4, the dark soliton propagates in the opposite direction as compared with the dark–bright one and oscillates back with the same frequency as a dark soliton in an unperturbed experiment. After 120 ms, it thus approaches the position of the dark–bright soliton, which has moved only very little owing to its much smaller oscillation frequency. The dark soliton is reflected off the dark–bright one comparable to a hard-wall reflection and moves back. To our knowledge, this is the first observation of collisions of different types of matter-wave soliton.

In summary, we have realized long-lived solitons in ^{87}Rb BECs and observed soliton oscillations for the first time. Through a combination of a local Raman transfer and a phase imprinting method, we could realize two-component solitary excitations called dark–bright solitons that clearly exhibit very slow oscillatory dynamics in a trapped BEC. As a first striking example of soliton interaction, the reflection of a dark soliton bouncing off a filled soliton could be observed. These experiments pave the way for further studies on solitons and soliton dynamics in ultracold quantum gases.

Note added in proof. Since the submission of our manuscript, we learned about related experiments³³.

METHODS

CREATION OF SOLITONS

We create BECs of ^{87}Rb atoms through trapping of up to 5×10^9 atoms in a 3D magneto-optical trap, sub-doppler cooling of these atoms and subsequently transferring them into a magnetic trap. We evaporatively cool the atoms slightly above the critical temperature T_c for Bose–Einstein condensation within 20 s. Afterwards, we superimpose a crossed dipole trap realized by a Nd:YAG laser beam focused to a waist of 35 μm and a perpendicular Ti:Sa laser beam (830 nm) focused to a waist of 125 μm . The atoms are loaded in this dipole trap and further cooled evaporatively by smoothly lowering the optical power of the dipole trap beams until we end up with an almost pure BEC of $5\text{--}10 \times 10^4$ atoms. We reduce the dipole trap power as much as possible to ensure the lowest temperatures of the BEC. The trapping frequencies for this configuration have been determined by several independent approaches and are $2\pi \times (5.9, 85, 133)$ Hz. At this stage, the condensate consists of atoms in the $|F=1, m_F=-1\rangle$ state and can be transferred to any other state or superposition of states through radiofrequency- or microwave-pulse or -sweep techniques. The state preparation is carried out at a sufficiently large magnetic offset field to avoid undesired spin-mixing dynamics³⁴. Moreover, the creation of dark–bright solitons demands a spatially selective transfer to the $|F=2, m_F=0\rangle$ state, which is accomplished by the use of a phase-locked Raman laser system with a relative phase error of not more than 0.44 rad. The optical transfer and phase imprinting is achieved by imaging a computer-generated pattern displayed on a spatial light modulator with a pixel size of 8 μm onto the BEC with an optical resolution of better than 2 μm . This is attained through a high-quality imaging optics with a magnification of 1/10. This optics is also used for the detection of BECs, yielding a magnification of 10. After creation of BECs in the optical dipole trap and the application of the phase imprinting light pattern via the SLM for a duration of 40 μs , we allow the BEC to evolve in the trap for a variable time τ_{evol} . Subsequently, we switch off the optical trapping potential

within 1 μs . In the experiments presented here, we take an absorption image of the expanded atomic cloud after a time-of-flight of 11 ms. Note that this is a destructive detection technique. For the measurements presented here, each data point therefore corresponds to a new realization of Bose–Einstein condensation, phase imprinting, evolution time and detection.

COUPLED GPE DESCRIBING DARK–BRIGHT SOLITONS

Following ref. 32, a two-component BEC can be described by a set of coupled GPEs. After a renormalization of energy $E' = E/(\hbar\omega_\perp)$, length $x' = x/\sqrt{\hbar/(m\omega_\perp)}$ and wavefunction $\psi'_i = \psi_i\sqrt{g_{ii}/(\hbar\omega_\perp)}$, where g_{ij} are intra- and inter-species interaction parameters, these equations are given by

$$\begin{aligned} i\dot{\psi}_d &= -\frac{1}{2}\psi''_d + (V_d + |\psi_d|^2 + g_d|\psi_b|^2 - \mu)\psi_d \\ i\dot{\psi}_b &= -\frac{1}{2}\psi''_b + (V_b + |\psi_b|^2 + g_b|\psi_d|^2 - \mu - \Delta)\psi_b, \end{aligned}$$

where ψ_d and ψ_b are the wavefunctions of the dark and bright components respectively, the V_i being external potentials and $\mu_b = \mu$ and $\mu_d = \mu + \Delta$ are the chemical potentials. The intra-species interaction parameters g_{ii} are normalized to unity, whereas the inter-species interaction parameters g_{ij} are very close to unity in the case of ^{87}Rb . The corresponding soliton solutions can be written as

$$\begin{aligned} \psi_d(z, t) &= i\sqrt{\mu}\sin\alpha + \sqrt{\mu}\cos\alpha\tanh\{\kappa(x - q(t))\} \\ \psi_b(z, t) &= \sqrt{\frac{N'_b\kappa}{2}}\operatorname{sech}\{\kappa(x - q(t))\}. \end{aligned} \quad (3)$$

$\cos\alpha$ is the depth of the dark soliton and N'_b is the rescaled number of particles in the bright component. Note that a phase factor has been omitted in ψ_b that is relevant only for collisions of bright solitons, which is beyond the scope of this work. $\kappa = \sqrt{\mu\cos^2\alpha + (N'_b/4)^2 - N'_b/4}$ is the inverse length of the dark–bright soliton, which is clearly expanded by the Thomas–Fermi-like repulsion of the bright component as compared with the unperturbed dark soliton. Rewriting this expression in SI units yields

$$\kappa\bar{\xi} = \sqrt{\cos^2\alpha + \left(\frac{4}{15}\frac{N_b R_z}{N_{\text{tot}}\bar{\xi}}\right)^2} - \frac{4}{15}\frac{N_b R_z}{N_{\text{tot}}\bar{\xi}}.$$

For our experimental parameters, we get $\kappa^{-1} = 6.7 \mu\text{m}$.

DETERMINATION OF SOLITON PARAMETERS

We have determined soliton parameters such as position, width and amplitude from 2D fits to the absorption images. The function used consists of a Thomas–Fermi-like density distribution for the BEC modulated with individual solitons basically given by the square of equation (1). The bright component has been fitted using equation (3).

Received 18 December 2007; accepted 2 April 2008; published 4 May 2008.

References

- Zabusky, N. J. & Kruskal, M. D. Interaction of solitons in a collisionless plasma and the recurrence of initial states. *Phys. Rev. Lett.* **15**, 240–243 (1967).
- Zabusky, N. J. Solitons and bound states of the time-independent Schrödinger equation. *Phys. Rev.* **168**, 124–128 (1968).
- Strecker, K. E., Partridge, G. B., Truscott, A. G. & Hulet, R. G. Formation and propagation of matter-wave soliton trains. *Nature* **417**, 150–153 (2002).
- Khaykovich, L. *et al.* Formation of a matter-wave bright soliton. *Science* **296**, 1290–1293 (2002).
- Cornish, S. L., Thompson, S. T. & Wieman, C. E. Formation of bright matter-wave solitons during the collapse of attractive Bose–Einstein condensates. *Phys. Rev. Lett.* **96**, 170401 (2006).
- Eiermann, B. *et al.* Dispersion management for atomic matter waves. *Phys. Rev. Lett.* **91**, 060402 (2003).
- Eiermann, B. *et al.* Bright Bose–Einstein gap solitons of atoms with repulsive interaction. *Phys. Rev. Lett.* **92**, 230401 (2004).
- Burger, S. *et al.* Dark solitons in Bose–Einstein condensates. *Phys. Rev. Lett.* **83**, 5198–5201 (1999).
- Denschlag, J. *et al.* Generating solitons by phase engineering of a Bose–Einstein condensate. *Science* **287**, 97–101 (2000).
- Anderson, B. *et al.* Watching dark solitons decay into vortex rings in a Bose–Einstein condensate. *Phys. Rev. Lett.* **86**, 2926–2929 (2001).
- Reinhardt, W. P. & Clark, C. W. Soliton dynamics in the collisions of Bose–Einstein condensates: An analogue of the Josephson effect. *J. Phys. B* **30**, L785–L789 (1997).
- Jackson, B., Kavoulakis, G. M. & Pethick, C. J. Solitary waves in clouds of Bose–Einstein condensed atoms. *Phys. Rev. A* **58**, 2417–2422 (1998).
- Feder, D. L., Pindzola, M. S., Collins, L. A., Schneider, B. I. & Clark, C. W. Dark-soliton states of Bose–Einstein condensates in anisotropic traps. *Phys. Rev. A* **62**, 053606 (2000).
- Brand, J. & Reinhardt, W. P. Solitonic vortices and the fundamental modes of the snake instability: Possibility of observation in the gaseous Bose–Einstein condensate. *Phys. Rev. A* **65**, 043612 (2002).

15. Muryshev, A. E., van Linden van den Heuvell, H. B. & Shlyapnikov, G. V. Stability of standing matter waves in a trap. *Phys. Rev. A* **60**, R2665–R2668 (1999).
16. Busch, Th. & Anglin, J. R. Motion of dark solitons in trapped Bose–Einstein condensates. *Phys. Rev. Lett.* **84**, 2298–2301 (2000).
17. Theocharis, G., Kevrekidis, P. G., Oberthaler, M. K. & Frantzeskakis, D. J. Dark matter-wave solitons in the dimensionality crossover. *Phys. Rev. A* **76**, 045601 (2007).
18. Jackson, B., Proukakis, N. P. & Barenghi, C. F. Dark-soliton dynamics in Bose–Einstein condensates at finite temperature. *Phys. Rev. A* **75**, 051601 (2007).
19. Fedichev, P. O., Muryshev, A. E. & Shlyapnikov, G. V. Dissipative dynamics of a kink state in a Bose-condensed gas. *Phys. Rev. A* **60**, 3220–3224 (1999).
20. Muryshev, A., Shlyapnikov, G. V., Ertmer, W., Sengstock, K. & Lewenstein, M. Dynamics of dark solitons in elongated Bose–Einstein condensates. *Phys. Rev. Lett.* **89**, 110401 (2002).
21. Carr, L. D., Brand, J., Burger, S. & Sanpera, A. Dark-soliton creation in Bose–Einstein condensates. *Phys. Rev. A* **63**, 051601 (2001).
22. Burger, S., Carr, L. D., Öhberg, P., Sengstock, K. & Sanpera, A. Generation and interaction of solitons in Bose–Einstein condensates. *Phys. Rev. A* **65**, 043611 (2002).
23. Konotop, V. V. & Pitaevskii, L. Landau dynamics of a grey soliton in a trapped condensate. *Phys. Rev. Lett.* **93**, 240403 (2004).
24. Pitaevskii, L. & Stringari, S. *Bose–Einstein Condensation* (Oxford Science Publications, Oxford, 2003).
25. Kivshar, Y. S. & Luther-Davies, B. Dark optical solitons: Physics and applications. *Phys. Rep.* **298**, 81–197 (1998).
26. Tsuzuki, T. Nonlinear waves in the Pitaevskii–Gross equation. *J. Low Temp. Phys.* **4**, 441–457 (1971).
27. Zakharov, V. E. & Shabat, A. B. Exact theory of two-dimensional self-focusing and one-dimensional self-modulation of waves in nonlinear media. *Sov. Phys. JETP* **34**, 62 (1972).
28. Dobrek, L. *et al.* Optical generation of vortices in trapped Bose–Einstein condensates. *Phys. Rev. A* **60**, R3381–R3384 (1999).
29. Parker, N. G., Proukakis, N. P., Leadbeater, M. & Adams, C. S. Soliton-sound interactions in quasi-one-dimensional Bose–Einstein condensates. *Phys. Rev. Lett.* **90**, 220401 (2003).
30. Boyer, V. *et al.* Dynamic manipulation of Bose–Einstein condensates with a spatial light modulator. *Phys. Rev. A* **73**, 031402 (2006).
31. Dum, R., Cirac, J. I., Lewenstein, M. & Zoller, P. Creation of dark solitons and vortices in Bose–Einstein condensates. *Phys. Rev. Lett.* **80**, 2972–2975 (1998).
32. Busch, Th. & Anglin, J. R. Dark–bright solitons in inhomogeneous Bose–Einstein condensates. *Phys. Rev. Lett.* **87**, 010401 (2001).
33. Weller, A. *et al.* Experimental observation of oscillating and interacting matter wave dark solitons. Preprint at <<http://arxiv.org/abs/0803.4352v1>>.
34. Kronjäger, J., Becker, C., Navez, P., Bongs, K. & Sengstock, K. Magnetically tuned spin dynamics resonance. *Phys. Rev. Lett.* **97**, 110404 (2006).

Acknowledgements

We thank the Deutsche Forschungsgemeinschaft DFG for financial support within the Forschergruppe FOR801 and the GRK 1355. K.B. thanks the EPSRC for financial support through grant EP/E036473/1.

Author information

Reprints and permission information is available online at <http://npg.nature.com/reprintsandpermissions>. Correspondence and requests for materials should be addressed to K.S.

Chapter 5

Ultracold atoms in periodic potentials

In this section we consider the motion of a particle in a periodic potential, which resembles particles in a crystal lattice in condensed matter physics. The simplest periodic optical potential is a retro-reflected standing wave, where a single-frequency light beam with wavelength λ is retro-reflected on a mirror, leading to a standing wave potential

$$V_{\text{lat}} = V_0 \sin^2(2\pi z/\lambda) = \frac{V_0}{2} (1 - \cos(2\pi z/a_{\text{lat}})), \quad (5.1)$$

where $a_{\text{lat}} = \lambda/2$ is the lattice period and $V_0/2\alpha I_0$ is the depth of the lattice potential with I_0 being the light intensity and α the polarizability of atoms for the particular light frequency.

5.1 Bloch theorem

In a periodic potential, the *Bloch theorem* holds to simplify the solution of Hamiltonian:

Theorem 5.1. *Every eigenfunction of a periodic single-body Hamiltonian can be written as a product of a plane wave function and a periodic function with the same periodicity as the Hamiltonian.*

The non-interacting eigenstate wavefunctions thus have the form

$$\phi_q^n(z) = e^{iqz} u_q^n(z), \quad (5.2)$$

where $u_q^n(z)$ are *Bloch functions* of periodicity a . q is referred as the *quasi-momentum* and the integer index n is the *band index*. The Bloch functions

can be expressed as a Fourier series due to the periodicity:

$$u_q^n(z) = \sum_{j=-\infty}^{\infty} c_{q,j}^n e^{i2\pi jz/a}. \quad (5.3)$$

Insert this into the wavefunction and we get

$$\phi_q^n(z) = \sum_{j=-\infty}^{\infty} c_{q,j}^n e^{iqz+i2\pi jz/a}, \quad (5.4)$$

which immediately allows us to only consider q within a interval of length 2π , for instance $-\pi/a \leq q < \pi/a$. Let $k_{q,j} = q + 2\pi j/a$.

Now consider the non-interacting Hamiltonian

$$\hat{H} = -\frac{\hbar^2}{2m} \nabla^2 + V(z), \quad (5.5)$$

where the periodic potential $V(z)$ can also be expressed in terms of Fourier series:

$$V(z) = \sum_{j'} v_{j'} e^{i2\pi j' z/a}. \quad (5.6)$$

The Schrödiner equation then turns to

$$\begin{aligned} E_q^n \phi_q^n(z) &= \hat{H} \phi_q^n(z) \\ &= \sum_j c_{q,j}^n \frac{\hbar^2 k_{q,j}^2}{2m} e^{ik_{q,j} z} + \sum_{j,j'} c_{q,j}^n v_{j'} e^{iqz+i2\pi(j+j')z/a} \\ &= \sum_j c_{q,j}^n \frac{\hbar^2 k_{q,j}^2}{2m} e^{ik_{q,j} z} + \sum_{j,j'} c_{q,j}^n v_{j'} e^{ik_{q,j+j'} z} \\ &= \sum_j c_{q,j}^n \frac{\hbar^2 k_{q,j}^2}{2m} e^{ik_{q,j} z} + \sum_j \left(\sum_{j'} c_{q,j-j'}^n v_{j'} \right) e^{ik_{q,j} z} \end{aligned} \quad (5.7)$$

Therefore

$$E_q^n c_{q,j}^n = c_{q,j}^n \frac{\hbar^2 k_{q,j}^2}{2m} + \sum_{j'} c_{q,j-j'}^n v_{j'}. \quad (5.8)$$

5.1.1 Solution for optical standing wave

For the optical standing wave mentioned above, the potential is

$$V(z) = \frac{V_0}{2} \left(1 - \cos\left(\frac{2\pi z}{a}\right) \right) = \frac{V_0}{2} (1 - e^{i2\pi z/a} - e^{-i2\pi z/a}), \quad (5.9)$$

so

$$v_0 = V_0/2, \quad v \pm 1 = -V_0/4. \quad (5.10)$$

For fixed q , E_q^n are eigenvalues of the effective Hamiltonian \hat{H}_q with

$$(H_q)_{j,j'} = \begin{cases} \frac{\hbar^2 k_{q,j}^2}{2m} + \frac{V_0}{2}, & j = j'; \\ -\frac{V_0}{4}, & j = j' \pm 1; \\ 0, & \text{otherwise.} \end{cases} \quad (5.11)$$

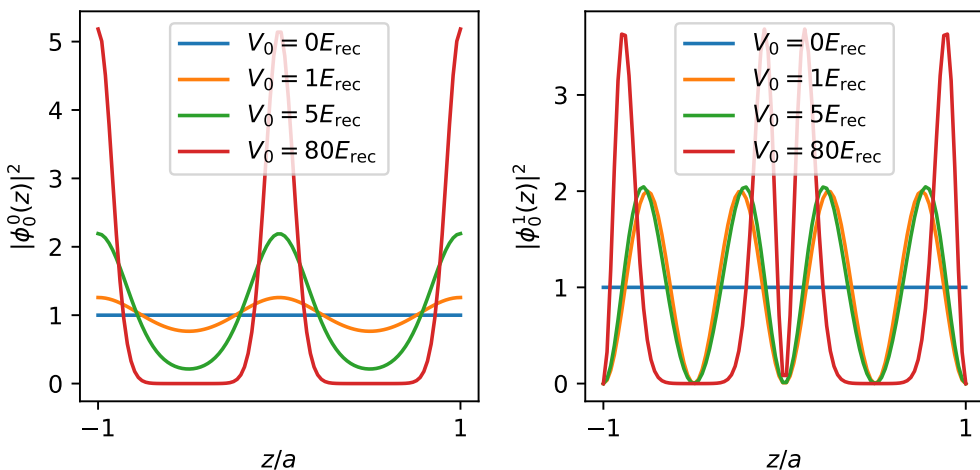


Figure 5.1: Ground state (left) and first excited state (right) wavefunctions of the sinusoidal optical lattice at $q = 0$. $E_{\text{rec}} = \pi^2 \hbar^2 / 2ma^2$.

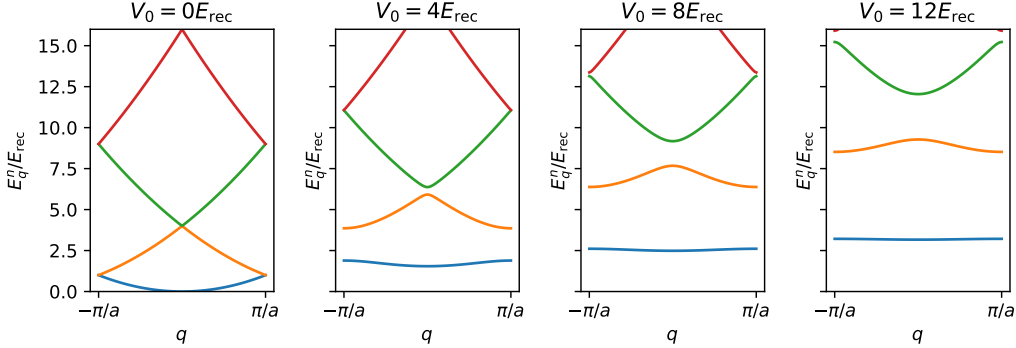


Figure 5.2: Band structure of the sinusoidal optical lattice. The lowest four bands are shown. $E_{\text{rec}} = \pi^2 \hbar^2 / 2ma^2$.

In Fig. 5.1, the wavefunction amplitudes of $q = 0$ case are plotted. As one can expect, the atoms are well localized around the potential minima for very deep lattices.

From the band structure view in Fig. 5.2, the potential opens the gaps in bands that flattens the dispersion relations and thus reduces the band width. In the deep lattice case, the other Fourier components are exponentially suppressed and the band dispersion can be well approximated by a cosine function with J being the half bandwidth

$$\omega(q) = E_q^0 = V_0/2 + 2J \cos(q \cdot a). \quad (5.12)$$

5.1.2 Phase velocity, group velocity

Since the dispersion relation is no longer parabolic, the usual relation $v = \hbar q/m$ between velocity and (quasi-)momentum is no longer valid. It is instead characterized by the *phase velocity*

$$v_{\text{ph}}(q) = \omega(q)/q \quad (5.13)$$

that describes the velocity of a propagating phase front and the *group velocity*

$$v_{\text{g}}(q) = \frac{\partial \omega(q)}{\partial q} \quad (5.14)$$

that describes the propagation velocity of a wave packet.

An interesting consequence of the band structure in the lattice is that a slowly accelerating particle can not acquire arbitrarily large energies: The particle will accelerate (the quasi-momentum q increases) until the band edge $q = \pi/a$ is reached. This point is symmetric to the $q = -\pi/a$ point, which means it is "reflected" if keeping being accelerated.

5.2 Momentum space measurements on atoms in lattices

5.2.1 Wannier functions

For deep lattices $V_0 \gg E_{\text{rec}}$, obviously the wavefunction of particles will be localized close to the potential minimum, or the *lattice site* on each lattice period. Since the lattice sites are only weakly connected by tunnelling, it becomes natural to consider a localized basis in real space rather than the delocalized Bloch basis. We thus introduce the *Wannier basis*. The Wannier functions $w^n(\mathbf{r})$ (we now move on to any dimension) are the discrete Fourier transform of Bloch wavefunctions evaluated at (in principle any lattice vector \mathbf{R} , and we focus on the case) 0 such that

$$w^n(\mathbf{r}) = \frac{1}{\sqrt{N}} \sum_{\mathbf{q}} \phi_{\mathbf{q}}^n(\mathbf{r}) \sim \frac{\sqrt{N}}{2\pi} \int \phi_{\mathbf{q}}^n(\mathbf{r}) d\mathbf{q} \quad (5.15)$$

or inversely

$$\phi_{\mathbf{q}}^n(z) = \frac{1}{\sqrt{N}} \sum_{\mathbf{R}} e^{i\mathbf{q}\cdot\mathbf{R}} w^n(\mathbf{r} - \mathbf{R}), \quad (5.16)$$

where N is the number of sites in the system and \mathbf{R} are all lattice vectors..

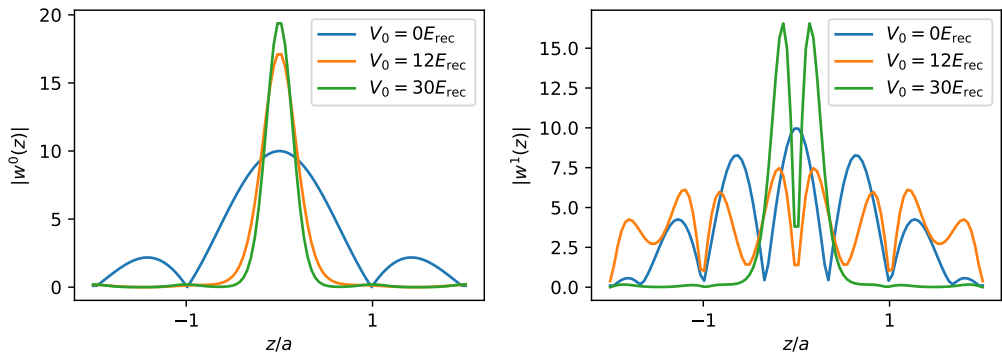


Figure 5.3: Ground state (left) and first excited state (right) Wannier functions of the sinusoidal optical lattice. $E_{\text{rec}} = \pi^2 \hbar^2 / 2ma^2$.

Just like in the free space, we can choose a second quantization representation of the bosonic system by defining the field operator

$$\hat{\Psi}(\mathbf{r}) = \sum_{n\mathbf{q}} \phi_{\mathbf{q}}^n(z) \hat{a}_{\mathbf{q}}^n. \quad (5.17)$$

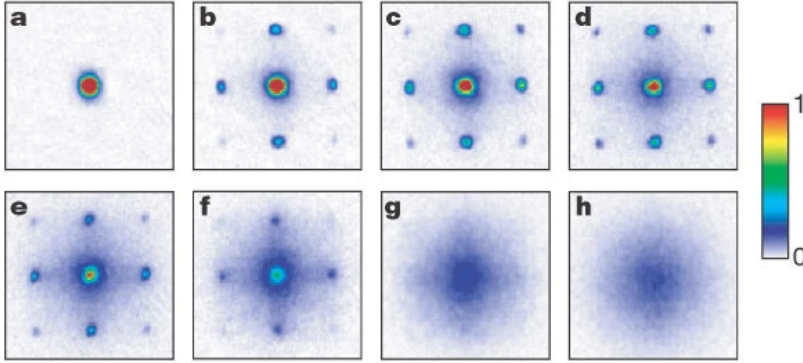


Figure 5.4: ToF image of atoms 15 ms after sudden releasing from 3D period standing wave potential (Greiner et al., 2003). $V_0 = 0, 3E_{\text{rec}}, 7E_{\text{rec}}, 10E_{\text{rec}}, 13E_{\text{rec}}, 14E_{\text{rec}}, 16E_{\text{rec}}$ and $20E_{\text{rec}}$ from a to h.

The same can be done for the Wannier basis:

$$\hat{\Psi}(\mathbf{r}) = \sum_{n, \mathbf{R}} w^n(\mathbf{r} - \mathbf{R}) \hat{a}_{\mathbf{r}}^n. \quad (5.18)$$

We are very often only interested in the ground state $n = 0$ case, and hence the superscript n as well as the sum is sometimes omitted.

5.2.2 Time of flight-imaging

In the time of flight method, when expanding from one of the energy eigenstates, which is a Bloch wavefunction, the (discrete) momentum components $k_{q,j}$ are effectively measured. For one given Bloch function, even for $q = 0$, we therefore expect to see a regular pattern of momenta occupied, resulting in a diffraction-pattern like distribution. In the low lattice $j \rightarrow 0$ limit, in particular $j = 0$ term dominates, whereas the increasing localization of the wave functions to the potential minima leads to a population of larger corresponding k -components for deeper lattices, see Fig. 5.4.

This can be calculated in Wannier basis, where the density distribution in space after the time of flight period t can be written as

$$\langle \hat{n}(\mathbf{r}, t) \rangle = \langle \hat{\Psi}^\dagger(\mathbf{r}, t) \hat{\Psi}(\mathbf{r}, t) \rangle, \quad (5.19)$$

where

$$\hat{\Psi}(\mathbf{r}, t) = \sum_j w_j(\mathbf{r}, t) \hat{a}_{\mathbf{R}}. \quad (5.20)$$

Assuming initial on-site Gaussian wavefunctions with width σ_0 in space, the operator at time t can be derived as

$$w_{\mathbf{R}}(\mathbf{r}, t) = W(\mathbf{r} - \mathbf{R}, t) \exp\left(\frac{i\hbar t(\mathbf{r} - \mathbf{R})^2}{2m\sigma_0^2\sigma_t^2}\right), \quad (5.21)$$

where

$$W(\mathbf{r}, t) = \frac{2\pi^{3/4}}{\sqrt{\sigma_0 + \frac{i\hbar t}{m\sigma_0}}} e^{-\frac{\mathbf{r}^2}{2\sigma_t^2}} \quad (5.22)$$

and

$$\sigma_t = \sqrt{\sigma_0^2 + \frac{\hbar^2 t^2}{\sigma_0^2 m^2}}. \quad (5.23)$$

Using Eq. (5.21), we obtain the density distribution

$$n(\mathbf{r}, t) = \sum_{\mathbf{R}, \mathbf{R}'} W^*(\mathbf{r} - \mathbf{R}) W(\mathbf{r} - \mathbf{R}') e^{\frac{i\hbar t(2\mathbf{r} - \mathbf{R} - \mathbf{R}')(\mathbf{R} - \mathbf{R}')}{2m\sigma_0^2\sigma_t^2}} \langle \hat{a}_{\mathbf{R}}^\dagger \hat{a}_{\mathbf{R}} \rangle. \quad (5.24)$$

Assume the expansion time t is so long such that $\sigma_t \gg |\mathbf{R}|$ for all lattice vectors, which also indicates the scale $|\mathbf{r}| \gg |\mathbf{R}|$. Furthermore $\sigma_t \gg \sigma_0$. With these approximations, finally

$$n(\mathbf{r}, t) = |W(\mathbf{r}, t)|^2 \sum_{\mathbf{R}, \mathbf{R}'} e^{\frac{i\mathbf{m}\cdot(\mathbf{R}-\mathbf{R}')}{\hbar t}} \langle \hat{a}_{\mathbf{R}}^\dagger \hat{a}_{\mathbf{R}'} \rangle. \quad (5.25)$$

Delocalized wavefunction consider the delocalized case, one dimensional single particle state

$$\frac{1}{\sqrt{N}} \sum_j \hat{a}_j^\dagger |0\rangle. \quad (5.26)$$

We have

$$n(x, t) = |W(x, t)|^2 \left| \sum_j e^{\frac{-im\cdot x a j}{\hbar t}} \right|^2. \quad (5.27)$$

In the one-dimensional case, it can be further simplified to be

$$n(x, t) = |W(x, t)|^2 \frac{\sin(\pi N x / l)^2}{\sin(\pi x / l)^2}, \quad (5.28)$$

where $l = 2\pi\hbar t / am$.

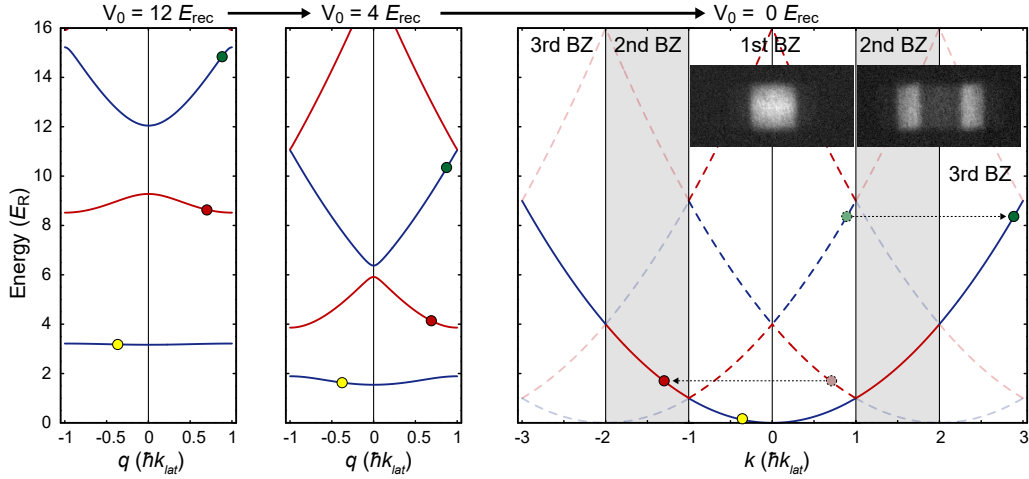


Figure 5.5: Band mapping.

Localized wavefunction for the localized case

$$\prod_j \frac{1}{\sqrt{n_j}} (\hat{a}_j^\dagger) |0\rangle, \quad (5.29)$$

the off-diagonal coherences are 0 and hence

$$n(x, t) = |W(x, t)|^2 \sum_j n_j. \quad (5.30)$$

5.2.3 Band mapping

Instead of suddenly switching off the lattice potential, which projects the wave function instantaneously to a superposition of free-space eigenfunctions in k -space, the potential can also be turned off adiabatically, which keeps the atom at the n -th band. For a given state $|\phi_q^n\rangle$, it will end up in the plane wave state $|q^n\rangle$. Adiabatic ramping of the potential is therefore a very convenient method to map the occupation distribution of q (quasi-momentum) states directly to a distribution of k (momentum) state occupation, allowing to measure the distribution in q directly. Here adiabaticity means slow compared to the band structure, but it should still be fast compared to the redistribution from scattering.

5.3 Bose Hubbard model

Start with free-space Hamiltonian with periodic potential and on site interaction. With the help of Wannier functions it can be rewritten as

$$\hat{H} = \sum_{i,j} -J_{ij}\hat{a}_i^\dagger\hat{a}_j + \sum_{i,j,k,l} U_{ijkl}\hat{a}_i^\dagger\hat{a}_j^\dagger\hat{a}_k\hat{a}_l. \quad (5.31)$$

When the Wannier functions are localized enough, these coefficients can be approximated as

$$J_{ij} = \begin{cases} E_i, & i = j; \\ J, & |i - j| = 1; \\ 0, & |i - j| > 1. \end{cases} \quad (5.32)$$

$$U_{ijkl} = \begin{cases} U, & i = j = k = l; \\ 0, & \text{otherwise.} \end{cases}$$

The constant offset E_i does not influence the physics and therefore the (Bose) Hubbard Hamiltonian can be written as

$$\hat{H} = \sum_{\langle ij \rangle} -J\hat{a}_i^\dagger\hat{a}_j + \sum_i U\hat{n}_i(\hat{n}_i - 1). \quad (5.33)$$

J is the *tunnel matrix element*, or tunnel coupling, while U is the on-site interaction coefficient. Both J and U can be calculated from the Wannier functions

$$J = - \int d\mathbf{r} \sum_{i,j} w^*(\mathbf{r}) \left(\frac{\hat{p}^2}{2m} + V(\mathbf{r}) \right) w(\mathbf{r} - a) \quad (5.34)$$

$$U = \frac{g}{2} \int d\mathbf{x} |w(\mathbf{r})|^4.$$

5.3.1 Non-interacting case

When the potential strength $V_0 = 0$, all atoms are free and thus the effective interaction $U = 0$. In this case, the only possible form of wavefunction according to Bloch theorem is

$$|\phi_q\rangle = \frac{1}{\sqrt{N}} \sum_j e^{-iqa \cdot j} \hat{a}_j^\dagger |0\rangle. \quad (5.35)$$

The corresponding energy eigenvalues are

$$E_q = -2J \cos(q \cdot a) \quad (5.36)$$

with corresponding bandwidth $4J$ (J can be determined also in this way), It is parabolic near $q = 0$, and hence an effective mass m^* can be defined such that

$$E_q \approx \frac{\hbar^2 q^2}{2m^*}. \quad (5.37)$$

Ground state The single particle ground state wave function is then the $q = 0$ Bloch wavefunction

$$|\phi_0\rangle = \frac{1}{\sqrt{N}} \sum_j \hat{a}_j^\dagger |0\rangle. \quad (5.38)$$

For the non-interacting case with M particles, the ground state is

$$|\Psi_0\rangle \propto \left(\sum_j \hat{a}_j^\dagger \right)^M |0\rangle. \quad (5.39)$$

In the particular limit $N, M \rightarrow \infty$ with $M/N = \tilde{n} = \text{const}$, the state can also be formulated as a product coherent state

$$|\Psi_0\rangle = \prod_j \hat{a}_j^\dagger |0\rangle, \quad (5.40)$$

where the average particle number is $|\alpha|^2 = \tilde{n}$ on each site. The probability of finding a given particle number n on a give site obeys a *Poisson distribution*. In particular, there is phase coherence over arbitrary distances as $\langle \hat{a}_i^\dagger \hat{a}_j \rangle = |\alpha|^2$ holds for any $|i - j|$.

5.3.2 Interaction dominated case

In the strongly interacting case $U \gg J$, for large occupations the ground state is also easy to find:

$$|\Psi_0\rangle = \prod_j \left(\frac{1}{\sqrt{n!}} \hat{a}_i^\dagger \right)^n |0\rangle. \quad (5.41)$$

The particles are evenly distributed on each site such that the interaction term (which dominates as it is quadratic) is minimized. Intuitively when the potential strength $V_0 \rightarrow \infty$, hopping becomes difficult, so it just corresponds to the strongly interacting case.

5.3.3 Phase transition in Bose-Hubbard model

When we tune V_0 from 0 to infinity, U/J also effectively goes from 0 to infinity. The atoms go through a transition from the coherent superfluid phase to the localized Mott insulator phase. In Fig. 5.4, the momentum space behaviors of these two distinct phases are shown. A transition point around $V_0 = 13E_{\text{rec}}$ is indicated, which corresponds to $U/J \approx 36$.

Bibliography

Andrews, M. R.

1997. Observation of Interference Between Two Bose Condensates. *Science*, 275(5300):637–641.

Becker, C., S. Stellmer, P. Soltan-Panahi, S. Dörscher, M. Baumert, E.-M. Richter, J. Kronjäger, K. Bongs, and K. Sengstock
2008. Oscillations and interactions of dark and dark–bright solitons in Bose–Einstein condensates. *Nature Physics*, 4(6):496–501.

Bloch, I., J. Dalibard, and W. Zwerger

2008. Many-body physics with ultracold gases. *Reviews of Modern Physics*, 80(3):885–964.

Chu, S., L. Hollberg, J. E. Bjorkholm, A. Cable, and A. Ashkin

1985. Three-dimensional viscous confinement and cooling of atoms by resonance radiation pressure. *Physical Review Letters*, 55(1):48–51.

Davis, K. B., M. O. Mewes, M. R. Andrews, N. J. van Druten, D. S. Durfee, D. M. Kurn, and W. Ketterle
1995a. Bose-Einstein Condensation in a Gas of Sodium Atoms. *Physical Review Letters*, 75(22):3969–3973.

Davis, K. B., M.-O. Mewes, M. A. Joffe, M. R. Andrews, and W. Ketterle
1995b. Evaporative Cooling of Sodium Atoms. *Physical Review Letters*, 74(26):5202–5205.

Giorgini, S., L. P. Pitaevskii, and S. Stringari

2008. Theory of ultracold atomic Fermi gases. *Reviews of Modern Physics*, 80(4):1215–1274.

Greiner, M., O. Mandel, T. Rom, A. Altmeyer, A. Widera, T. W. Hänsch, and I. Bloch

2003. Quantum phase transition from a superfluid to a Mott insulator in an ultracold gas of atoms. *Physica B: Condensed Matter*, 329-333:11–12.

BIBLIOGRAPHY

- Ketterle, W., D. S. Durfee, and D. M. Stamper-Kurn
1999. Making, probing and understanding Bose-Einstein condensates.
- Pethick, C. J. and H. Smith
2008. *Bose-Einstein Condensation in Dilute Gases*, volume 102. Cambridge: Cambridge University Press.
- PHILLIPS, W. D., P. L. GOULD, and P. D. LETT
1988. Cooling, Stopping, and Trapping Atoms. *Science*, 239(4842):877–883.
- Thomas, N. R., N. Kjærgaard, P. S. Julienne, and A. C. Wilson
2004. Imaging of s and d Partial-Wave Interference in Quantum Scattering of Identical Bosonic Atoms. *Physical Review Letters*, 93(17):173201.